

Copyright
by
Jorge Barrios Rivera
2003

The Dissertation Committee for Jorge Barrios Rivera certifies that this is the approved version of the following dissertation:

**STRATIGRAPHIC ANALYSIS OF REFLECTIVITY DATA,
APPLICATION TO GAS RESERVOIRS IN THE BURGOS
BASIN, MEXICO**

Committee:

William L. Fisher, Supervisor

Bob A. Hardage, Co-Supervisor

Robert H. Tatham

Carlos Torres-Verdín

Albert W. Bally

**STRATIGRAPHIC ANALYSIS OF REFLECTIVITY DATA,
APPLICATION TO GAS RESERVOIRS IN THE BURGOS
BASIN, MEXICO**

by

Jorge Barrios Rivera B.S., M.Sc.

Dissertation

Presented to the Faculty of the Graduate School of

The University of Texas at Austin

in Partial Fulfillment

of the Requirements

for the Degree of

Doctor of Philosophy

The University of Texas at Austin

December, 2003

Dedication

In memory of my father, Eleuterio Barrios Del Angel, who showed me the real
path of life

Acknowledgements

I would like to thank Petróleos Mexicanos (PEMEX, Exploración y Producción, Región Sur), for giving me the opportunity to pursue Ph.D. studies at The University of Texas at Austin. I am grateful to Pablo Cruz Helú and Rosalío Hernández García for their encouragement to study in The University of Texas at Austin in the John A. and Katherine G. Jackson School of Geosciences Ph.D. program.

I thank Antonio Escalera, Pedro Silva, Javier Méndez, Víctor Mercado, Humberto Salazar, Martín Méndez, Víctor Portales, Alfonso Limón, and Fernando Zurita from the Activo de Exploración Reynosa, for their support and for providing me the complete data set from the Misión, Cañón, and Lomitas gas field areas.

A note of gratitude goes to Gorgonio García Molina, Julio Cerrillo Cruz, Guillermo Pérez Cruz, and Francisco Sánchez de Tagle y de la Lastra for their continuous support and friendship.

I am especially grateful to William L. Fisher for his support and encouragement during my research. I am grateful to Carlos Torres-Verdín for his strong guidance and training in seismic inversion. I thank Bob A. Hardage for his valuable support of my dissertation.

Special thanks go to my outside committee member Albert W. Bally, who agreed to be part of my committee, for his valuable suggestions; I thank Robert H. Tatham for his kind support and comments. I thank Alejandro, Pedro, Juan, Javier, Faustino, Ricardo, Verónica, Andrea, Eliseo, Oscar, Katrin, Ramón, Estrella, Silvia, and Arturo, for their suggestions and friendship, and Effie Jarrett, for her support in the workstation laboratory.

Special thanks to Amanda Masterson who helped me to edit this dissertation.

I thank my beloved mother, siblings, mother-in-law, and siblings-in-law for their help and love.

Last but not least, I am grateful to my loving wife, Norma Edith, for her unconditional support and patience during the last five years. I thank my lovely children, Jocelyn Edith, and Jorge Luis, for making my life more enjoyable while living in Austin.

**STRATIGRAPHIC ANALYSIS OF REFLECTIVITY DATA,
APPLICATION TO GAS RESERVOIRS IN THE BURGOS
BASIN, MEXICO**

Publication No. _____

Jorge Barrios Rivera, Ph.D.

The University of Texas at Austin, 2003

Supervisors: William L. Fisher and Bob A. Hardage

Reflectivity data derived from the inversion of post-stack seismic data can be used to improve the detection and spatial delineation of stratigraphic sequences. The enhancement in spatial resolution inherent to post-stack inversion can often substantially improve standard delineation results based on seismic amplitudes. In this research, a study is described of the use of reflectivity data to delineate stratigraphic sequences associated with gas-producing sands in a mature basin. Stratigraphic units in the Burgos Basin consist of Oligocene, wave-dominated deltaic sequences within delta front and prodelta facies. Post-stack reflectivity data helped to define the lateral continuity of coast-parallel sand

bodies deposited by wave action and reworking of sediments supplied by the ancient Rio Grande.

An attempt was made to discriminate high-porosity, clean sands from shaly sands within a given sand unit. This was done using reflectivity data derived from pre-stack inversion. Extensive petrophysical analysis confirmed that pre-stack inversion could provide a quantitative method that discriminates high-quality from low-quality sands. In particularly favorable situations, pre-stack inversion results could even help to discriminate between water and gas. Pre-stack inversion yielded angle-dependent reflectivities as well as density, P-wave and S-wave velocities. Transformations of these properties into Lamé's $\lambda \cdot \rho$ and $\mu \cdot \rho$ parameters were also explored to assess the influence of shale volume, total porosity, and rock type within sand and shale units delineated by post-stack inversion. Spatial delineation of sand units is presented near two key exploration wells. Success in the location of development wells is significantly constrained by the spatial delineation of reservoir units.

Table of Contents

Dedication	iv
Acknowledgments	v
Abstract	vii
Table of Contents	ix
List of Tables	xiii
List of Figures	xv
Chapter 1 Introduction	1
1.1 Purpose and Objectives	1
1.2 Location of Study Area	2
1.3 Methodology	3
1.3.1 Regional Structural Framework Recognition.....	5
1.3.2 Vicksburg Stratigraphic Units.....	5
1.3.3 Petrophysical Analysis at Reservoir Interval	5
1.3.4 Stratigraphic Analysis of Reflectivity Data from Post- Stack Inversion.....	6
1.3.5 Stratigraphic Analysis of Reflectivity Data from Pre- Stack Inversion.....	6
1.3.6 Facies Architecture Interpretation.....	6
1.4 Digital Dataset.....	7
1.4.1 3D Seismic Data.....	7
1.4.2 Vertical Seismic Profiles (VSP).....	10
1.4.3 Well Logs	10
1.4.4 Production Data.....	10
1.5 Geological Setting.....	12
1.5.1 Structure	12

1.5.2 Vicksburg Petroleum System	16
1.5.3 Oligocene Stratigraphy and Biostratigraphy	17
Chapter 2 Structural and Stratigraphic Environments of Natural Gas Reservoirs in the Vicksburg Flexure Expanded Sediments in Burgos Basin, Northern México	23
2.1 Introduction	23
2.2 Regional Structural Framework	23
2.2.1 Seismic Transect I	24
2.2.2 Seismic Transect II	27
2.2.3 Growth Fault Patterns in South Texas and Northern México	29
2.2.4 Reservoir Structural Habitat	31
2.3 Analogue Reservoirs with South Texas	32
2.4 Stratigraphic Units	32
2.5 3D Seismic Interpretation	36
2.5.1 Methodology	36
2.5.2 Crossline 200	37
2.5.3 Inline 1700	37
2.5.4 Time Slice Analysis	37
2.5.5. Isochron Map of 32.4 ma Sequence Boundary	43
2.6 Conclusions	43
2.6.1 Structure	43
2.6.2 Stratigraphy	45
Chapter 3 Petrophysical Analysis	46
3.1 Introduction	46
3.2 Well Log Digital Data Base	47
3.3 Well Log Analysis	47
3.4 Elastic Constants	52
3.4.1 Elastic Constants and Their Relationships to Rock Matrix and Fluids	54

3.5 Crossplotting	55
3.6 Biot-Gassmann Sensitivity Analysis	62
3.7 Fluid and Lithology Discrimination	68
3.8 Conclusions	70
Chapter 4 Stratigraphic Analysis of Reflectivity Data I: Enhancing Lateral and Vertical Resolution with Constrained Sparse Spike Inversion	71
4.1 Introduction	71
4.2 Background	73
4.3 Methodology	75
4.3.1 Structural Analysis	75
4.3.2 Stratigraphic Units.....	76
4.3.3 Earth Model.....	76
4.3.4 Seismic Bandwidth and Wavelet Extraction.....	78
4.3.5 Constrained Sparse Spike Inversion (CSSI).....	83
4.3.6 Seismic Horizons Picking on the Reflectivity Volume.....	88
4.3.7 Attribute Extraction.....	88
4.3.8 Interpretation of Amplitude Attribute Maps	93
4.4 Conclusions	95
Chapter 5 Stratigraphic Analysis of Reflectivity Data II: Lamé Petrophysical Parameters as a Lithology and Fluid Discriminators	97
5.1 Introduction	97
5.1.1 Data set.....	97
5.2 Methodology	99
5.2.1 Petrophysical Analysis	100
5.2.2 Angle-Dependent Inversion	100
5.2.3 Angle Sub-Stacks Computation	102
5.2.4 Elastic Impedance Computation.....	104
5.3 Reflectivity Analysis	106

5.4 Amplitude Attribute Extraction.....	108
5.4.1 S Field Amplitude Attribute Reflectivity Maps	111
5.4.2 K Field Amplitude Attribute Reflectivity Maps	111
5.5 Lamé Parameters, Rock Quality and and Fluid Discrimination.....	112
5.5.1 Lambda/mu ratio Maps	113
5.6 Conclusions	120
Chapter 6 Discussion of Results.....	121
6.1 Structure	121
6.2 Stratigraphy	122
6.3 Petrophysics	122
6.4 Post-Stack Inversion.....	124
6.5 Angle-Dependent Inversion	125
Appendix A, Well Database.....	126
Appendix B, Time-Depth Tables and Velocity Graphs	129
Appendix C, Cored Intervals.....	155
Appendix D, Production Database	156
Bibliography.....	158
Vita	167

List of Tables

Table 1.1 Acquisition parameters in the 3D P-wave survey, Misión-Lomitas	9
Table 1.2 Vertical resolution computed in the wells S-1 and K-1.	11
Table 1.3 Lower Oligocene (Vicksburg Formation).....	19
Table 1.4 Middle Oligocene (Norma Conglomerate and Frio members)	21
Table 1.5 Upper Oligocene (Anahuac Formation).....	22
Table A.1 Data base of the wells used in this study.....	126
Table B.1 Velocity data from the A-1 well.....	129
Table B.2 Velocity data from the Baz-1 well.....	131
Table B.3 Velocity data from the Dra-1 well.....	133
Table B.4 Velocity data from the Ec-1 well.....	135
Table B.5 Velocity data from the Em-1 well	137
Table B.6 Velocity data from the Gal-1 well	139
Table B.7 Velocity data from the Gali-1 well.....	141
Table B.8 Velocity data from the Ind-1 well	143
Table B.9 Velocity data from the K-1 well.....	145
Table B.10 Velocity data from the Mac-1 well.....	147
Table B.11 Velocity data from the M-1001 well	149
Table B.12 Velocity data from the S-1 well.....	151

Table B.13 Velocity data from the S-2 well.....	153
Table C.1 Core intervals in wells in the study area.....	155
Table D.1 Production data from the last drilled wells in the Vicksburg trend in the Burgos Basin	156
Table D.2 Production data for Vicksburg fields in the Burgos Basin.....	157

List of Figures

Figure 1.1 Location of the study area region and the outline of the 3D survey	4
Figure 1.2 Location of the study area showing the major gas fields.....	8
Figure 1.3 Major depocenters postulated in Texas coast and northern México....	13
Figure 1.4 Depositional structural model of the Vicksburg Formation in the Burgos Basin and positions of wells S-1 and K-1	15
Figure 1.5 Geologic column of the Tertiary in Burgos Basin.....	18
Figure 1.6 Index fossils of Early Oligocene age in the Burgos Basin	20
Figure 2.1 Structural compilations for South Texas and northern México.....	25
Figure 2.2 Dip-oriented seismic transect I, showing the sequence boundary correlation through the Burgos Basin.....	26
Figure 2.3 Dip-oriented seismic transect II, displaying the structural styles affecting Cenozoic and Mesozoic strata in the Burgos Basin.....	28
Figure 2.4 Dip-oriented profiles from South Texas an northern México.....	30
Figure 2.5 Log type showing the stratigraphic units and major flooding surfaces that define the Vicksburg stratigraphy in South Texas and northern México	34
Figure 2.6 Dip-oriented well correlations transect showing the relationship between up-dip and down-dip sequences.....	35
Figure 2.7 Dip-oriented crossline 200.....	38
Figure 2.8 Strike oriented inline 1700.....	39

Figure 2.9A Time slice at 1000 ms of two-way time showing the structural characteristics found in the study area	40
Figure 2.9B Time slice at 2000 ms of two-way time showing the structural characteristics found in the study area	41
Figure 2.9C Time slice at 2700 ms of two-way time showing the structural characteristics found in the study area	42
Figure 2.10 Isochron map of the 32.4 ma sequence boundary that corresponds to the top of the Vicksburg Formation	44
Figure 3.1 Base map highlighting key wells used for the detailed petrophysical analysis in the study area.....	48
Figure 3.2 Composite log tracks from the S-1 well	51
Figure 3.3 Composite log curves showing a suite of measured and computed curves	56
Figure 3.4A Crossplot of reservoir interval 2827-2847 m in the S-1 well.....	57
Figure 3.4B Crossplot of reservoir interval 3450-3460 m in the K-1 well	59
Figure 3.4C Crossplot of reservoir interval 2827-2847 m in the S-1 well.....	61
Figure 3.5 Core petrophysical analyses at reservoir interval in S-1 well.....	65
Figure 3.6A Biot-Gassmann sensitivity analysis in the S-1 well.....	66
Figure 3.6B Biot-Gassmann sensitivity analysis in the K-1 well	67
Figure 3.7 Lambda*rho versus mu*rho crossplot displaying separation of the reservoir zone	69

Figure 4.1 Location map showing the position of the study area in the Burgos Basin, northern México	74
Figure 4.2 Regional structural framework in the study area	77
Figure 4.3 Solid model illustrating the sequence boundary D and the subdivision into six micro-layers within the sequence.....	79
Figure 4.4 Amplitude-frequency character of data extracted in the 2,000-2,800 ms interval	80
Figure 4.5 Wavelet extraction in the S field for a time window between 1850 and 2050 milliseconds	82
Figure 4.6 Flow chart of the post-stack inversion methodology used in this study	84
Figure 4.7 Porosity bodies extracted from P-impedance derived from post-stack seismic inversion.....	87
Figure 4.8 Reflectivity retraced horizons used to make a better detailed correlation of seismic interfaces.....	89
Figure 4.9A Amplitude map extraction in the reservoir of the S field.....	91
Figure 4.9B Amplitude map extraction in the reservoir of the K field	92
Figure 4.10 Sedimentary model interpreted from attribute map.....	94
Figure 5.1 Location map of study area displaying the key well locations.	98
Figure 5.2 Flow chart of the methodology for simultaneous inversion.	101
Figure 5.3 Angle-dependent convolutional model.....	103
Figure 5.4 Angle stacks computation methodology.....	105
Figure 5.5 Elastic and acoustic impedance computation in S-1 well.....	107

Figure 5.6 Comparison between the seismic interpretation and detailed tracing of horizons on the reflectivity.	109
Figure 5.7 Amplitude maps displaying the reflectivity from post-stack and pre-stack inversion in S and K fields.	110
Figure 5.8 Lambda/mu ratio section and map in the S field..	114
Figure 5.9 Lambda/mu ratio section and map in the K well.....	117
Figure 5.10 Comparison between lambda/mu ratio and badlimited P_impedance in the S Field.....	118
Figure 5.11 Comparison between lambda/mu ratio and bandlimited P_impedance in the K Field.....	119
Figure B.1 Time depth graph interval velocities from A-1 well.....	130
Figure B.2 Time depth graph interval velocities from Baz-1 well.....	132
Figure B.3 Time depth graph interval velocities from Dra-1 well.....	134
Figure B.4 Time depth graph interval velocities from Ec-1 well.....	136
Figure B.5 Time depth graph interval velocities from Em-1 well.....	138
Figure B.6 Time depth graph interval velocities from Gal-1 well.....	140
Figure B.7 Time depth graph interval velocities from Gali-1 well.....	142
Figure B.8 Time depth graph interval velocities from Ind-1 well.....	144
Figure B.9 Time depth graph interval velocities from K-1 well.....	146
Figure B.10 Time depth graph interval velocities from Mac-1 well.....	148
Figure B.11 Time depth graph interval velocities from M-1001 well.....	150
Figure B.12 Time depth graph interval velocities from S-1 well.....	152
Figure B.13 Time depth graph interval velocities from S-2 well.....	154

Chapter 1

Introduction

1.1 PURPOSE AND OBJECTIVES

Exploration for gas reservoirs in mature basins often requires specialized geophysical techniques. Understanding heterogeneity in potential gas reservoirs provides opportunities for locating additional reserves in mature plays such as the Vicksburg Formation in the Burgos Basin. Quantitative modeling techniques can be effective in accomplishing such objectives.

Gas reservoirs in Vicksburg sedimentary sequences often cannot be fully characterized with seismic data because spatial discontinuity, thickness, and structural complexity do not permit resolution of the stratigraphic units. Seismic resolution depends on seismic source characteristics and earth layer responses that produce reflection coefficient series (Castagna and Backus, 1993). For seismic reflection of compressional waves (P) at normal incidence, seismic amplitudes are caused by contrasts in acoustic impedance (density times velocity). In multichannel seismic data, oblique reflections are recorded, and they are affected by mode conversions from P-waves to S-waves (Ostrander, 1984); Amplitude versus angle (AVA) behavior exhibited by seismic reflection events depends on contrasts in S impedance ($V_s\rho$) as well as P impedance ($V_p\rho$) (Connolly, 1999). AVA methodology can be used as a direct hydrocarbon indicator (DHI) and, in

some cases, as a lithology discriminating tool, because gas reservoirs usually have specific characteristics of V_p/V_s ratio (Tatham and Stoffa, 1976), elastic parameters, and amplitude versus angle behavior.

Reflectivity data derived from seismic inversion are useful because wavelet effects have been reduced and should be used to better position exploration and development wells. Reflectivity maps may often delineate the stratigraphic features better than do ordinary seismic maps.

This project intends to provide a methodology to model potential gas reservoirs in the Vicksburg Formation in the Burgos Basin. Thus, the lateral and vertical seismic resolution is enhanced to define the boundaries of the stratigraphic bodies and to predict fluid content in sands using reflectivity data from post-stack and pre-stack inversion.

The objectives of this study are: (1) enhanced lateral and vertical seismic resolution in gas reservoirs, (2) stratigraphic analysis of reflectivity data derived from post-stack inversion to delineate the spatial continuity of gas reservoirs, (3) extraction of porosity and reservoir properties, (4) lithology and fluid discrimination by Lamé's petrophysical parameters ($\lambda \cdot \rho$ and $\mu \cdot \rho$) derived from stratigraphic analysis of reflectivity data from pre-stack inversion, and (5) facies architecture modeling of gas reservoirs.

1.2 LOCATION OF STUDY AREA

The Burgos Basin is the principal, non-associated, gas-producing basin in México. Hydrocarbon exploration in the basin began in the 1920's with the

discovery of gas and condensate reservoirs of Eocene age. The Oligocene Vicksburg Formation includes prolific oil and gas reservoirs in Texas and México; it has yielded more than 300 Tcf of gas since production began in the 1940's. (Corpus Christi Geological Society, 1968; Sandoval-Cambranis, 1969; Yzaguirre, 1969; Rodríguez-Santana, 1969; Busch, 1973, 1975; González-García, 1976; Echánove-Echánove, 1976, 1986; Kosters et al., 1989; Combes, 1990; Coleman and Galloway, 1990; Langford et al., 1992).

The Burgos Basin is located in northern México, covers some 50,000 square kilometers, and is the southern continuation into México of the Rio Grande Embayment. It is bounded by the Rio Grande to the north, the Tamaulipas arch to the south, the Sierra Madre Oriental to the west, and the Gulf of México to the east. The area of this study is located in the north-central portion of the Burgos Basin (Figure 1.1) and covers an area of approximately 450 square kilometers, including the Misión, Cañón, and Lomitas fields, which are located in the Oligocene hydrocarbon trend.

1.3 METHODOLOGY

The methodology used in this research involved six main steps:

1. Structural Framework Definition
2. Vicksburg Stratigraphic Units Definition
3. Petrophysical Analysis of Reservoir Intervals
4. Stratigraphic Analysis of Reflectivity Data from Post-Stack Inversion
5. Stratigraphic Analysis of Reflectivity Data from Pre-Stack Inversion

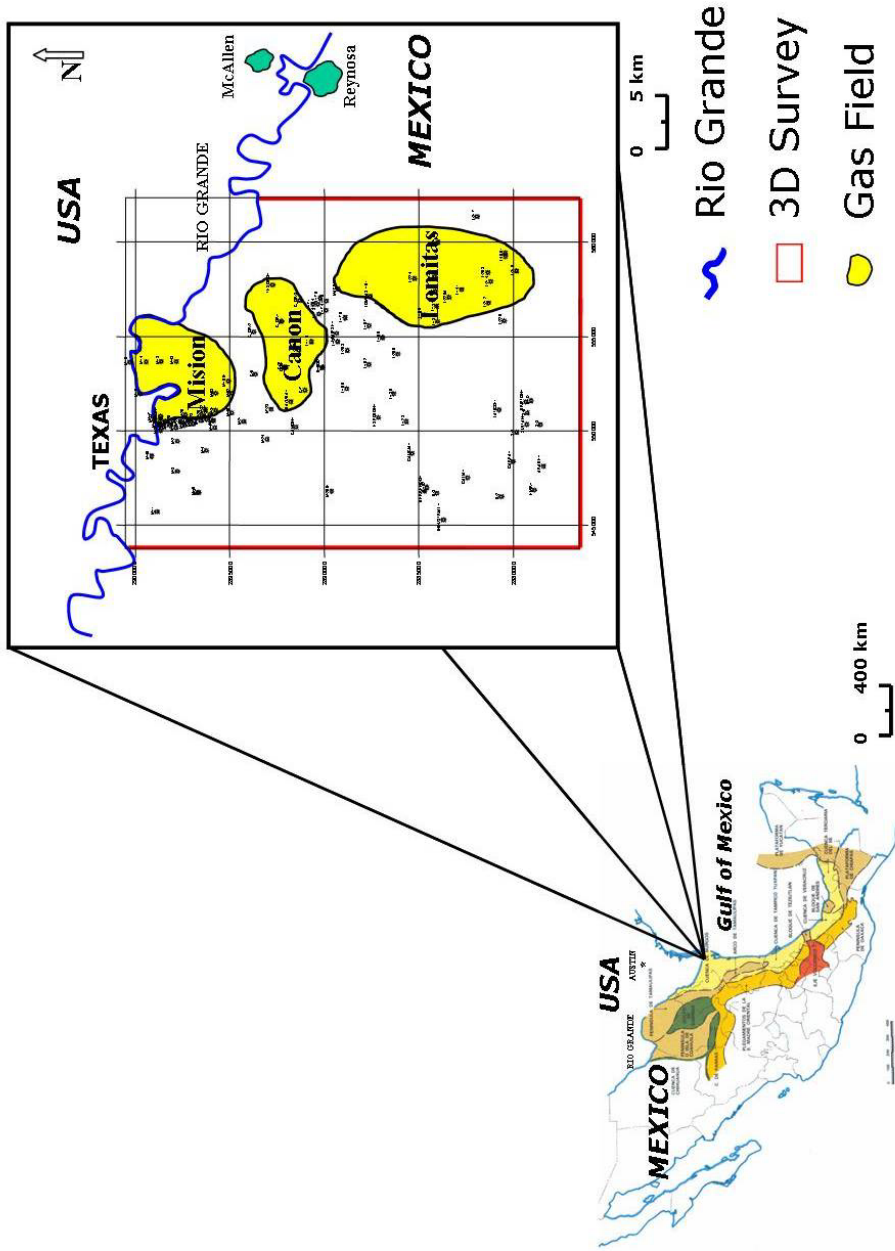


Figure 1.1 Location of the study area region and outline of the 3D survey used in this research.

6. Facies Architecture Delineation and Interpretation

1.3.1 Regional Structural Framework Recognition

The regional structural framework, based on a broad regional seismic grid including two dip regional transects, illustrates the structural styles of the Burgos Basin. Each line is a composite of several seismic lines and is presented as a continuous profile.

1.3.2 Vicksburg Stratigraphic Units

Six stratigraphic units were defined based on flooding surfaces within the Oligocene in the Vicksburg Formation within a 3D survey area. The identification of six stratigraphic units was fundamental to understanding the structural and stratigraphic environments of the reservoirs.

1.3.3 Petrophysical Analysis at Reservoir Interval

Petrophysical analysis of in twelve key wells allowed assessment of the effect of compaction, fluid content, sand/shale ratio, and saturation. The results were calibrated against core analysis. Petrophysical analysis was useful to discriminate high-porosity, clean sands from shaly sands within a given unit. Petrophysical analysis confirmed that pre-stack seismic inversion could help to quantitatively discriminate high-quality sands from low-quality sands.

1.3.4 Stratigraphic Analysis of Reflectivity Data from Post-Stack Inversion

Post-stack seismic inversion was useful to increase the resolution of reflectivity data and helped to model the stratigraphic units. Post-stack reflectivity data also helped to define the lateral continuity of coast-parallel sand bodies deposited by wave action and reworking of sediments supplied by ancient Rio Grande systems.

1.3.5 Stratigraphic Analysis of Reflectivity Data from Pre-Stack Inversion

Pre-stack seismic inversion helped to discriminate between lithology and fluids in reservoirs. Pre-stack seismic inversion also yielded angle-dependent reflectivities, density, and P-wave and S-wave velocities. Parameter transformations of these properties into Lamé's lambda and mu constants were also explored to assess shale volume, total porosity, and fluid type within sand units delineated with post-stack inversion.

1.3.6 Facies Architecture Interpretation

Facies architecture imaging was based on amplitude maps extracted from seismic data and reflectivity data derived from post-stack and pre-stack inversions. The computation of Lamé's petrophysical parameters played an important role in lithology discrimination and rock quality assessment as well.

1.4 DIGITAL DATASET

The data set available for this research consists of 120 wells (Appendix A) distributed mostly over three major gas fields; complete sets of conventional logs from these wells, a 3D P-wave seismic survey covering 450 km² (Figure 1.2); twelve zero-offset VSP surveys; well testing data; and twelve recently drilled wells with a complete set of borehole logs, including core data, biostratigraphic data, and full wave dipole-sonic logs. The complete dataset belongs to Petróleos Mexicanos (PEMEX) and was made available for this dissertation.

The following section describes the characteristics of the dataset used in this study.

1.4.1 3D Seismic Data

Three dimensional P-wave seismic data in this study are part of survey “Misión-Lomitas-Tinta” survey and cover 450 km². These data were acquired by PEMEX in 1999 using the following acquisition parameters (Table 1.1).

Seismic Resolution

Seismic resolution is critical in stratigraphic and reservoir studies (Sheriff, 1985; Brown, 1999). Good seismic resolution should allow mapping of specific features based on an observed seismic event. For a bed to be resolved by seismic data, a distinct event must occur at the top and the bottom of a given layer (Sheriff, 1985). In principle, seismic resolution is either vertical or horizontal. In practice, vertical resolution is computed by the limit of separation (Rayleigh

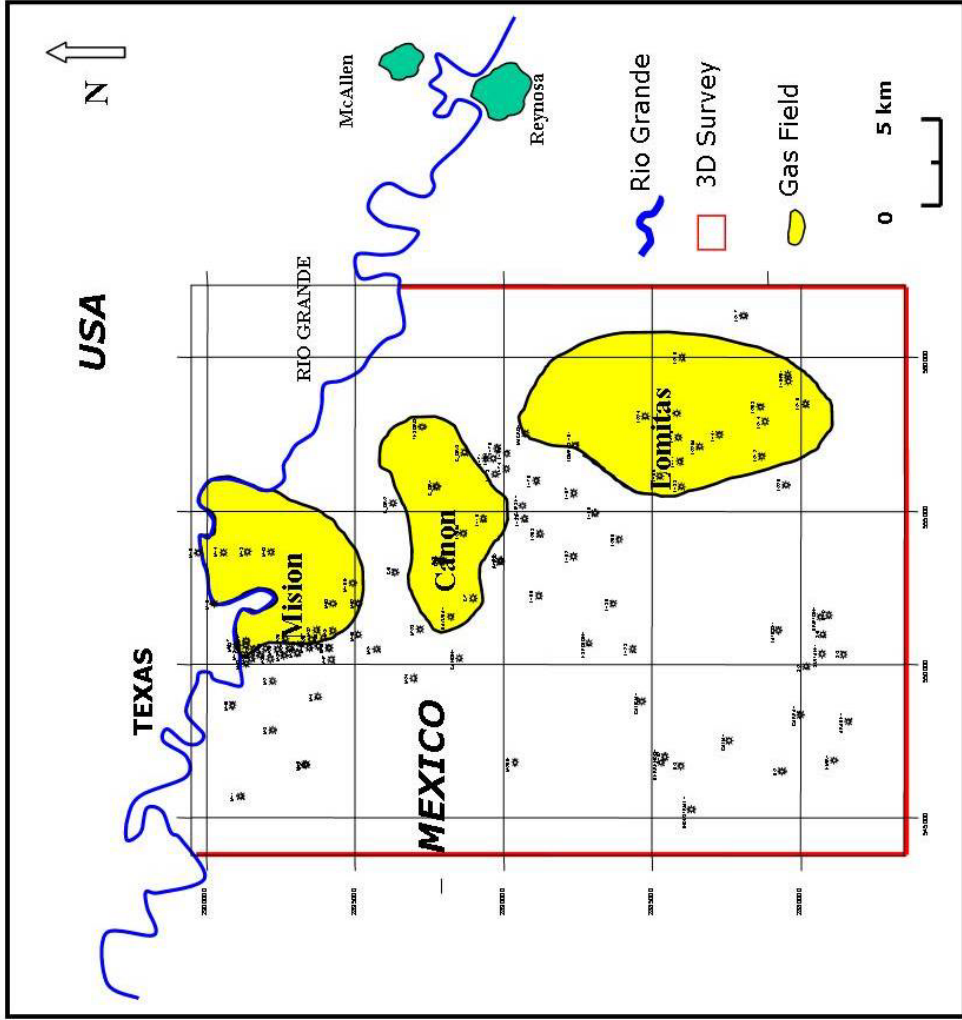


Figure 1.2 Location of the study area showing the major gas fields in yellow.

Parameter	Type/Value
Nominal fold	30 fold
Energy source	Vibroseis
Sweeps in VP	10 sweeps
Sweep length	12 seconds
Record length and sample interval	6 seconds/2 milliseconds
Bandwidth sweep	10-90 Hertz
Sweep type	Non linear +3 db/oct
Sweep taper	200 milliseconds
Source pattern	4 Vibroseis-13 meters-10 seconds-4 meters
Receiver pattern	6 receivers/20 meters
Field filters	3-135 Hz. ½ Nyq. Min
Bin size	20 meters x 20 meters
Receiver station spacing	40 meters
Source station spacing	40 meters
Receiver line spacing	400 meters
Source line spacing	400 meters
Number of receiver lines in patch	10 receiver lines
Active channels in line	132 channels
Active channels in patch	1320 channels
Number of VP's in km ²	~57
Minimum offset/maximum	620 meters/3421 meters
Inline offset	2620 meters
Crossline offset	2180 meters
Inline taper	1100 meters
Crossline taper	800 meters

Table 1.1 Acquisition parameters in the 3D P-wave survey across Misión-Lomitas-Tinta.

limit), which has a value of $\frac{1}{4}$ of the dominant wavelength (λ). The dominant wavelength is determined by the ratio of average velocity to frequency. In Table 1.2 the Rayleigh limit has been computed in wells S-1 and K-1.

1.4.2 Vertical Seismic Profiles (VSP)

Twelve zero-offset vertical seismic profiles (VSP) are available for the following wells: Ind-1, Em-1, A-1, S-1, S-2, K-1, Gal-1, Gali-1, Ec-1, Mac-1, Dra-1, and M-1001 (see velocity tables and time-depth graphs in Appendix B).

1.4.3 Well Logs

Most of the wells have conventional logs such as caliper, spontaneous potential (SP), gamma ray (GR), density-porosity (DPHI), bulk density (RHOB), porosity-sonic (BHC), neutron-porosity (NPHI), and resistivity (ILM and ILD) logs. The data quality and quantity permit stratigraphic and structural correlations. Eleven wells have a complete set of well logs, including dipole sonic profiles (DSI): Ind-1, Em-1, A-1, S-1, K-1, Gal-1, Gali-1, Ec-1, Mac-1, Dra-1, and M-1001. Some wells have cores from gas reservoirs of specific interest (see table of cores in Appendix C).

1.4.4 Production Data

The Vicksburg Formation contains prolific oil and gas reservoirs (Corpus Christi Geological Society, 1968; Sandoval-Cambranis, 1969; García del Angel, 1969; Yzaguirre, 1969; Rodríguez-Santana, 1969; Busch, 1973, 1975; González-

WELL	POROSITY [%]	VOLUME OF SHALE [%]	GROSS SAND [m]	NET SAND [m]	LAMBDA [m] FREQUENCY [Hz] VELOCITY [m/s]	RAYLEIGH RESOLUTION LIMIT [m]	FLUID
S-1	19.40%	1%	95 meters	81 meters	125 meters 20 Hertz 2500 m/s	31.25 meters	YES
K-1	15%	20%	70 meters	18.3 meters	115 meters 20 Hertz 2300 m/s	28.3 meters	NO

Table 1.2 Vertical resolution computed in the two interest intervals from wells S-1 and K-1.

García, 1976; Echánove-Echánove, 1976, 1986; Pérez-Cruz, 1992; Eguiluz et al., 2001). To date, the Vicksburg Formation has produced more than 300 Tcf of gas in the Burgos Basin since production began in the 1940's.

Cumulative production data from major fields and recently drilled wells was made available for this study (see production tables in Appendix D).

1.5 GEOLOGICAL SETTING

During the Cenozoic a thick sedimentary wedge was deposited in the Burgos Basin. Clastic sediments within this wedge range from conglomerates to shales and also include some beds of volcanic ash, and tuffs (Busch, 1973; González-García, 1976; Pérez-Cruz, 1992; PEMEX, 1994).

The three major depocenters in the Gulf Coast Basin, including northern México, are the Rio Grande Embayment, the Houston Embayment, and the Mississippi River Embayment (Figure 1.3) (Winker, 1982; Galloway, 1989a, 1989b; PEMEX, 1993).

1.5.1 Structure

In the Tertiary Burgos Basin more than 10,000 meters of Cenozoic sediments record periods of regional extension and shale flowage. During the Cenozoic, the uplift of the Rocky Mountains increased clastic sedimentation within an overall eastward progradation in the northwestern Gulf of México (Winker, 1982; Galloway, 1989a,b; Pérez-Cruz, 1992; Hernández-Mendoza, 2000). These clastic sequences prograded over the Cretaceous carbonate

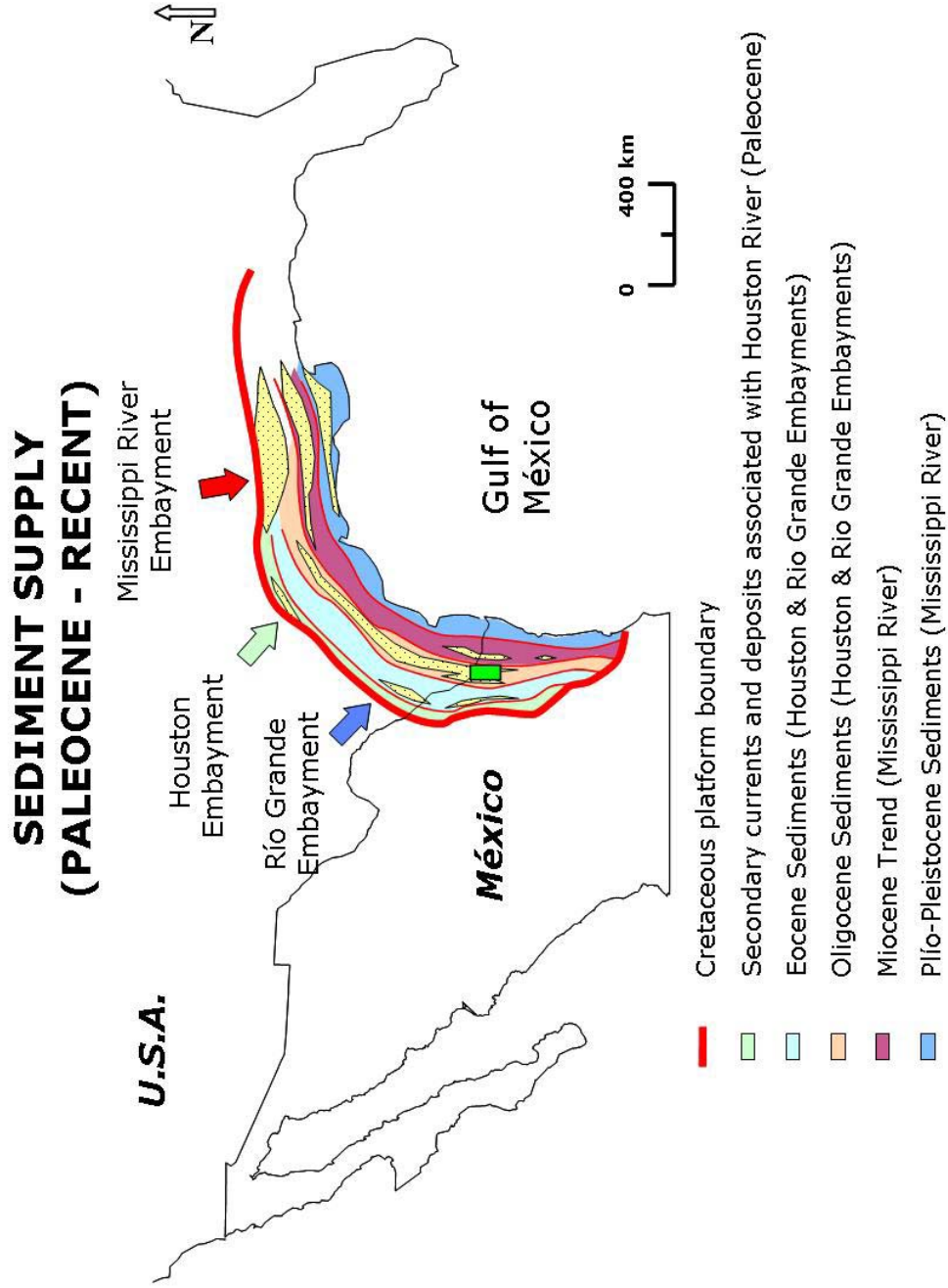


Figure 1.3 Major depocenters postulated in Texas Coast and Northern México. Compiled from Galloway (1989) and Chevron/PEMEX (1993).

platform margin and include a fluvial to inner deltaic massive sand facies, a deltaic plain to prodeltaic facies, a neritic sand facies with interbedded shales, and a massive, outer neritic and bathyal, dominantly shaly, facies with some turbiditic sands (Winker 1982; Bally, 1989).

The Lower Oligocene Vicksburg deltaic deposits are involved in complex structures characterized by numerous growth faults (Busch, 1975) and shale diapirism. Progradational deltaic deposition associated with faults resulted in rotated and subsiding sedimentary wedges; thus rotation and expansion of the section along growth faults controlled the thickness of the deltaic deposits (Langford and Combes, 1994). Sediments are thickest close to the glide-plane contact and thin down depositional dip. Connecting the major growth faults of the Vicksburg sediments is a detachment surface that dips gently eastward, which has been referred to as a glide plane (Han, 1981; Han and Scott, 1981; Berg and Habeck, 1982; Bruce, 1983; Hastings, 1984; Hill et al., 1991; Langford and Combes, 1994; Whitbread et al., 2001).

The Vicksburg Formation was deposited on a shelf-margin (Figure 1.4), and shares its characteristics with other deltaic sequences built on unstable substrates (Edwards, 1980; Straccia, 1981; Suter and Berryhill, 1985; Mayall et al., 1992). Shelf-margin deltas have a distinctive depositional style that contrasts with deltas deposited in stable tectonic environments (Sutter and Berryhill, 1985; Mayall et al., 1992).

Shelf-margin deltaic deposits are economically important hydrocarbon reservoirs involved in combined structural and stratigraphic traps that developed

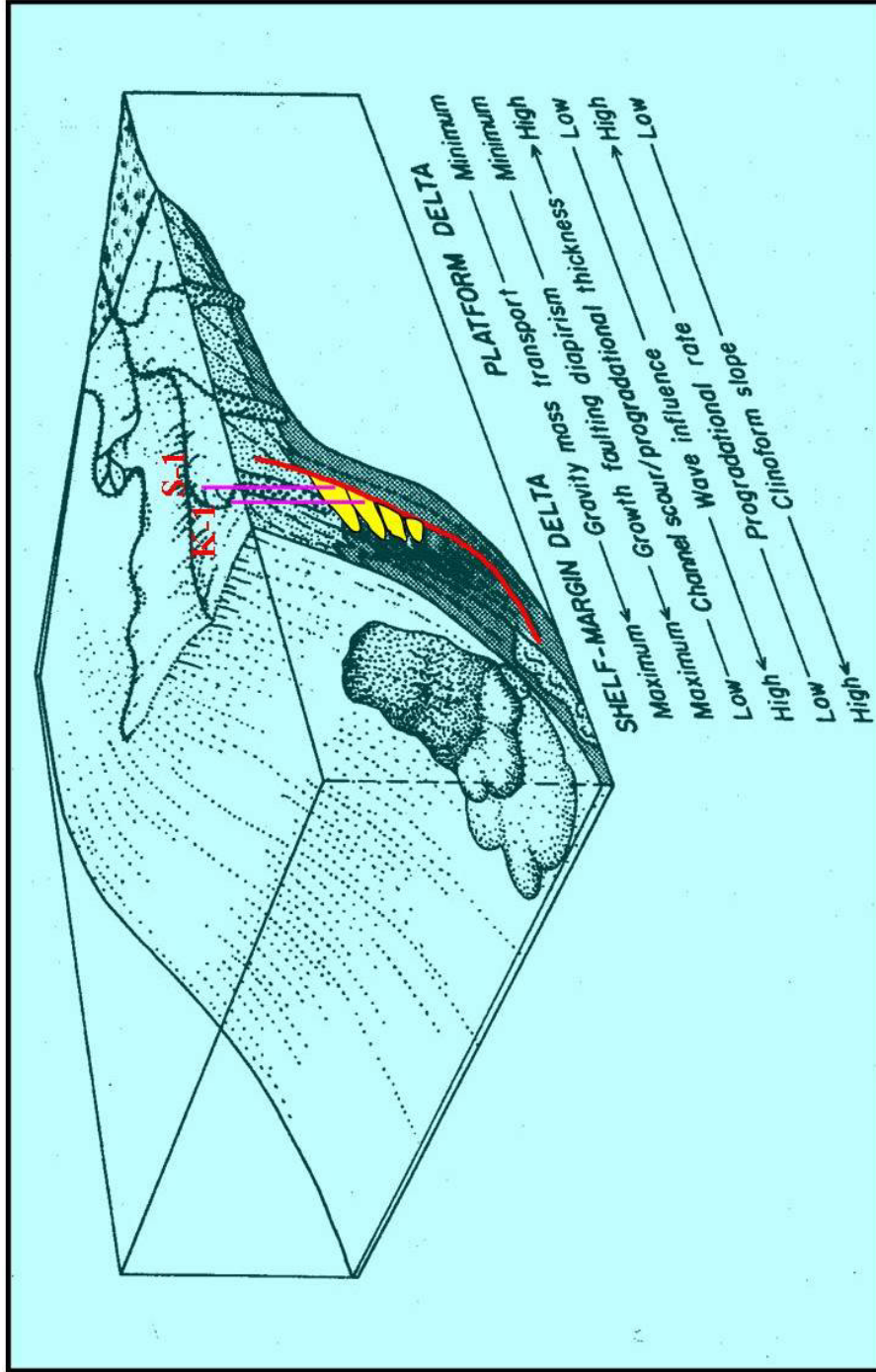


Figure 1.4 Depositional structural models of the Vicksburg Formation in the Burgos Basin. The positions of S-1 and K-1 wells are displayed (Modified from Galloway and Hobday, 1996).

during contemporaneous deformation and deposition. Therefore, it is important to know the style of deposition in shelf margins for locating and producing hydrocarbons.

1.5.2 Vicksburg Petroleum System

The Vicksburg Formation petroleum system can be characterized as follows:

- Source rock from the Midway and Wilcox Formations is composed of marine shales with total organic carbon (TOC) ranging from 0.1% to 1.5%, Ro from 0.5% to 1.9%, and Hydrogen Index varying from 100 to 150, (Eguiluz et al., 2001; PEMEX, 2002).

- The reservoir rock is characterized by deltaic sandstones with porosities ranging from 12% to 28% and net thickness from 8 to 40 meters (Eguiluz et al., 2001; PEMEX, 2002).

- The traps are associated with anticlines related to growth faults and rollovers on the detachment sites of the faults, where the seal is marine shales (Eguiluz et al., 2001; PEMEX, 2002).

- Timing and migration: The Paleocene started hydrocarbon generation at Early Eocene (48 ma), and the Wilcox Eocene started in the Middle Eocene.

Therefore, the best synchrony is in the Vicksburg play itself (Eguiluz et al., 2001; PEMEX, 2002).

1.5.3 Oligocene Stratigraphy and Biostratigraphy

Four Oligocene stratigraphic units are clearly identified in the Burgos Basin: the Norma Conglomerate and the Vicksburg, Frio, and Anahuac Formations (Figure 1.5). They were deposited during two major transgressive-regressive cycles. In the following, condensed descriptions of the Oligocene stratigraphic units are summarized in tables 1.3 to 1.5.

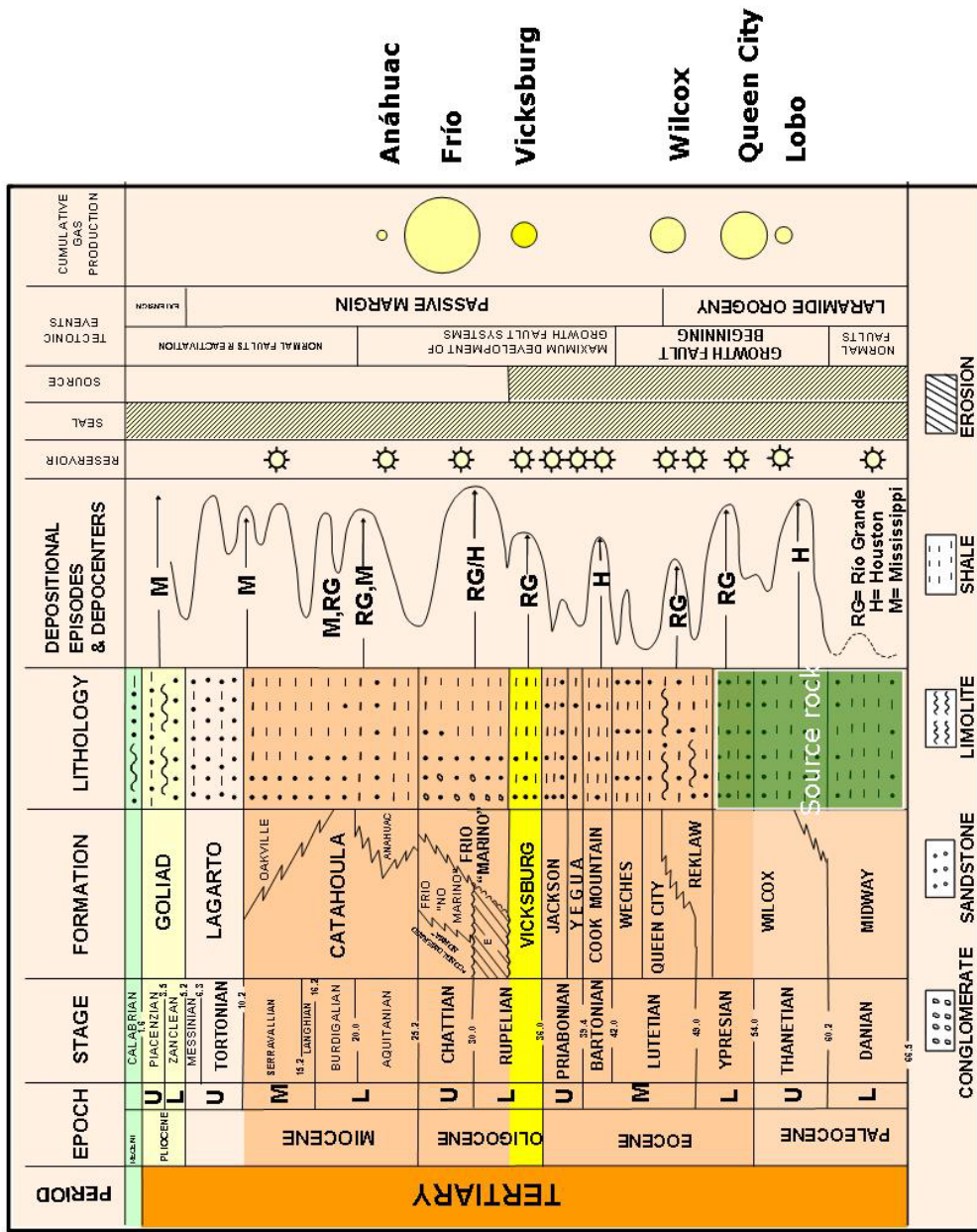
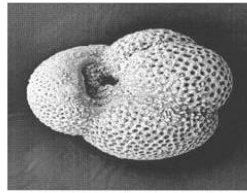


Figure 1.5 Geologic column of the Tertiary in the Burgos Basin, México (Modified from Galloway, 1986a, b).

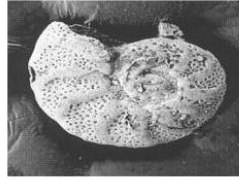
Lithostratigraphic Unit	Vicksburg Formation
Lithology	Shales and siltstones with some intercalations of fine sand
Thickness	Varies from 0 to more than 3,000 m.
Distribution	Widespread along north-south-oriented elongated depocenters
Stratigraphic relationships	Conformably overlies Eocene rocks and underlies the Norma Conglomerate and Frio Formation to the west and east, respectively
Fossil content	<i>Globigerina ampliapertura</i> biozone (Figure 1.6)
Depositional environment	Deep marine basin (outer neritic-upper bathyal); <i>Textularia warreni</i> , <i>Cibicides mexicana</i> (Cavazos-Prado, 1969).

Table 1.3 Lower Oligocene (Vicksburg Formation).

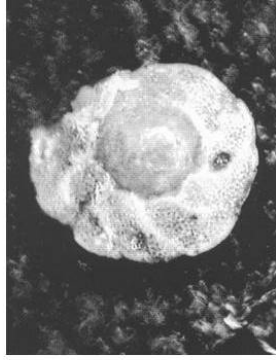
VICKSBURG INDEX FOSSILS
 32.4 – 36.0 m.a. (Rupelian)
 Early Oligocene
 P18 & P19



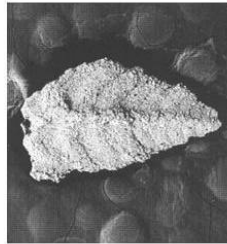
Globigerina ampliapertura



Anomalina bilateralis Cushman



Cibicides pipeni



Textularia warreni Cushman and Ellisor



Textularia mississippiensis Cushman



Bulimina sculptilis



Figure 1.6 Index fossils of Early Oligocene in the Burgos Basin (PEMEX, 1994).

Lithostratigraphic Units	Continental facies: Norma Conglomerate Marginal facies: Frio Formation (non-marine member) Marine facies: Frio Formation (marine member)
Lithology	Continental facies: Conglomerate formed by fragments up to 40 cm in diameter derived from igneous and sedimentary rocks. Marginal facies: Shales and sands. Marine facies: Silts, and shales with some sands.
Thickness	Norma Conglomerate: Varies from 0 to 300 meters. Frio Formation (marginal facies): Varies from 0 to more than 2,000 m. Frio Formation (marine facies): Varies from 0 to more than 1,000 m.
Distribution	The Norma Conglomerate is present along a narrow north-south band that extends east to the McAllen-Reynosa fault system. The non-marine member of the Frio Formation extends further east to the 18 de Marzo fault system, intertonguing with the marine member. The marine member is expected to be present under the Tamaulipas shelf (offshore) beneath thick Miocene deposits. The Norma Conglomerate unconformably overlies rocks of the Vicksburg and intertongues with the non-marine member of the Frio Formation. The non-marine member overlies deposits of the Vicksburg Formation and intertongues with the marine member deposits.
Fossil content	<i>Oogonids</i> of <i>Chara</i> , <i>Ostracoids</i> , <i>Cibicides hazardii</i> , <i>Marginulina texana</i> , and <i>Nodosaria blanpiedi</i> biozones (Cavazos-Prado, 1969)
Depositional environment	Continental to deep marine basin.

Table 1.4 Middle Oligocene (Norma Conglomerate and Frio members).

Lithostratigraphic unit	Anahuac Formation
Lithology	Siltstones and shales with minor proportion of fine sandstones
Thickness	From 0 to about 1,000 m
Distribution	Widespread-present to the east of the McAllen-Reynosa fault system, becoming thicker eastward.
Fossil content	<i>Discorbis nomada</i> (<i>Discorbis</i> biozone); <i>Elphidium rota</i> , <i>Heterostegina texana</i> , and <i>Bolivina perca</i> (<i>Heterostegina</i> biozone), <i>Marginulina idiomorpha</i> , <i>Marginulina mexicana</i> , and <i>Marginulina howei</i> (<i>Marginulina</i> biozone) (Cavazos-Prado, 1969).
Depositional environment	Shallow marine

Table 1.5 Upper Oligocene (Anahuac Formation).

Chapter 2

Structural and Stratigraphic Environments of Natural Gas Reservoirs in the Vicksburg Flexure Expanded Sediments in the Burgos Basin, Northern México

2.1 INTRODUCTION

Gas reservoirs in the Vicksburg Formation in the Burgos Basin, northern México, are highly productive down-dip of growth faults. The gas fields trend north-south and display growth faults, counter-regional faults, dip-reversal, and low-angle detachments as their structural characteristics (Busch, 1973, 1975; Pérez-Cruz, 1992; Kosters et al., 1989; PEMEX, 2002).

This chapter analyzes the regional structural and stratigraphic framework of the Burgos Basin based on the interpretation of two dip-oriented seismic transects and a detailed study of the 3D survey acquired over the major gas fields, Misión (47.1 Tcf) and Lomitas (49.6 Tcf) (See Appendix D, Table D.2).

2.2 REGIONAL STRUCTURAL FRAMEWORK

The Vicksburg Formation of the Burgos Basin is affected by numerous growth faults and post-depositional faults (Busch, 1975, PEMEX, 1994, 2002). The sediment thickness expands greatly into the growth fault zone, and structural features become more complex with increasing depth.

Progradation of deltas across an unstable shelf margin occurred during Early Oligocene time. The progradation was associated with syndepositional

faulting, eastward movement of undercompacted Jackson Formation shales, and the formation of complex salt structures. Thus the accommodation space necessary to deposit large amounts of sediment was created (Fisher, 1969; Fisher et al., 1969; Picou, 1981; Winker and Edwards, 1983). Structural closures formed in rollover anticlines segmented by faults associated with growth faulting. Growth faults are curvilinear in map view, with the orientation slightly north-south and continuous over several kilometers; in a regional context they form a series of sub-parallel structural blocks of sediments. These blocks have been identified from west to east as Becerro, McAllen-Reynosa, Altamirano, Brasil, and 18 de Marzo (Busch, 1973, 1975; González-García, 1976; Echánove, 1976, 1986). The study area presented here is within the Becerro block (Figure 2.1). To show the structural behavior of the Cenozoic units, I interpreted two dip-oriented seismic profiles across the Burgos Basin.

2.2.1 Seismic Transect I

Seismic transect I is oriented northeast-southwest and is 220 km long (Figure 2.2). The western portion of this seismic transect depicts the structure of a region located 60 km northeast of Monterrey City, near the Sierra Madre Oriental frontal ranges; it shows a general shallowing and folding of the basement in response to Laramide compressional deformation. The Upper Jurassic and Cretaceous thicken toward the southeast. In the western portion of this seismic line, a broad, symmetric, basement-involved anticline can be observed, where the Refinería-1 well was drilled; toward the east, other minor basement-involved

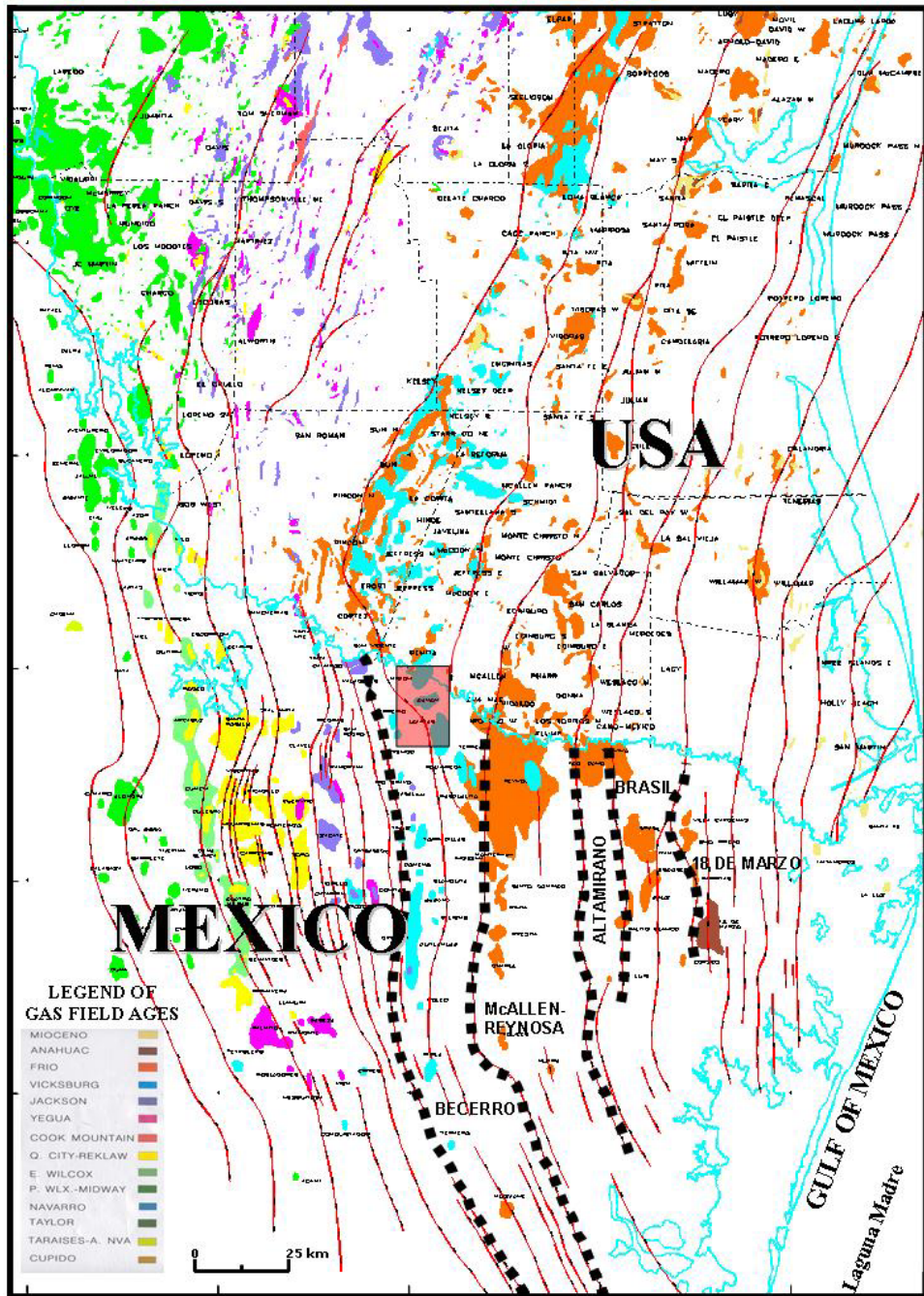
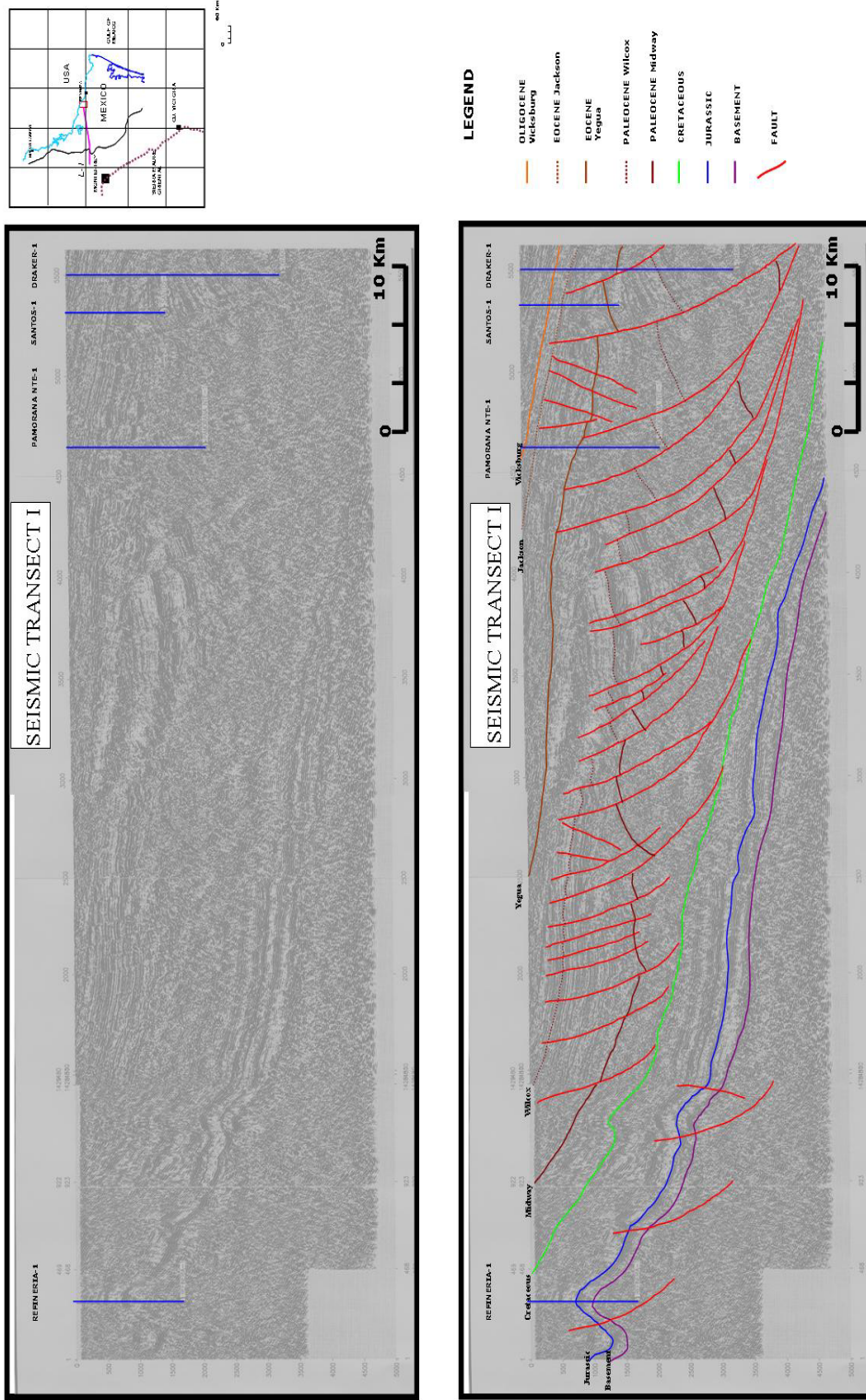


Figure 2.1 Structural compilations for South Texas and Northern Mexico, showing the spatial distribution of fields and fault systems at 1.5 seconds of two-way time. Five structural blocks have been defined, each bounded by growth faults that are continuous and follow a curvilinear pathway. (Modified from PEMEX, 1994).



folds are present along a gentle monocline where the Upper Jurassic units are very thin.

Proceeding eastward between CDP's 3000 and 5000, transect I shows a system of basinward dipping growth faults associated with a dramatic expansion of the Paleocene section. These growth faults merge into a decoupling level on the top of Cretaceous and affect the overlying stratigraphic units. A large, highly rotated fault block is observed in Pamorana Nte.-1 well. The variation in the structural style may be due to an increase in basinward dip of the top Cretaceous, which is not likely, as that would rotate the Mesozoic. The increased dip in the Cretaceous may be purely a velocity effect.

In the easternmost portion of this line, within the 3D study area, the main growth fault system of the Lower Oligocene Vicksburg Formation is highly rotated and expanded. In this portion of the line, the decoupling level is near the base of the Jackson Formation.

2.2.2 Seismic Transect II

Seismic transect II is a composite regional seismic profile that is 480 km long (Figure 2.3), from the Vaquerías anticline in the west, to the continental slope of the Tamaulipas shelf in the east. Mesozoic units in the west portion of this seismic transect are gently folded and cut by basement-involved thrusts. These structures tend to increase in depth toward the east. Down-to-the-basin growth faults, between CDP's 9000 and 6000 that cut Paleocene, Eocene, and Oligocene units can be identified and appear to converge on the top of

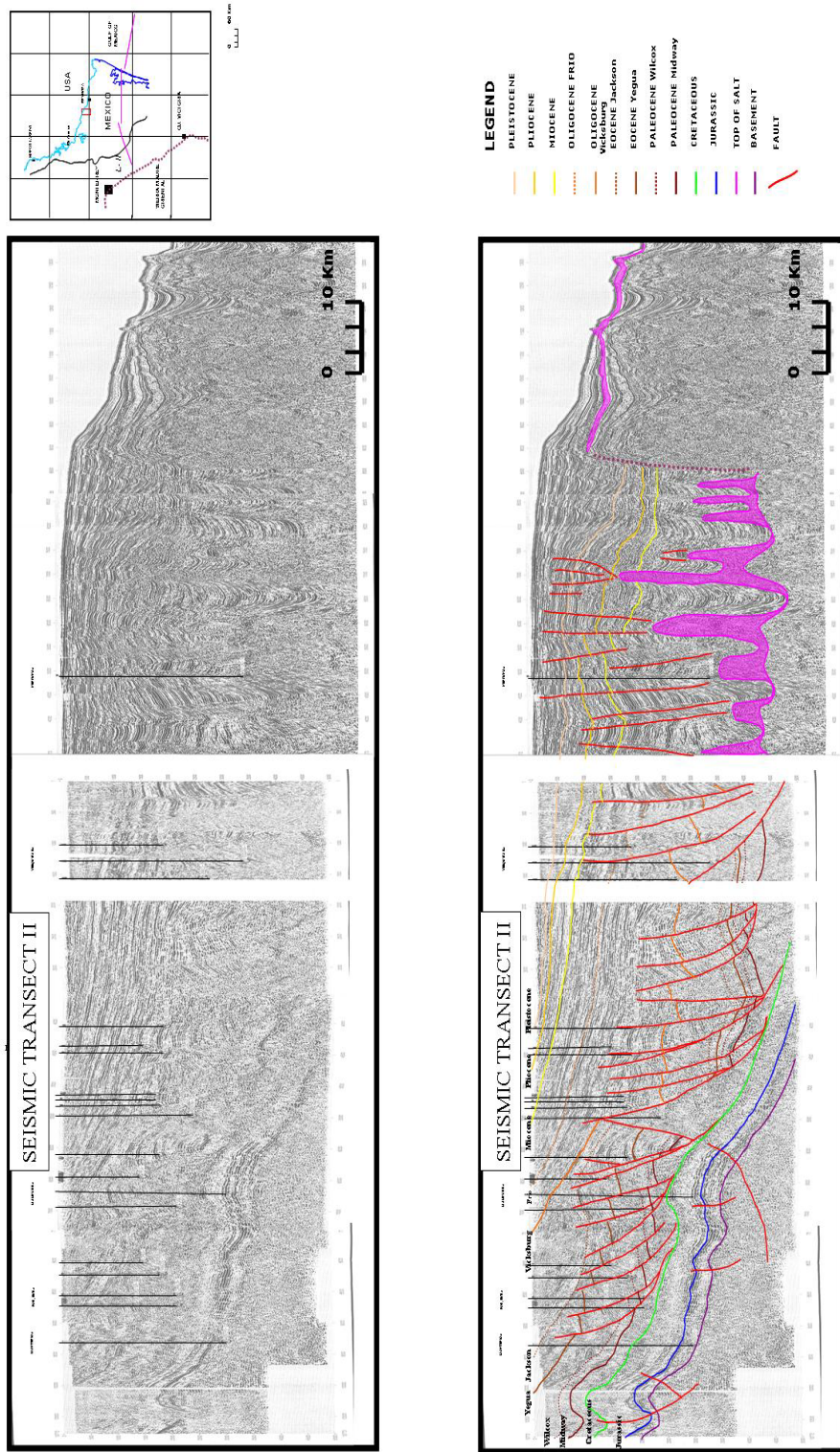


Figure 2.3 Dip-oriented seismic transect II displays the structural styles affecting Cenozoic and Mesozoic strata in the Burgos Basin. Structural features include an extensional system characterized by growth faults that affect clastic Cenozoic units and a compressional system that is deforming the carbonate Mesozoic rocks. A decoupling level can be observed between both structural systems. Salt bodies are part of an allochthonous salt body that has been reported by Diegel et al., (1995) and Peel et al. (1995).

Cretaceous. These thrusts may define a compressional regime characterizing post-Oligocene tectonics.

Between CDP's 6300 and 5500, there is a structural block where the Tenampa-1 and Argentina-1 wells were drilled, bounded on the west by a low-angle growth fault with an associated rollover anticline and a counter-regional fault in the east.

The Paleogene structural style of deformation changes drastically toward the east, close to the coast line. Synthetic normal faults become more closely spaced, reflect activity during the Miocene, and apparently detach within the Eocene units. Further east, there is a collapsed anticline where the Neptuno-1A well was drilled. This fold is characterized by normal faulting and stratal rotation, associated with shale mobilization and salt withdrawal. The easternmost portion of this seismic transect is characterized by a series of deep troughs, mainly filled with Miocene-Pliocene sediments separated by salt intrusions associated with an allochthonous salt mass.

2.2.3 Growth Fault Patterns in South Texas and Northern México

Differences between growth fault patterns in South Texas and northern México can be illustrated by the seismic profiles displayed in Figure 2.4. Seismic profile A is from onshore South Texas and seismic profile B is from onshore northern Mexico. The first profile shows a growth fault with a shallow low-angle detachment, and the second profile shows a tilted growth fault system with a deep

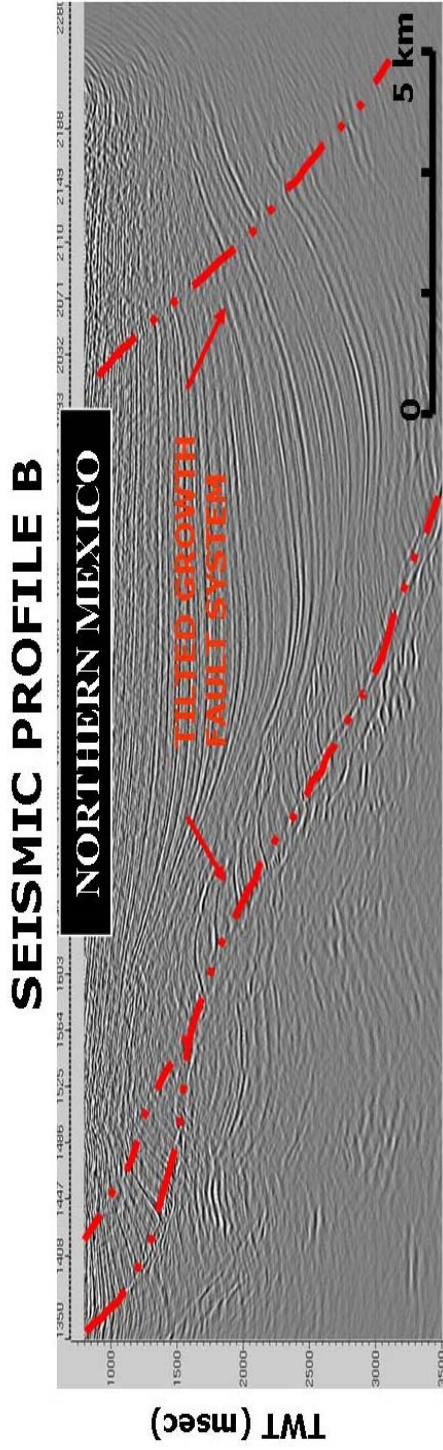
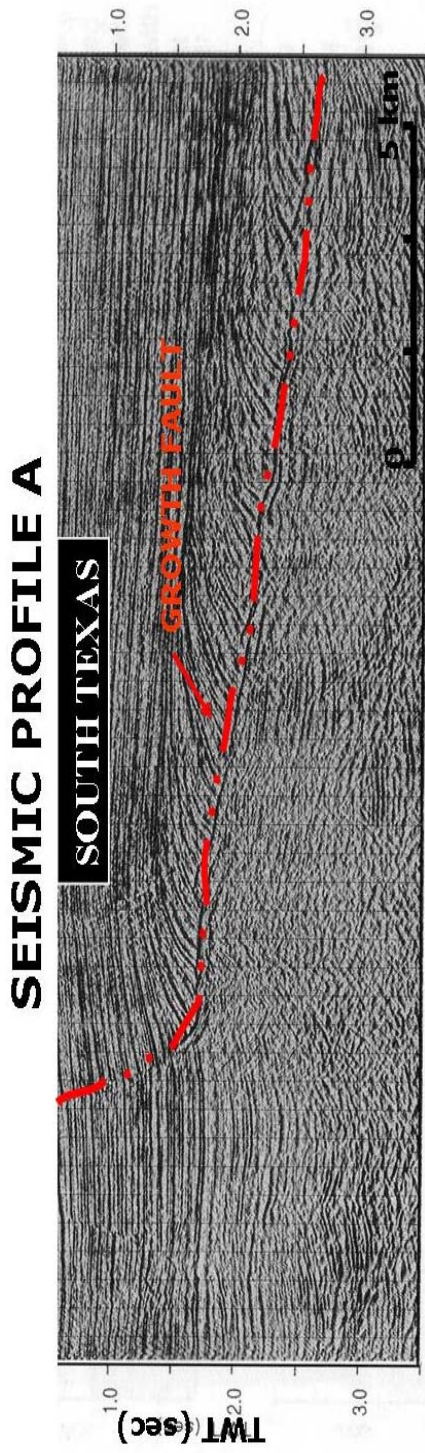


Figure 2.4 Dip-oriented seismic profiles displaying the structural styles affecting Cenozoic rocks in South Texas (A) and northern Mexico (B). A growth fault with a low-angle detachment level can be observed in A, and a tilted growth fault system with a deep detachment is shown in B.

detachment. The difference in growth fault pattern was caused by the uplift of the Mexican Plateau in post-Oligocene times.

2.2.4 Reservoir Structural Habitat

Vicksburg gas reservoirs in the Burgos Basin are highly productive. The largest fields include Cuitláhuac, Pascualito, Lomitas, Misión, and Polvareda (see gas reserves in Appendix D, table D.2).

The rapid deposition of sediments triggered syndepositional growth faulting at shelf margins associated with salt and shale mobilization. Growth faults have been studied by many authors, including investigations of triggering mechanisms of fault motion by Currie (1956), Bruce (1972), Busch (1975), and Galloway (1986a,b), clay models by Cloos (1968), and the relationship between growth faulting and shelf margins by Winker (1982), Diegel et al. (1995), and Peel et al. (1995).

In general, growth faulting leads to an expanded stratigraphic section and horizontal displacements greater than vertical displacements. Galloway (1986b) recognized three growth-fault patterns that form in response to the depositional and structural setting: (1) a growth fault pattern associated with rapidly prograding major deltaic headlands in which the faults are closely spaced; (2) a growth fault pattern associated with prograding interdeltic margins; and (3) a growth fault pattern associated with gravity-glide (Diegel et al., 1995).

Major gas reservoirs in the Burgos Basin are related to curvilinear and linked growth fault systems. Varying delta morphologies occur in the Vicksburg

sediments as a result of the interaction between progradation, subsidence, and marine reworking.

2.3 ANALOGUE RESERVOIRS WITH SOUTH TEXAS

Some gas fields on the downdip side of the Vicksburg Flexure; for example, McAllen Ranch, Javelina, and East McCook fields in Texas (Hastings, 1984; Kosters et al., 1989; Hill et al., 1991; Langford et al., 1992; Langford and Combes, 1994), and Cuitláhuac field in México (PEMEX, 2002), lie within the same growth-fault trend; therefore, structural setting and trapping mechanisms may be compared. Other analogous fields that share the same structural block are Misión, Cañón, and Lomitas fields located in México, which are on trend with the Monte Cristo field in Texas (PEMEX, 2002)

Vicksburg reservoirs in the Burgos Basin exhibit common stratigraphic characteristics similar to those in South Texas. Major flooding surfaces that define the Vicksburg stratigraphy can be interpreted and correlated on both sides of the Rio Grande, and the producing intervals in the South Texas fields can be identified in the same stratigraphic sequence intervals of the Burgos Basin (PEMEX, 2002).

2.4 STRATIGRAPHIC UNITS

The Vicksburg Formation in the Burgos Basin is a lower Oligocene clastic sequence that underlies the Frio Formation; deposition of the Vicksburg Formation marks the initiation of coarse sediments from the Sierra Madre

Oriental that produces a regional progradational pattern (Rainwater, 1964; Hardin, 1967; Loucks, 1978).

The Vicksburg Formation is extremely complex because it slides on the unstable shales of the Jackson Group. In this study, a stratigraphic framework was performed by the identification and correlation, based on flooding surfaces, of six stratigraphic units, named A to F, within the Vicksburg Formation; these units are constrained to fault-bounded, structurally-defined provinces. The stratigraphic framework is similar between South Texas and northern México because the major flooding surface marker horizons that define Vicksburg stratigraphy in the Burgos Basin can be correlated north into Texas, as shown on the type log (Figure 2.5). Furthermore, the producing intervals in the South Texas fields were identified and assigned to the equivalent genetic stratigraphic intervals of the Burgos Basin. The depositional architectures of delta-flank, shoreface, and beach ridge facies as well as delta-mouth-bar and distributary channels facies in the Texas Vicksburg reservoirs are also comparable to those in the Burgos Basin, (PEMEX, 2002).

Well correlation analysis and detailed seismic interpretation were done across the 3D survey. In this study, I focused on sequences D and E, which involve the main reservoirs down-dip growth faults in the southern portion of the 3D survey. In Figure 2.6 a dip-oriented well correlation transect A-A' through the growth fault is shown with the distribution of the interpreted stratigraphic sequences. The datum in the well correlation transect is the sequence boundary 30 ma, which represents a substantial intraformational unconformity within the Frio

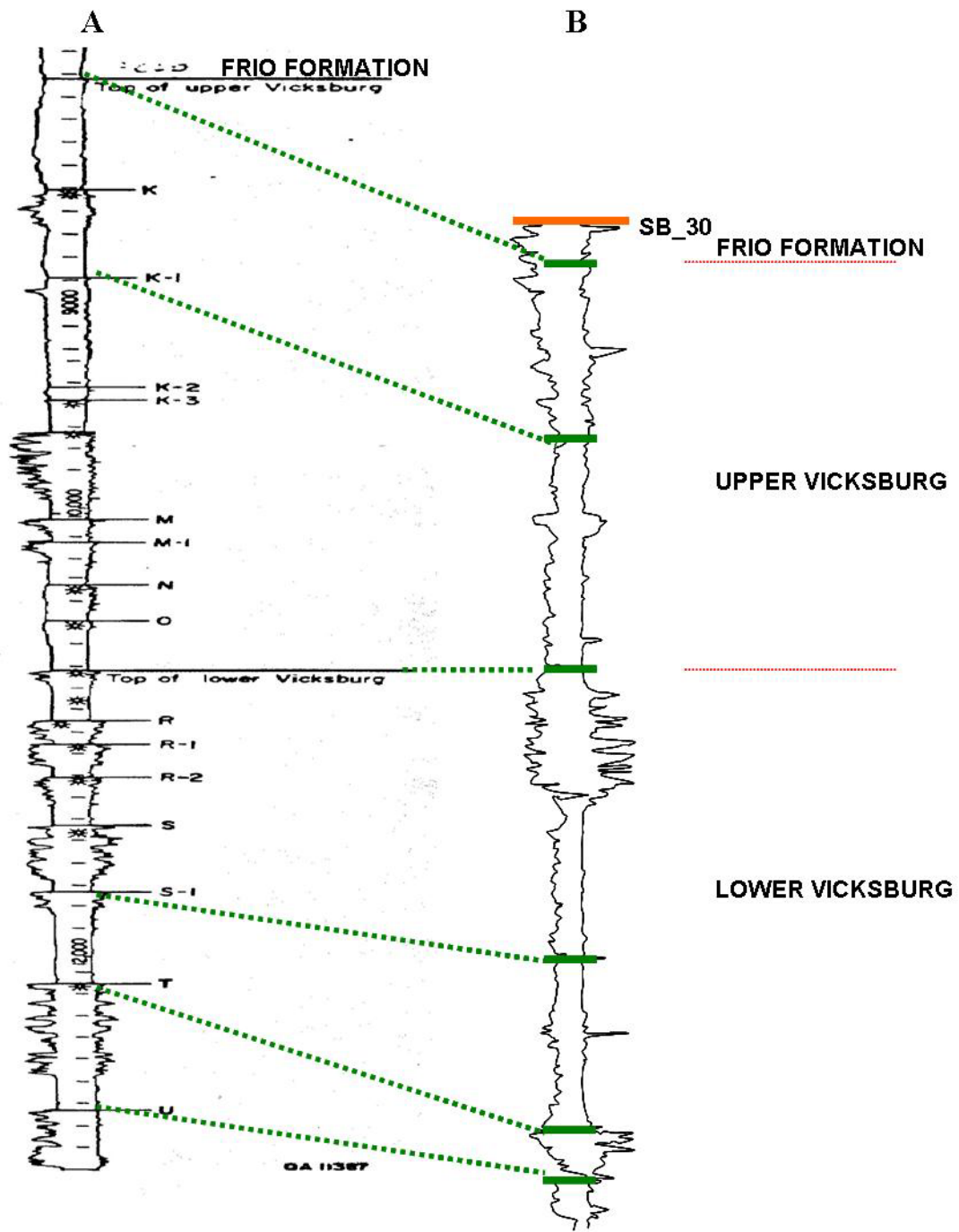


Figure 2.5 Log type showing the stratigraphic units and major flooding surfaces that define Vicksburg stratigraphy in South Texas, (A) and correlated in the Burgos Basin (B).

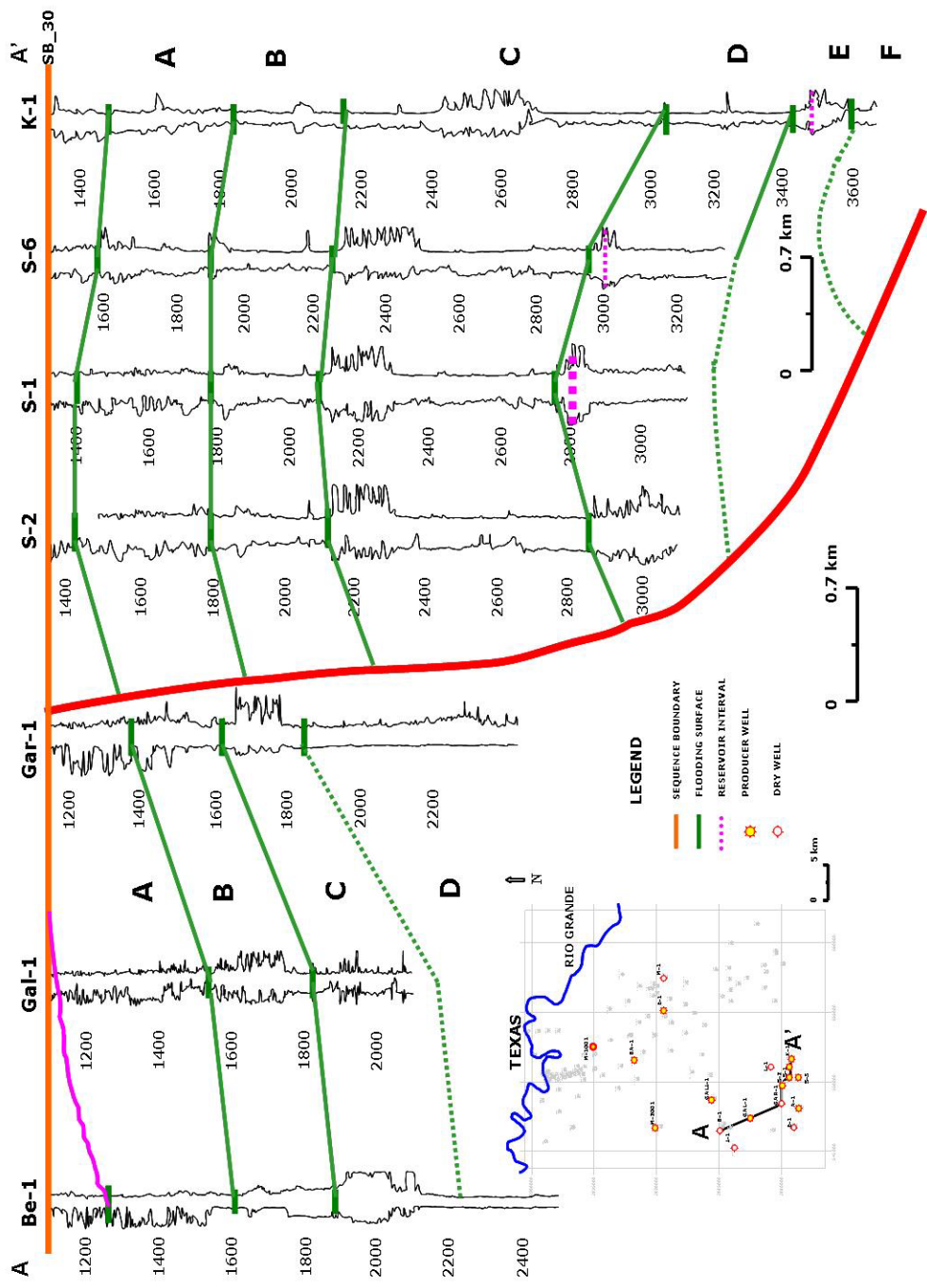


Figure 2.6 Dip-oriented well correlation transect A - A' showing the relationship prime between up-thrown and down-thrown sequences.

Formation that was recognizable on the seismic data. The expansion of the stratigraphic sequences in the down-dip direction due to the effect of the growth fault is clear.

2.5 3D SEISMIC INTERPRETATION

Detailed seismic interpretation was performed on the seismic volume with a Silicon Graphics® workstation using Seisworks® interactive interpretation software by correlating the sequence boundaries defined in boreholes and identifying the master growth fault in the west portion of the area. The inlines, north-south oriented, represent strike direction, and the crosslines, east-west oriented, show the dip direction.

2.5.1 Methodology

The methodology used to interpret the seismic volume involves six steps:

1. Load seismic data in SEG-Y format files into workstation
2. Load well logs in .las format and tops in ASCII format in Seisworks®
3. Tie wells to seismic data with synthetic seismograms
4. Identify faults in the area using dip, strike, and random lines, as well as time slices
5. Pick seismic horizons across the whole survey
6. Map reflecting horizons.

2.5.2 Crossline 200

Crossline 200 is a dip-oriented seismic transect extracted from the southern portion of the 3D seismic volume. The structural seismic section shows the interpretation of sequences A to F of the Vicksburg Formation interval. The sedimentary sequences are affected by normal faults, which regionally create down-dip eastward expansion of sediments. Unconformity surfaces covered by thick muddy units provide good seals for gas traps (Figure 2.7).

2.5.3 Inline 1700

Inline 1700 is a strike-oriented seismic line extracted from the center of the 3D survey (Figure 2.8). This section shows the vertical distribution of the sequences from south to north. A listric master fault is interpreted with a low-angle detachment level located between the base of the Vicksburg Formation and the top of the Jackson Formation. The sequences are expanded close to the fault, suggesting contemporaneous fault movement and sediment supply.

2.5.4 Time Slice Analysis

Time slice sequence analysis is shown in Figure 2.9 A, B, and C. Figure 2.9 A corresponds to a structural map on a time surface from 1000 ms of two-way time, B shows a time slice extracted from 2000 ms of two-way time and C displays a time slice from 2700 ms of two-way time. A master growth fault in the west portion of the area is a dominant feature in all of the slices. This growth fault trends northeast-southwest and branches in the northern portion to increase

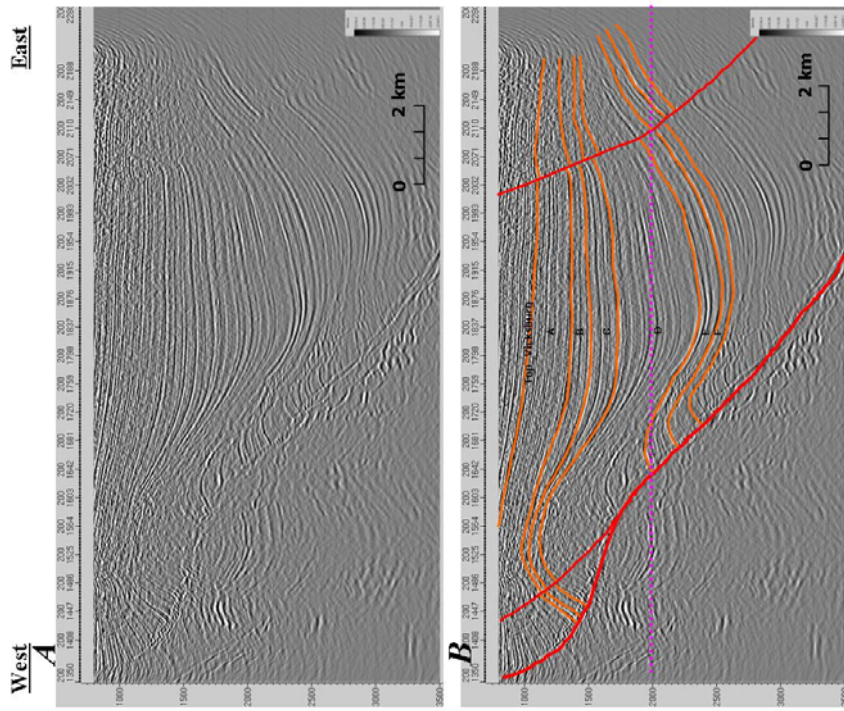


Figure 2.7 Dip oriented crossline 200. (A) Seismic profile without interpretation. (B) Interpreted line across main anticline production trend. The growth fault, in red, expands the Vicksburg sequences. The dotted purple line shows the position of the extracted time slice. (C) Uninterpreted time slice. (D) Time slice at 2000 milliseconds of two-way-time showing the normal fault system as well as the main structural characteristics: anticline shadowed in yellow and synclines in green.

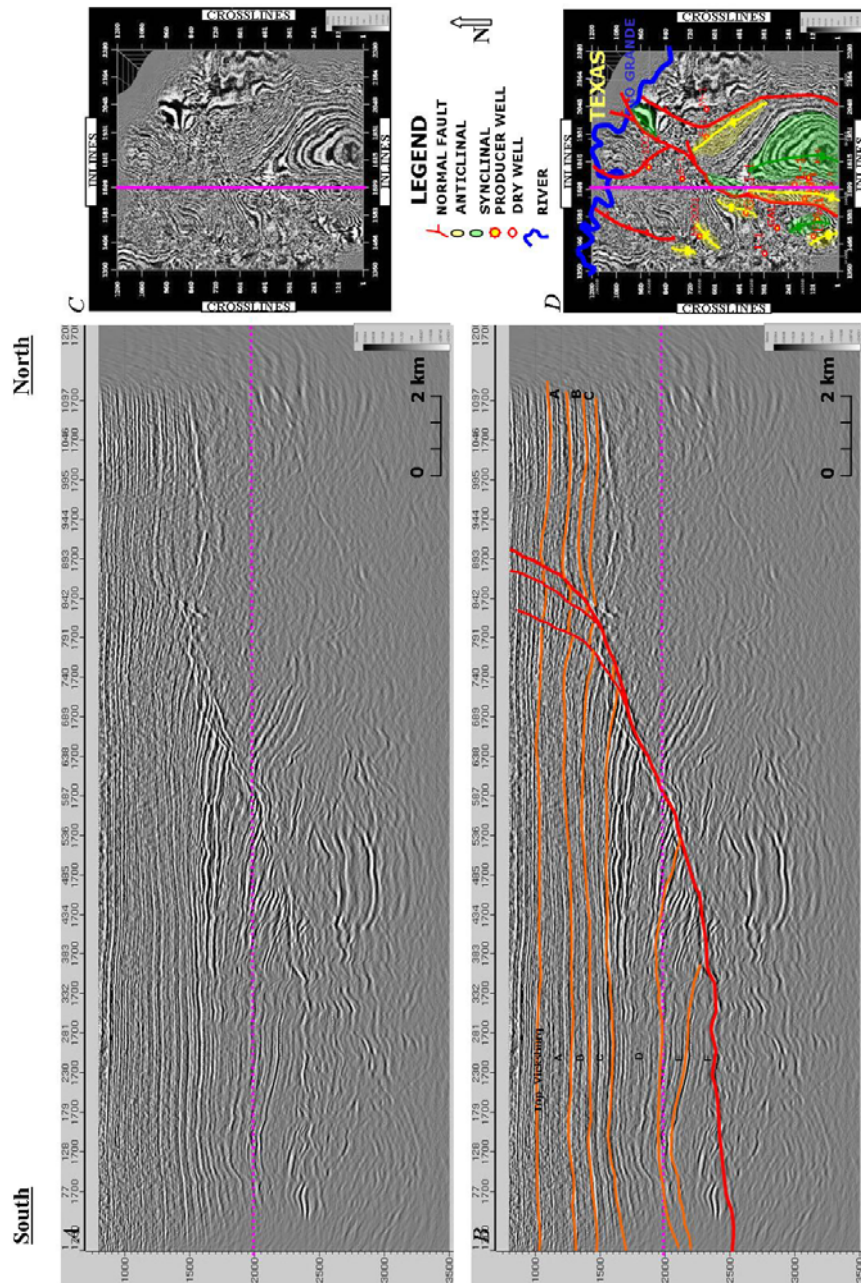


Figure 2.8 Strike-oriented inline 1700. (A) Seismic profile without interpretation. (B) Interpreted line showing the listric normal fault affecting the Vicksburg sequences defined in this study. The dotted purple line shows the position of the extracted time slice. (C) Uninterpreted time slice at 2000 ms. (D) Interpreted time slice showing the structural features. The growth fault path, in the center of the slice, is curvilinear.

Time Slice at 1000 milliseconds

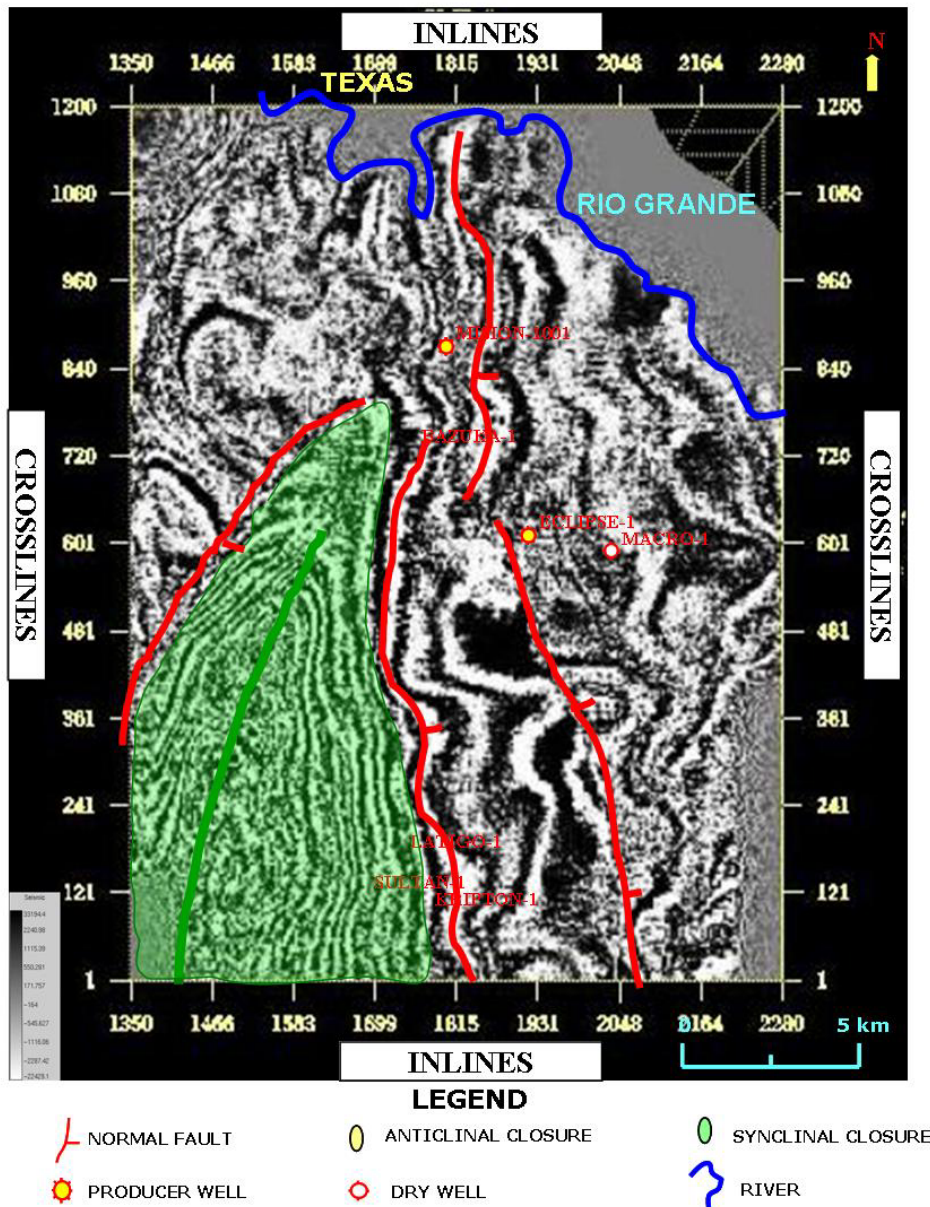


Figure 2.9A Time slice at 1000 ms of two-way time. This time slice shows the structural characteristics found in the study area as two way time increases. In general, growth fault system is displayed in curvilinear patterns, oriented NNE-SSW. The master growth fault is branched in the north portion of the survey, increasing the structural complexity. Narrow and elongated anticlines are present, and a wide syncline in the south portion of the area represents a local depocenter.

Time Slice at 2000 milliseconds

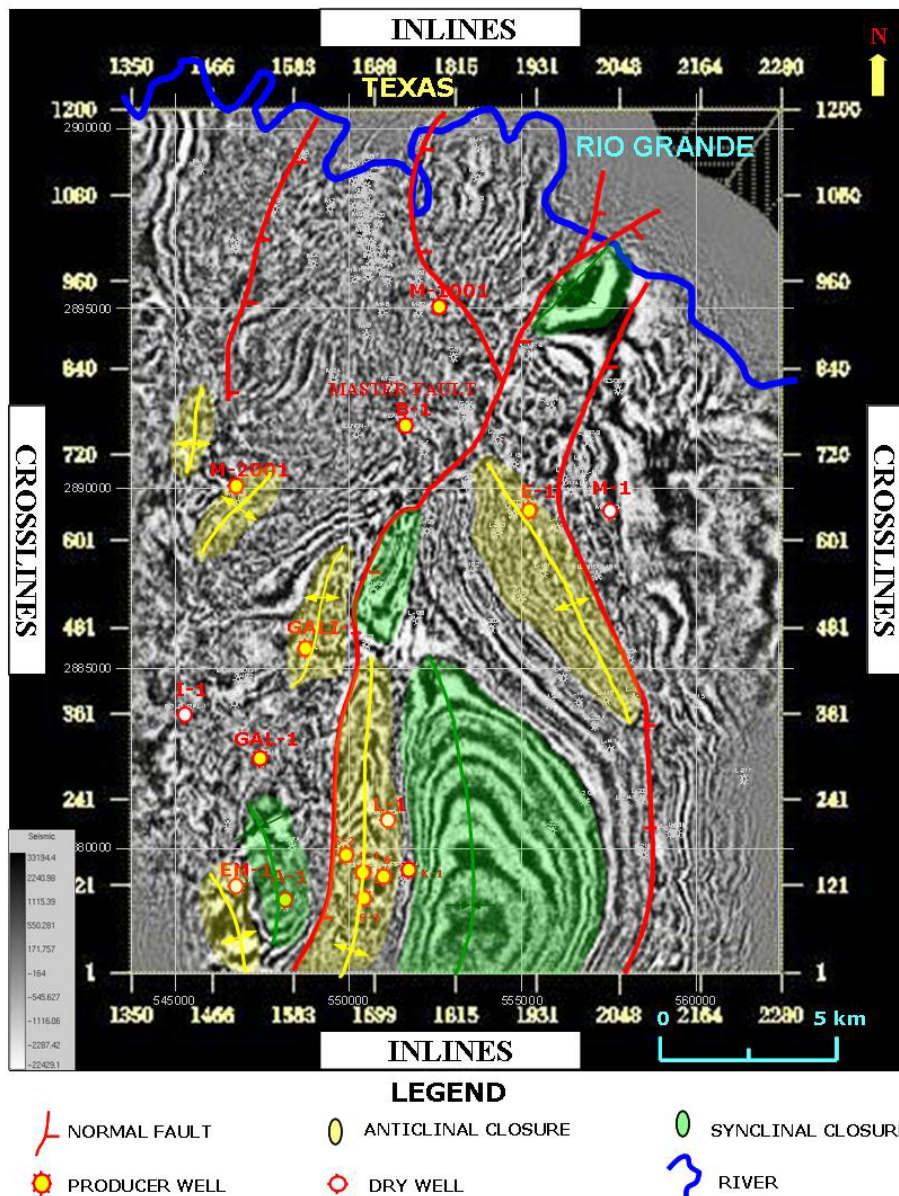


Figure 2.9B Time slice at 2000 ms of two-way time and. This slice shows the structural characteristics found in the study area as two-way time increases. In general, growth fault system is displayed in curvilinear patterns, oriented NNE-SSW. The master growth fault is branched in the north portion of the survey, increasing the structural complexity. Narrow and elongated anticlines are present, and a wide syncline in the south portion of the area represents a local depocenter.

Time Slice at 2700 milliseconds

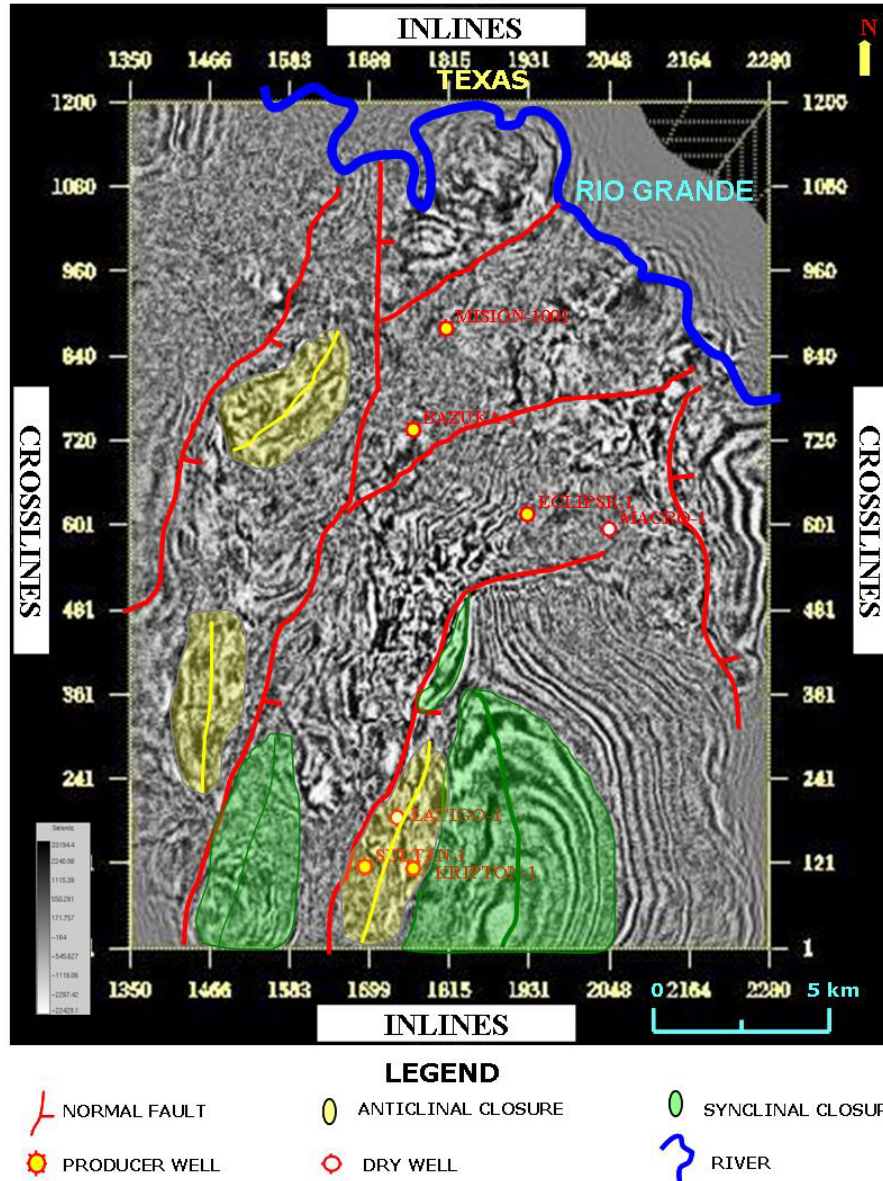


Figure 2.9C Time slice at 2700 ms of two-way time. High amplitude anomalies up-dip growth fault are present. This slices shows the structural characteristics found in the study area as two-way time increases. In general, growth fault system is displayed in curvilinear patterns, oriented NNE-SSW. The master growth fault is branched in the north portion of the survey, increasing the structural complexity. Narrow and elongated anticlines are present, and a wide syncline in the south portion of the area represents a local depocenter.

structural complexity. A narrow, long anticline exists down-dip of the growth fault, and a wide, broad syncline is observed just eastward in that area. Up-dip growth fault can be seen high-amplitude structures at time slice 2700 ms as potential gas traps placed in over-pressured sediments.

2.5.5 Isochron map of 32.4 ma sequence boundary

The isochron map of 32.4 SB represents the top of the Vicksburg Formation in two-way time or 32.4 ma sequence boundary. In this map, the behavior of the top Vicksburg seismic marker can be seen where the master fault plays an important role in the change in thickness between the up-dip and down-dip growth fault. The time variation of this seismic reflector varies from 800 ms in the up-dip growth fault to 2500 ms in the down-dip growth fault in the middle of the big syncline (Figure 2.10).

2.5 CONCLUSIONS

2.5.1 Structure

Regionally two structural systems were identified in the Burgos Basin: (1) The lower compressional system affecting Paleocene and Mesozoic rocks characterized by reverse faulting, and (2) an extensional system characterized by low-angle normal faulting affecting Eocene to Recent rocks.

A decoupling (detachment) level separating both structural systems was identified on the top of the Cretaceous and Neogene interval, where the deepest low-angle normal faults converge.

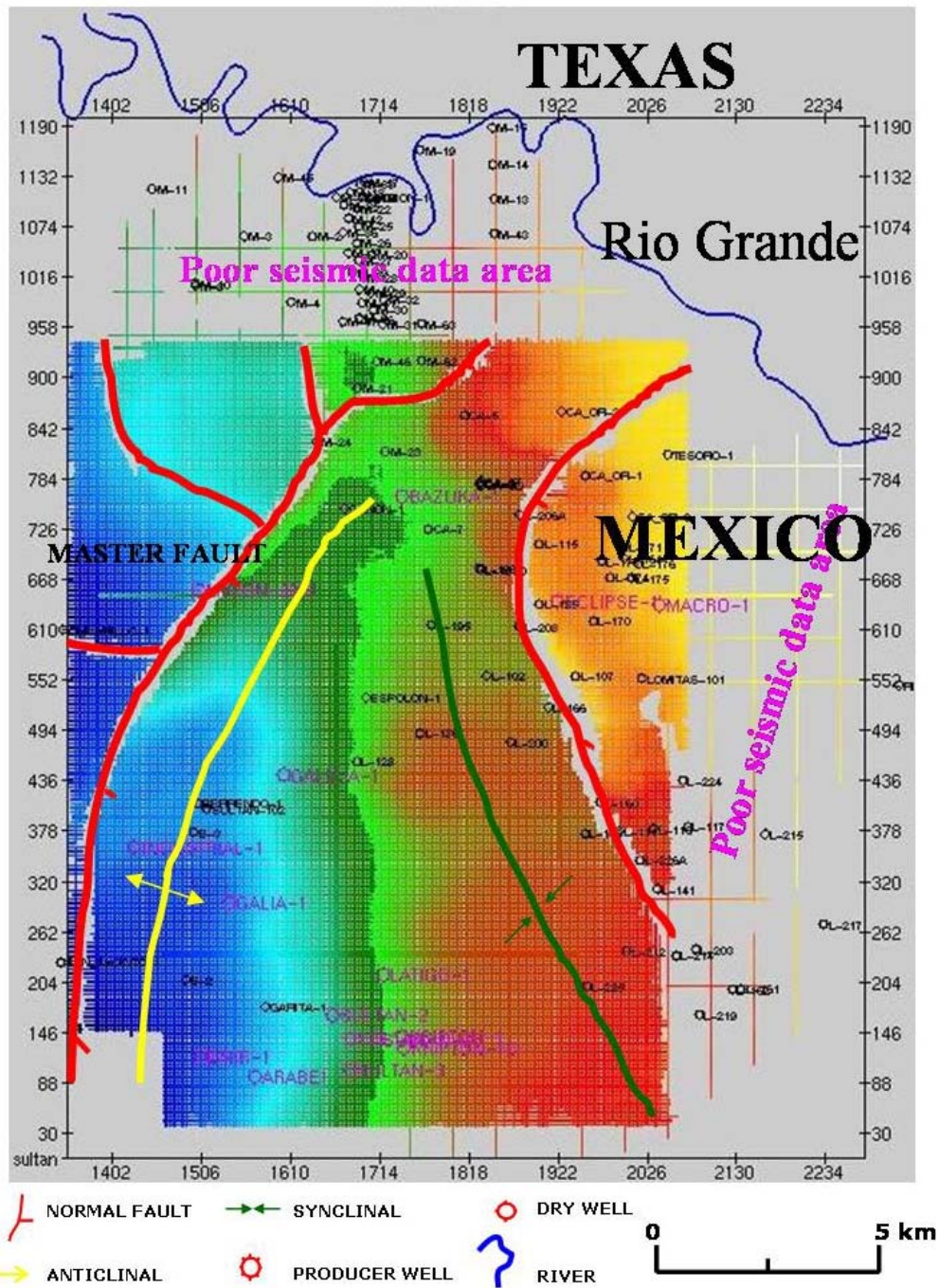


Figure 2.10 Isochron map of the 32.4 ma sequence boundary that corresponds to the top of the Vicksburg Formation. A master growth fault is present in the western portion with a northeast-southwest orientation.

Growth faults are curvilinear in map view and very continuous over distances of several kilometers. The main growth faults bound five structural blocks in which the main reservoirs have been identified.

Vicksburg reservoirs in the Burgos Basin are very productive down-dip, and the reservoirs are placed mostly in rollover anticline traps where fault closures play important roles as seals. The structure of the Vicksburg Formation is complex because of normal faulting sliding on the unstable shales of the Jackson Group.

2.5.2 Stratigraphy

The stratigraphic framework was constructed by the identification and correlation, based on flooding surfaces, of six stratigraphic units, named A to F, within the Vicksburg Formation. These units are constrained to fault-bounded, structurally-defined provinces.

The stratigraphic framework is shared between South Texas and northern México because the major flooding surface marker horizons that define the Vicksburg stratigraphy in the Burgos Basin can be correlated north into Texas. The producing intervals in South Texas fields can be identified and assigned to equivalent genetic stratigraphic intervals of the Burgos Basin. The depositional architectures of delta-flank shoreface and beach ridge facies, as well as delta-mouth-bar facies and distributary-channels facie in the Texas Vicksburg reservoirs, are also comparable to those in the Burgos Basin.

Chapter 3

Petrophysical Analysis

3.1 INTRODUCTION

Log-based petrophysical analysis is very important in any seismic inversion effort. A complete data set of well logs is needed to determine the relationships between petrophysical properties and fluid presence. A petrophysical analysis involves log editing, and log calculation of shale volume, effective porosity, water saturation, hydrocarbon saturation, and elastic properties.

Crossplotting is useful in petrophysical analysis, and modern computational techniques facilitate handling of the data. It is necessary to know the log response functions and their relations to porosity and lithology to make a good interpretation of the crossplotted results. Some well logs are sensitive to porosity, for example, neutron, acoustic, and density. Therefore, all of these logs transform into porosity values. However, equations that convert the log measurements to porosity values involve fluid and matrix parameters that must be known or assumed. In this chapter, the goal is to provide estimations of the volume of shale, water saturation, effective porosity, and derived elastic constants for the principal reservoirs penetrated by key wells that will be used as control points in post-stack and pre-stack seismic inversions.

3.2 WELL LOG DIGITAL DATA BASE

PEMEX Exploración y Producción provided the edited digital log curves for 120 wells. All the wells are vertical, with few exceptions, and are distributed across the 3D survey area. Log-curve suites include caliper, spontaneous potential (SP), gamma ray (GR), resistivity (LLD, ILM, ILD), neutron-porosity (NPHI), density-porosity (DPHI), bulk density (RHOB), and sonic (BHC). In the study area, there are twelve key wells (Figure 3.1) that contain dipole sonic logs (DSI). Detailed log analysis, consisting of estimation of volume of shale, effective porosity, and water saturation at reservoir intervals, was done for these twelve key wells.

3.3 WELL LOG ANALYSIS

V_{shale} was computed for each well using the formula derived from the observed GR curve:

$$V_{shale} = \left[\frac{GR - GR_{clean}}{GR_{shale} - GR_{clean}} \right],$$

where

- V_{shale} is the volume of shale
- GR is the observed log response in the zone of interest
- GR_{clean} is the log response in a shale-free bed, and
- GR_{shale} is the log response in a shale zone.

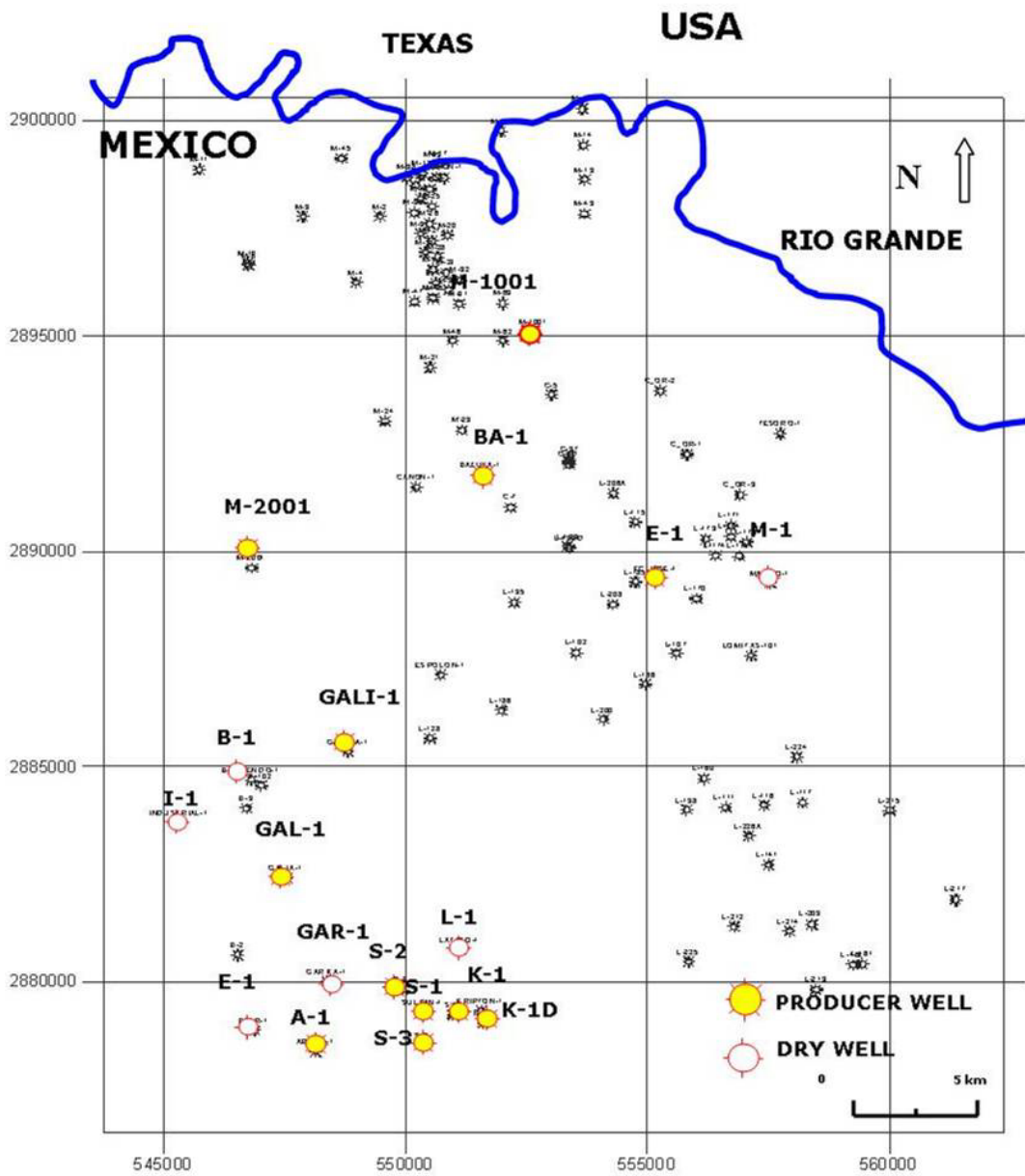


Figure 3.1. Base map highlighting 12 key wells, which have dipole sonic logs, used for the detailed petrophysical analysis in the study area.

A porosity model was validated by comparing the porosity estimation from the neutron-porosity and density-porosity logs corrected for shale and the measured porosity data from cores, by the following equations:

$$\Phi_e = \sqrt{\left(\frac{\Phi_{dc}^2 + \Phi_{nc}^2}{2}\right)}, \quad (\text{formula for gas})$$

where:

- Φ_e is the effective porosity,
- Φ_{dc} is the corrected density-porosity, and
- Φ_{nc} is the corrected neutron-porosity,

and

$$\Phi_{dc} = \Phi_d - (V_{sh} \bullet \Phi_{dsh}),$$

$$\Phi_{nc} = \Phi_n - (V_{sh} \bullet \Phi_{nsh}),$$

where

- Φ_d is the density porosity,
- Φ_{dsh} is the density porosity of shale,
- Φ_n is the neutron porosity, and
- Φ_{nsh} is the neutron porosity of shale.

Water saturation was computed using a modified Simandoux equation (Asquith, 1982),

$$S_w^e = \frac{C \cdot R_w}{\Phi_e^2} \left[\sqrt{\frac{5 \cdot \Phi_e^2}{R_w \cdot R_t} + \left(\frac{V_{sh}}{R_{sh}} \right)^2} - \frac{V_{sh}}{R_{sh}} \right],$$

where

S_w^e is the effective water saturation (clay corrected),

C is a constant normally taken to be 0.40 for sandstones and 0.45 for carbonates,

R_w is the electrical resistivity of the connate water,

Φ_e is the effective (clay corrected) porosity,

R_t is the measured deep resistivity (corrected for invasion and shoulder effects),

V_{sh} is the estimated volume of shale, and

R_{sh} is the resistivity measured in an adjacent shale.

In Figure 3.2, four tracks containing gamma ray, volume of shale, effective porosity, and water saturation are plotted. The red zone corresponds to the gas reservoir interval in the S-1 well; the red point in the effective porosity track is the measured data from core and indicates a good match between estimated data from logs and the measured data from the laboratory.

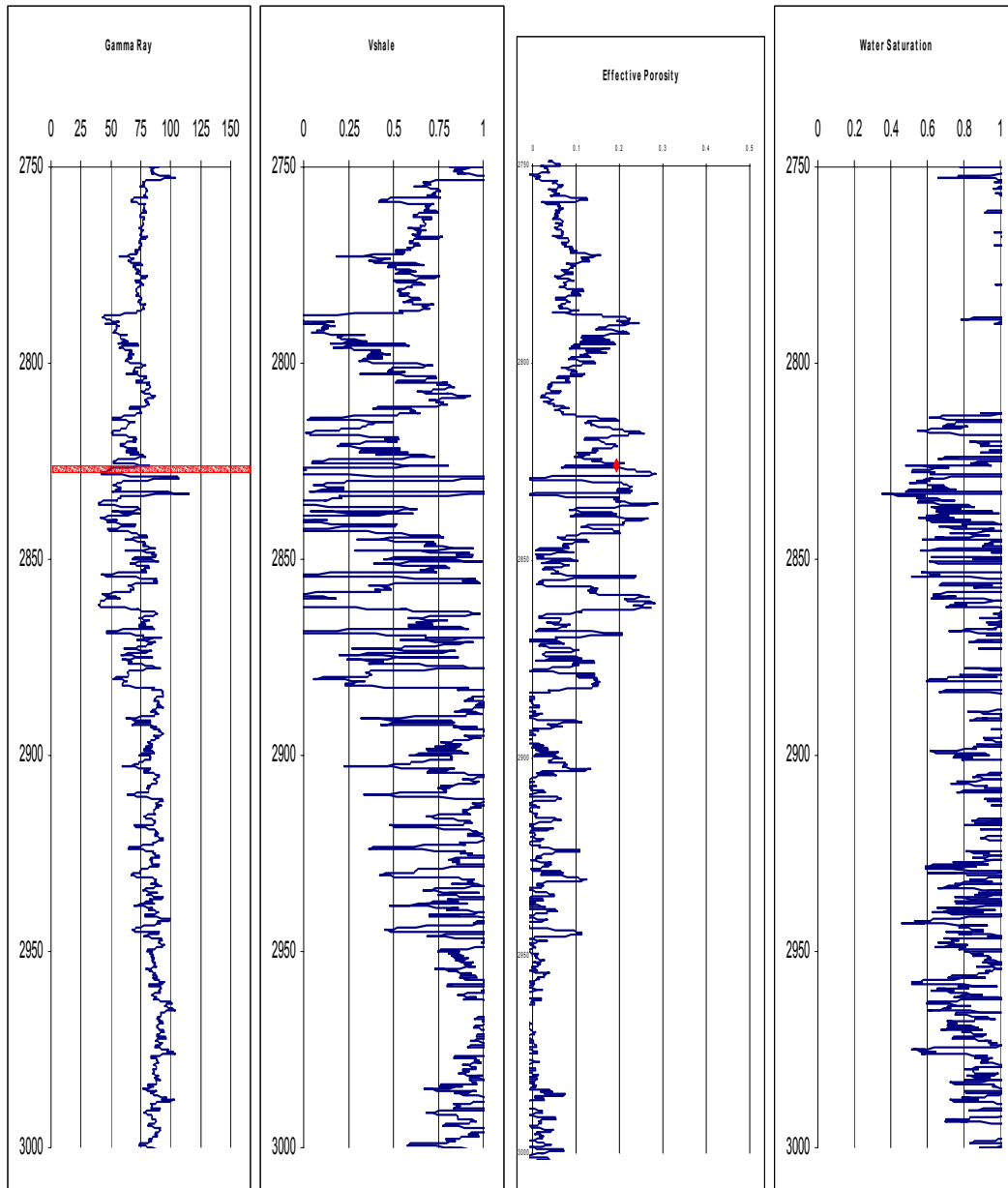


Figure 3.2 Composite log tracks from the S-1 well, showing the gamma ray and computed curves; from left to right: gamma ray, volume of shale, effective porosity, and water saturation. The red point on the effective porosity curve is a data measurement from well core.

3.4 ELASTIC CONSTANTS

Elastic behavior deals with deformations that vanish entirely upon removal of the stresses that cause them. The passage of a low-amplitude seismic wave through Earth media is an example of elastic behavior. For small deformations, Hooke's law holds, and strain is proportional to stress. The stress-strain properties of isotropic materials that obey Hooke's law are specified by elastic moduli. The key moduli include the following:

- **Bulk modulus** k is the stress and strain ratio under simple hydrostatic pressure.

$$k = \frac{\Delta P}{(\Delta V / V)},$$

where

ΔP is the pressure change,

V is the volume,

ΔV is the change in volume and $\Delta V / V$ is called dilatation.

- **Shear modulus, rigidity modulus, or Lamé's rigidity constant** μ is the stress-strain ratio for simple shear.

$$\mu = \frac{(\Delta F / A)}{(\Delta L / L)},$$

where

ΔF is the tangential force,

A is the cross-sectional area,

L is the distance between shear planes, and

ΔL is the shear displacement.

ΔL and L are directed at right angles to each other.

- **Young's modulus or stretch modulus** E , is the stress-strain ratio when an elastic cylinder is pulled or compressed.

$$E = \frac{(\Delta F / A)}{(\Delta L / L)},$$

where

$\Delta F / A$ is the stress,

L is the original length, and

ΔL is the change in length. $1/E$ is called compliance.

- **Lamé's λ constant**

$$\lambda = k - (2\mu/3),$$

where

k is the bulk modulus, and

μ is the rigidity modulus.

- **Poisson's ratio** σ is the ratio of the transverse strain to longitudinal strain when an elastic cylinder of length L is pulled or compressed

$$\sigma = - \frac{(\Delta W / W)}{\Delta L / L},$$

where

ΔW is the width change of the elastic cylinder, and

W is the width of the elastic cylinder.

Poisson's ratio varies from 0 to 0.5. Poisson's ratio value for fluids is 0.5 and 0.25 for Lamé's solids when $\lambda = \mu$.

3.4.1 ELASTIC CONSTANTS AND THEIR RELATIONSHIPS TO ROCK MATRIX AND FLUIDS

Rigidity μ is resistance to shear deformation. μ gives information about the rock matrix.

Incompressibility k is resistance to compression. Lamé's constant λ is an elastic parameter sensitive to fluid content. λ is related to bulk modulus and rigidity by,

$$\lambda = k - (2\mu/3)$$

These physical properties are related to the rock's ability to transmit seismic waves:

$$V_p = \sqrt{\frac{(\lambda + 2\mu)}{\rho}}, \quad V_s = \sqrt{\frac{\mu}{\rho}}, \quad \frac{V_p}{V_s} = \sqrt{\frac{\lambda}{\mu} + 2}$$

$$\sigma = \frac{1/2 \left(\frac{V_p}{V_s} \right)^2 - 1}{\left(\frac{V_p}{V_s} \right)^2 - 1} \quad \frac{V_s}{V_p} = \sqrt{\frac{(0.5 - \sigma)}{1 - \sigma}}$$

where

V_p = is the compressional wave velocity,

V_s = is the shear wave velocity,

σ = is the Poisson's ratio,

λ = is the Lamé's constant,

μ = is the shear modulus or rigidity, and

ρ = is the bulk density.

The shear modulus μ of a rock does not change when the fluid is changed. However, the bulk modulus k unchange when the fluid changes. The bulk modulus of a brine-saturated rock is greater than that for gas-saturated rock because brine is significantly stiffer or less compressible than gas. The effect is that the V_p/V_s ratio of a gas-saturated rock can be substantially lower than the V_p/V_s ratio for the same rock if it was brine-saturated. This change in V_p/V_s ratio can invoke an AVO (amplitude variation with offset) response. Figure 3.3 shows an example of the computed elastic rock properties achieved in well K-1.

3.5 CROSSPLOTING

In this research, graphs were obtained plotting P_velocity (V_p), shear velocity (V_s), V_p/V_s ratio, Poisson's ratio, $\lambda \cdot \rho$, $\mu \cdot \rho$, and λ/μ versus porosity-density, volume of shale, and water saturation computed at specific intervals to define characteristics and ranges of shales and sands in gas reservoirs.

In Figure 3.4A-I a P_impedance versus density crossplot at seismic frequency using a 60 Hz. highcut filter and having a gamma ray color bar, the graph shows the lithologic separation based in P_impedance values. It could show three types of lithology based on P_impedance and density values. This graph indicates that sandstones at the reservoir interval have high P_impedance values and shales have low P_impedance values; in Figure 3.4A-II a crossplot shows P_impedance versus density from the same interval but at well frequency. Both

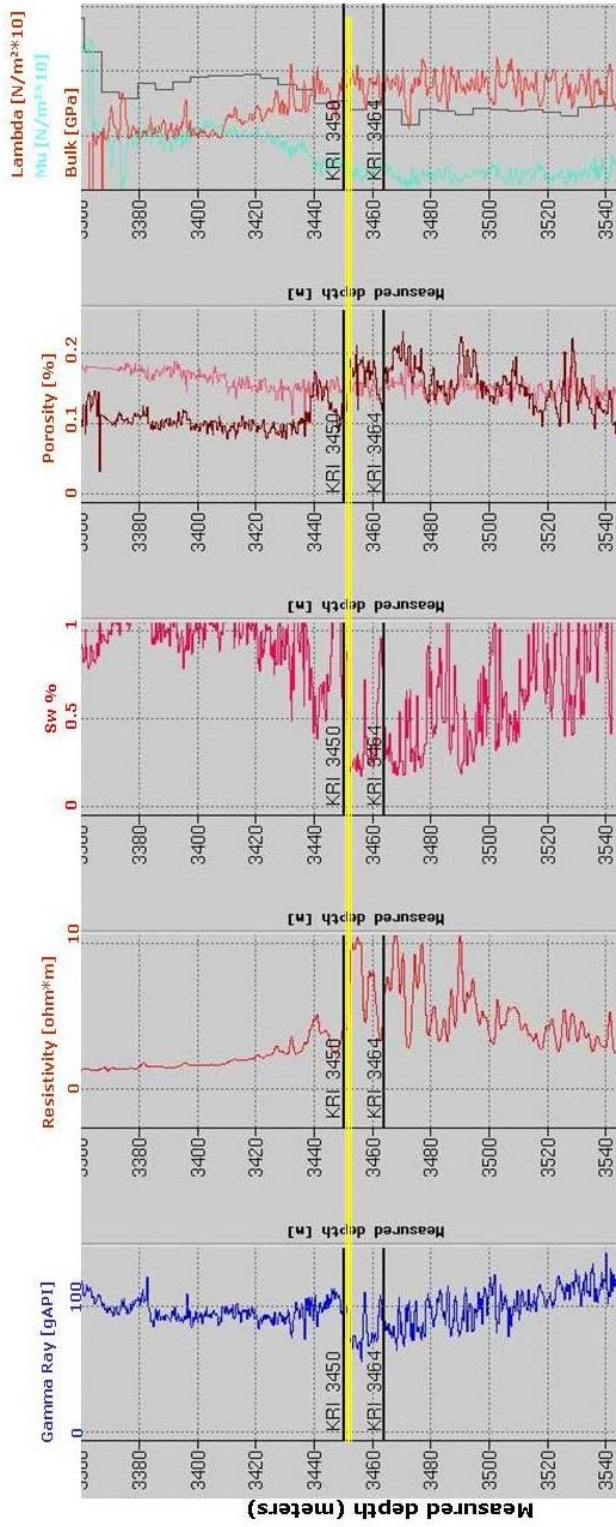
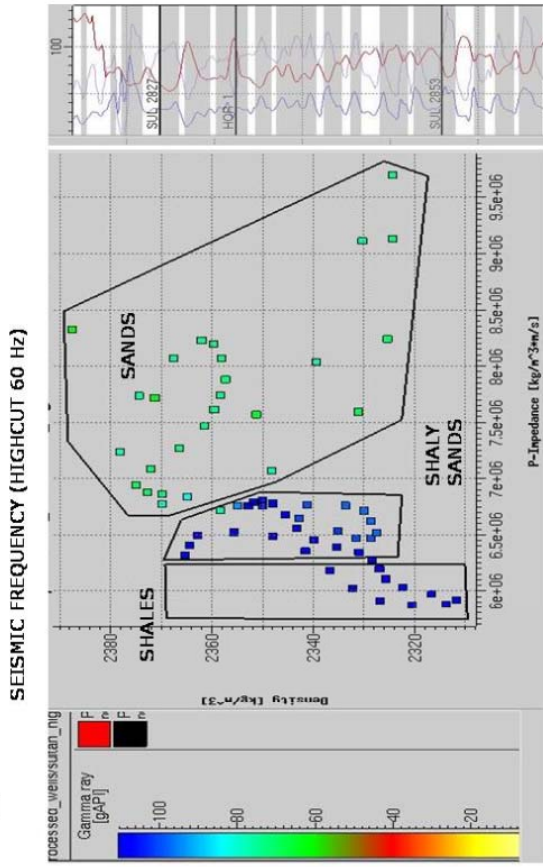


Figure 3.3 Composite log curves showing a suite of measured and computed curves. In the last track to the right, the elastic constants have been computed. Lambda is plotted in red motif. The light blue corresponds to the mu, and the black blocked curve is the bulk modulus k, decreasing at the reservoir interval. The yellow line represents the top upper reservoir in well K-1.

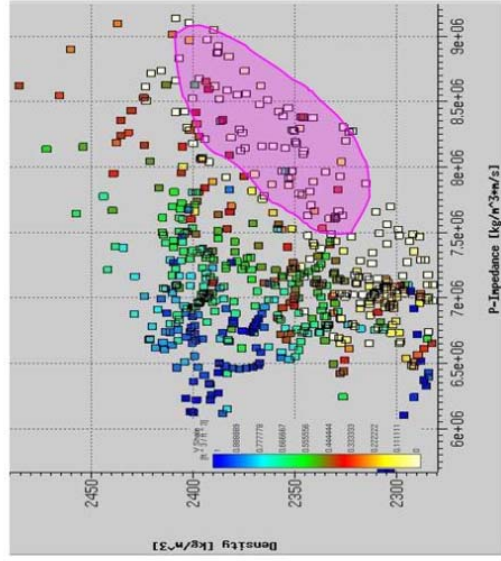
**PETROPHYSICAL ANALYSIS
(RELATIONSHIP BETWEEN ACOUSTIC IMPEDANCE AND
PETROPHYSICAL PROPERTIES IN GAS-BEARING SANDS)**

S_1 WELL

I



II



**** HIGH IMPEDANCE SANDSTONES
ACOUSTIC IMPEDANCE AND DENSITY SENSITIVE TO GAS**

Figure 3.4A Crossplotting at reservoir interval 2827-2847 m in the S-1 well with the color scale representing gamma ray values from 20 to 100 gAPI. (I) P_impedance versus density crossplot at seismic frequency showing lithologic discrimination between sandstone and shales, a shaly sandstone interval could be defined. (II) P_impedance versus density at well frequency showing high P_impedance for sandstones.

graphs show high P_impedance values for sandstones and little discrimination based on density.

In Figure 3.4B there is an example of a set of crossplots calculated for the K-1 well. In this example, the variables V_p , V_s , V_p/V_s , Poisson's ratio, $\lambda \cdot \rho$, $\mu \cdot \rho$, and λ/μ ratio have been plotted versus water saturation in the interval between 3450 and 3460 meters. The color scale, from 50 to 120, corresponds to gamma-ray values (gAPI units) with light colors representing sandstones and dark colors showing shales. In general, the graphs show higher than normal V_p and V_s values for the Vicksburg Formation, because open hole log measurements often are affected by conditions in the wellbore during drilling through the rock formation and must be corrected using charts that include the effect of mud present in the well. Graph A shows a decrease in V_p velocities, from 3500m/s to 2700 m/s, for shales as S_w increases while V_p for sandstones remains between 3200 and 3600 m/s. Panel B shows V_s decreasing from 2200m/s to 1900 m/s for sandstones and from 2000 to 1600 m/s for shales. In plot C, the crossplot shows constant values for sandstones and shales ranging between 1.5 and 1.7 in V_p/V_s ratio as S_w increases except for $S_w > 0.95$. Graph D shows behavior similar to that in graph C where the values for sandstones and shales range between 0.1 and 0.25, an increase in Poisson's ratio for $S_w > 0.95$. Graph E shows ranges between 50 and 200 of $\lambda \cdot \rho$ except $S_w > 0.80$, where an increment in shales is shown. When $\lambda \cdot \rho$ values for shales are higher than values for sandstones, the presence of fluids is indicated. In F $\mu \cdot \rho$ range is limited to values between 200 and 250, indicating a poor quality rock of

K-1 WELL (3450-3465 meters)

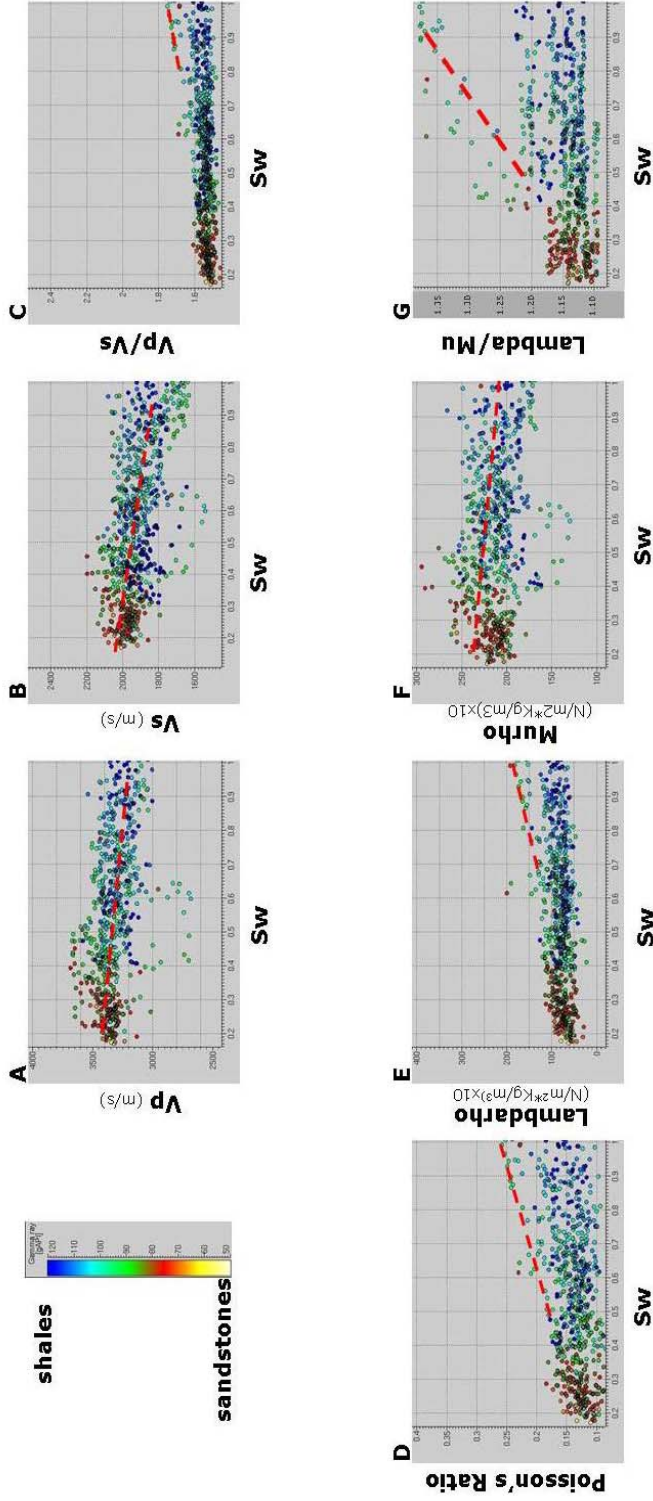


Figure 3.4B Crossplotting at reservoir interval 3450-3460 m in the K-1 well, with the color scale representing gamma-ray values. (A) Vp-Sw graph showing a gradual decreasing in Vp velocities as Sw increases; with sandstones exhibit higher velocities than shales. (B) Vs-Sw crossplot showing Vs decreases as Sw increases. (C) Crossplot of Vp/Vs ratio versus Sw, shows a uniform behavior, except for Sw > 0.95. At high Sw values there is an increment in Vp/Vs ratio for shales. (D) Poisson's ratio-Sw crossplot shows an increment at high values of water saturation, this graph is essentially the same as graph C. (E) The graph of lambda*rho-Sw shows an increment for shales when Sw > 0.8. (F) mu*rho-Sw graph shows constant values for sandstones and decreasing for shales. (G) lambda/mu-Sw crossplot presents a constant behavior for sandstones; for shales an increment is displayed starting at Sw > 0.4.

this interval; sandstones values stay almost constant and decrease in μ^*rho values for shales can be seen as S_w increases. In the final plot G, a λ/mu ratio – S_w graph shows values for sandstones ranging between 1.1 and 1.17, while shales show incremental values from 1.20 to 1.35 for $S_w > 0.5$.

In Figure 3.4C sets of crossplots from the interval between 2827 m and 2847 m calculated for the S-1 well are shown. The variables V_p , V_s , V_p/V_s , Poisson's ratio, λ^*rho , μ^*rho , and λ/mu ratio have been plotted versus water saturation with the color scale, from 50 to 100 gAPI. This corresponds to gamma-ray values (gAPI units) light colors represent sandstones and dark colors show shales. Graph A shows a decrease in V_p velocities, from 3050 m/s to 2950 m/s, for sandstones for values of S_w from 0.4 to 0.7, increasing V_p from 3000 m/s to 4350 m/s for $S_w > 0.7$; V_p for shales ranges from 2800 m/s to 3000 m/s. Panel B shows V_s decreasing from 2000 m/s to 1900 m/s for sandstones and from 1700 m/s to 1500 m/s for shales. In plot C, the crossplot shows increment in values for sandstones ranging between 1.6 and 1.8 in V_p/V_s ratio as S_w increases except for $S_w > 0.8$ where the V_p/V_s ratio increases substantially from 1.6 to 2.6. Graph D shows an incremental behavior from 0.2 to 0.35 for sandstones; shales range from 0.25 to 0.38 as S_w increases. Graph E shows values for sandstones between 150 and 200 of λ^*rho except $S_w > 0.70$, where an increment in sandstones is shown; shale behavior is constant at values ranging between 150 and 200. In general this graph shows higher values for shales than sandstones. In F, μ^*rho range is limited to almost constant values of 180 for sandstones, indicating a good quality rock of this interval; sandstones

S-1 WELL (2827-2847 meters)

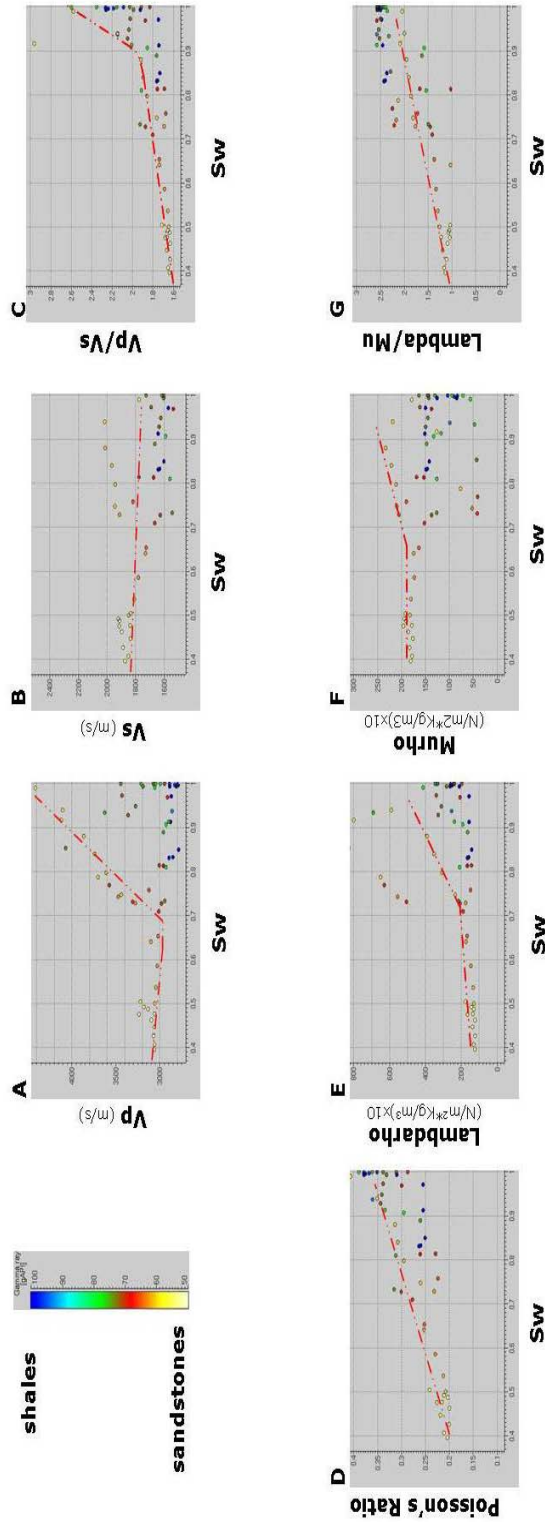


Figure 3.4C Crossplotting at reservoir interval 2827-2847 m in the S-1 well, with the color scale representing gamma-ray values from 50 to 100 gAPI. (A) Vp-Sw graph showing a gradual decrease in Vp velocities as Sw increases; with sandstones exhibit higher velocities than shales; Vp is increased for sandstones substantially for Sw > 0.7, Vp in shales varies from 2800 m/s to 3000 m/s (B) Vs-Sw crossplot showing Vs and Vp decreases as Sw increases. (C) Crossplot of Vp/Vs ratio versus Sw, shows a decreasing uniform behavior, except for Sw > 0.95. At high Sw values there is an increment in Vp/Vs ratio for shales. (D) Poisson's ratio-Sw crossplot shows a constant increment starting at 0.4 of water saturation values. (E) The graph of lambda*rho-Sw shows a strong increment for sandstones when Sw > 0.7, shales stay between values ranging between 150 and 200. (F) mu*rho-Sw graph shows constant values for sandstones and staying constant values for shales at high Sw values. Sandstone values are highest at Sw > 0.75. (G) lambda/mu ratio-Sw crossplot presents a constant increment behavior for sandstones; shales present higher values than do sandstones.

values increase for $S_w > 0.7$ in $\mu \cdot \rho$ values. Shales range between 50 and 150. In the final plot G, a λ/μ ratio – S_w graph shows an increment for sandstones from 1.1 to 2 as S_w increases, while shales show values from 1.5 to 2.5; in general, shales show higher values than do sandstones in this interval.

3.6 BIOT-GASSMANN SENSITIVITY ANALYSIS

Biot (1956a,b) described the theory of propagation of elastic waves in fluid-saturated porous solids for low and high frequency ranges. Because there were unknown coefficients involved, his equations were difficult to measure. Geerstma (1961) found a solution by letting the frequency-dependent Biot equation reduce to what is called the zero-frequency approximation. The Gassmann equation (Gassmann, 1951a,b), is useful for predicting velocities in gas and oil-saturated reservoirs, although it fails to consider some factors that contribute to seismic character like amplitude.

The Gassmann equation is given by:

$$V_p^2 = \frac{\left[\left(K_b + \left(\frac{4}{3} \mu_b \right) \right) + \left(1 - \left(\frac{K_b}{K_s} \right) \right)^2 \right] \cdot (1/\rho_b)}{\left[\left(1 - \Phi - \left(\frac{K_b}{K_s} \right) \right) \cdot (1/K_s) + (\Phi/K_f) \right]} \cdot (1/\rho_b)$$

$$V_s^2 = \frac{\mu_b}{\rho} ,$$

where

V_p is the compressional wave velocity,

V_s is the shear wave velocity,
 K is the bulk modulus,
 μ is the shear modulus or rigidity,
 Φ is the porosity,
 ρ is the density, and

the meaning of the subscripts,

b is related to dry rock,
 f is related to pore fluid, and
 s is related to solid material.

This simplified form of the Biot equation is useful at seismic frequencies. It is used to solve for the bulk modulus of the drained rock frame K_b , given by an initial P_velocity, water saturation, porosity, and assumed bulk moduli dry Poisson's ratio σ , and densities and bulk moduli of the water.

The objective here is to calculate the trend of the velocity in the reservoir or area of interest by substituting these values for the porosity and water saturation. The data required for modeling are the S-wave and P-wave velocities, V_s and V_p respectively.

Shear modulus remains the same if only the water saturation is changed, but bulk modulus will change with water saturation at fixed porosity. If the porosity is changed, then the dry rock exhibits new elastic parameters that are updated using a variation of Pickett's equation (Pickett, 1963) for estimating the

dry rock moduli. Poisson's ratio of the dry rock is also necessary although not critical, and 0.12 is assumed.

These calculations were applied in the S-1 and K-1 wells, which have laboratory estimates for bulk and shear modulus and porosity in addition to P_wave and S_wave logs. Figure 3.5 shows the results of S-1 well from laboratory petrophysical analysis from core; the core was extracted from an interval that includes the rock reservoir.

Figure 3.6A and 3.6B shows the results of velocity modeling following fluid and porosity substitution at the reservoir interval given the values of V_p , V_s and ϕ extracted from the laboratory tests and then compared with the crossplots obtained from well logs at the same intervals.

In Figure 3.6A the crossplots showing the gas effect response in a clean and high-porosity sandstone from S-1 well is presented; according to the crossplots, the velocity modeling indicates a strong variation of V_p and V_p/V_s ratio at $S_w > 0.95$.

In Figure 3.6B the gas effect is not so dramatic due to the lithologic characteristic of the sandstone from the K-1 well that consists of shaly sandstone with porosity 12.4% and 0.2 of volume of shale.

The principal difference between both modeling analyses is that S-1 sandstone comes from a more proximal environment than K-1, which has high shale content because of having come from a more distal environment.



S-1 Well
 Plug sample at 2825.88 m depth
 Brine Saturated 26,000 ppm
 Confining pressure 2800 psia

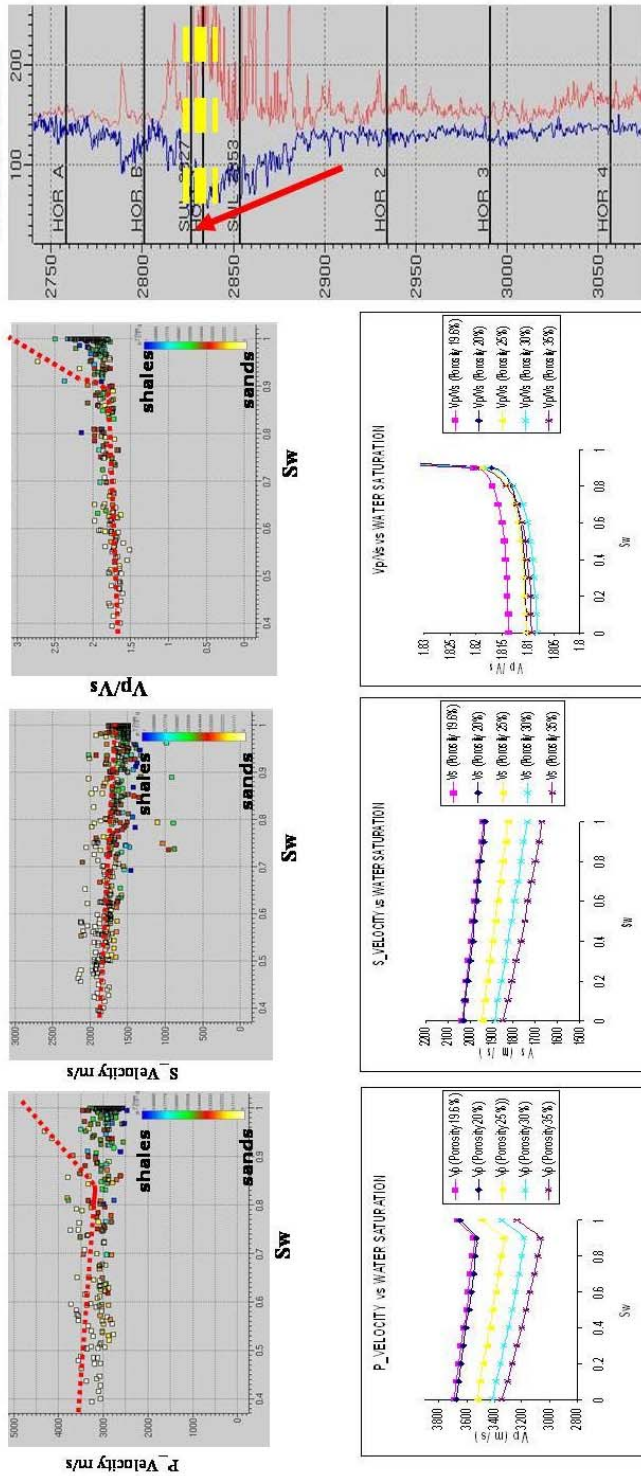
$V_p = 3787.2$ m/s
 $V_s = 2079.5$ m/s
 $K = 28.85$ GPa
 $E = 37.36$ GPa
 $\mu = 14.55$ GPa
 $\sigma = 0.284$

$\Phi = 19.6$ %
 $\rho = 2.32$ gr/cc
 $k = 14.44$ md

Figure 3.5 Core petrophysical analyses at reservoir interval in S-1 well. Laboratory measurements include bulk, Young, and shear moduli.

FLUID SENSITIVITY ANALYSIS

S_1 WELL

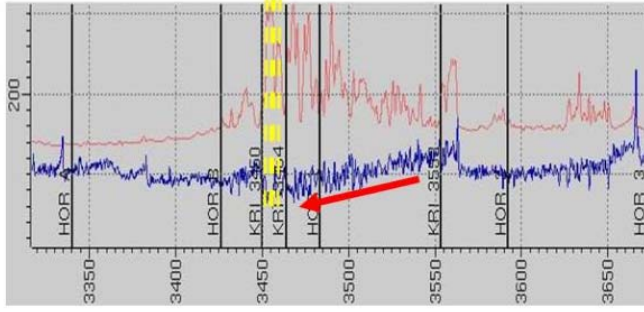


POROSITY = 19.6 %
Vshale = 0.01
Bed thickness (2827-2847) = 20 meters

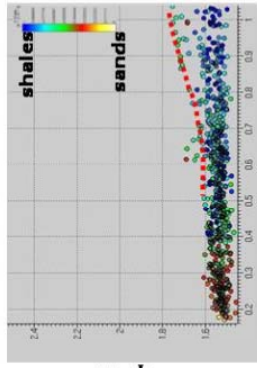
Figure 3.6A Biot-Gassmann sensitivity analysis in S-1 well at the gas reservoir interval between 2827 and 2847 meters. The upper crossplots are the measured data from logs, and the lower graphs show the velocity modeling when Sw is changed. Variation of P-velocity and Vp/Vs ratio due to gas-saturated sand can be seen.

FLUID SENSITIVITY ANALYSIS K_1 WELL

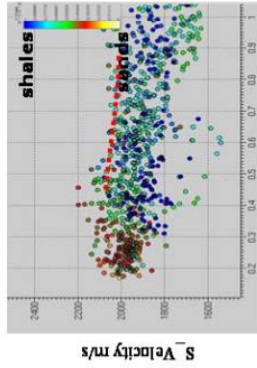
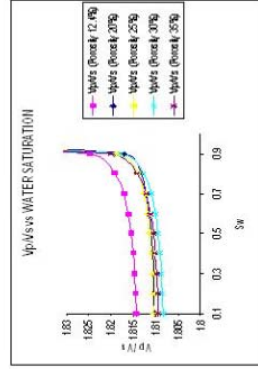
**GAMMA RAY
RESISTIVITY**



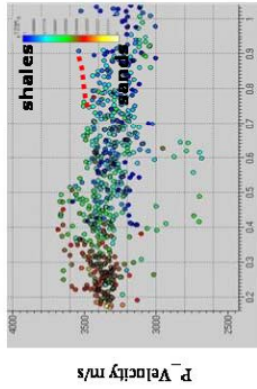
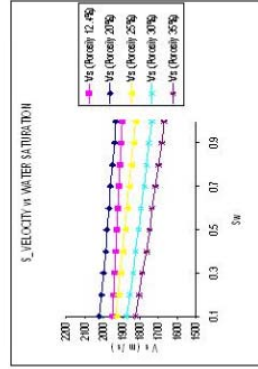
POROSITY = 12.4 %
Vshale = 0.20
Bed Thickness = 10 meters
3450-3460



Sw



Sw



Sw

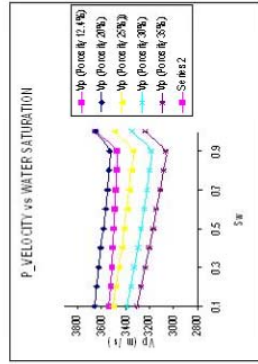


Figure 3.6B Biot-Gassmann sensitivity analysis in K-1 well at the gas reservoir interval between 3450 and 3460 meters. The upper crossplots are the measured data from logs, and the lower graphs show the velocity modeling when Sw is changed. Variation of P-velocity and Vp/Vs ratio due to gas effect from saturated sand is displayed.

3.7 FLUID AND LITHOLOGY DISCRIMINATION

Mud filtrate invasion can occur in many types of permeable hydrocarbon-bearing formations, and it causes sonic logs that show low values (higher P or S velocities) and high density log values. Mud filtrate invasion affects shallow investigation tools such sonic and density. Generally the log curves delivered from PEMEX are corrected for environmental effects, but the data used here are not totally corrected, and mud filtrate invasion is present in these logs .

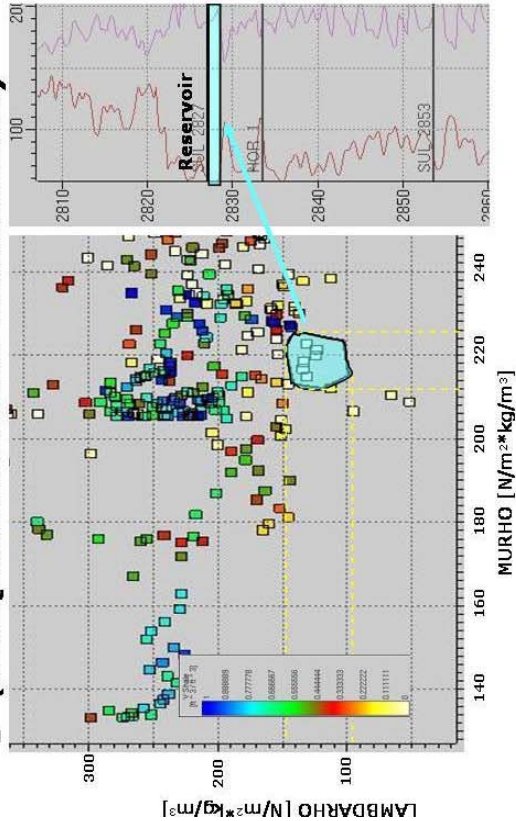
Lamé's parameters, lambda and mu, are useful to discriminate between fluids and rocks. Lambda (λ) is an elastic parameter sensitive to fluid content and is related to bulk modulus and rigidity by $\lambda = k - 2\mu/3$.

Mu (μ) or rigidity is resistance to shear deformation. Mu gives information about the rock matrix. The shear modulus, μ , of a rock does not change when the fluid is changed. The bulk modulus, k , does change significantly when the fluid changes. Elastic properties were computed in key wells to differentiate rocks from fluids. Crossplotting of Lamé's parameters is useful to discriminate lithology or fluids, depending on the rock quality and thickness. Figure 3.7 displays a crossplot of lambda*rho versus mu*rho that illustrates separation of the reservoir zone from the rest of the points in λ - μ domain, which indicates that Lamé's parameters computation can be used for discriminating gas reservoir zones. In particular, the reservoir is characterized by low values of lambda*rho consistent with the presence of gas.

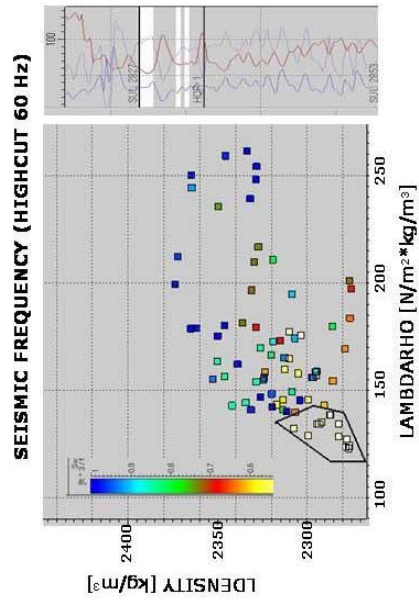
S-1 WELL

PETROPHYSICAL ANALYSIS

I (ROCK QUALITY AND FLUID DISCRIMINATION)



II



** LAMBDA*RHU FLUID DISCRIMINATOR MURHO ROCK QUALITY DISCRIMINATOR

Figure 3.7 (I) Lambda*rho versus mu*rho crossplot displaying the separation of the reservoir zone and identification of sandstone in well log. Knowing the values of elastic properties is a first step to the inversion processes used to extrapolate through a seismic cube. (II) Lambda*rho versus density crossplot at seismic frequency 60 Hz highlight filtered, showing low values of density and lambda*rho for sandstones at reservoir interval. This indicates fluid discrimination.

3.8 CONCLUSIONS

Petrophysical analysis is a fundamental process for this inversion project because the acoustic and elastic properties of rocks were defined.

A well log data base including porosity, density, gamma ray, and sonic curves was necessary for making such an analysis and for establishing the relationship between rocks and fluids. The methodology used here consisted of editing logs and computing of shale volume, effective porosity, water saturation, and elastic properties.

Mud filtrate invasion in sonic and density well logs is present because the environmental effects were not totally corrected for.

Crossplotting was useful for defining the petrophysical properties in reservoir intervals of interest and was helpful for discriminating between fluids and rocks at key wells. As a result of this, high $P_{\text{impedance}}$ sandstones were defined with crossplots and low density linked to low values of $\lambda \cdot \rho$ were used to detect fluid at seismic frequency.

Lamé's petrophysical parameters, $\lambda \cdot \rho$ and $\mu \cdot \rho$, were analyzed as tools for fluid and lithology discrimination. Clean and good-porosity sandstone from S field provided the best way to discriminate between fluid and lithology; shaly sandstone from the K reservoir which has low porosity, does not show a clear gas effect in fluid substitution modeling.

However, the shale effect, the mud filtrate invasion, and the presence of gas are the most important issues in this petrophysical analysis, and these effects are present in all data.

Chapter 4

Stratigraphic Analysis of Reflectivity Data I: Enhancing Lateral and Vertical Resolution with Constrained Sparse Spike Inversion

4.1 INTRODUCTION

Constrained sparse spike inversion from Jason's software (CSSI®), represents one way to reduce wavelet tuning effects and to remove the effects of wavelet side lobes. CSSI uses seismic traces to estimate reflectivity with some minimum number of reflection coefficients via optimization methods. In the CSSI algorithm, the results are driven by seismic data, with trends and constraints derived from well data and from the Earth model defined by the seismic horizons.

The trends and constraints are useful for reducing non-uniqueness in the inversion process. Because the seismic data do not have low-frequency information, the inversion provides the low-frequency component from the well log data, which is subsequently merged with the band-limited data from the seismic reflections to produce a total acoustic impedance volume.

Reflectivity data derived from seismic inversion can be used to define stratigraphic sequences from enhanced lateral continuity and vertical resolution of seismic data. Using case study from a new gas field in a mature basin, I will show how this approach leads to improvements in delineation of spatial distribution and lateral continuity of reservoirs. Using a sequence stratigraphic framework to extract reflectivity values, this chapter shows how sand bodies can be delineated.

Reflectivity modeling is helpful for delineating and characterizing reservoirs that cannot be defined using conventional seismic data. Resolution of reflectivity data derived from seismic inversion increases when the wavelet effect is removed and reflector continuity is improved. The integration of seismic data with borehole data containing low-frequency information was very important in this study as the data set includes good-quality P-wave and S-wave sonic and density well logs and check-shot surveys.

Use of reflectivity data provides the following advantages:

1. Lateral and vertical resolution is increased.
2. Tuning effect is reduced.
3. Reflectivity is an interface property, whereas acoustic impedance is a bulk layer property.
4. Boundaries of reservoirs can be accurately defined, thereby improving the characterization of gas reservoirs.
5. Stratigraphic analysis of reflectivity data can be developed between reservoir interfaces by retracing seismic horizons, allowing the refinement of the sedimentary model.
6. Sequence boundaries can be accurately defined by reducing the tuning effect.
7. Results from the inversion of reflectivity data can be calibrated with wells.

In this chapter, a methodology is proposed to use reflectivity data from seismic inversion to enhance lateral and vertical seismic resolution. It is shown through the descriptions of a case study how reflectivity is useful for delineating reservoir boundaries. Reflectivity analysis was applied in an Oligocene wave-

dominated delta depositional environment. In wave-dominated deltas, the principal framework facies consists of amalgamated beach-ridge sands deposited along the front and margins of the delta (Han, 1981; Han and Scott, 1981), and imparts a first-order, sedimentary strike orientation of the delta framework. Dip-oriented distributary channel-fill facies sand bodies constitute a secondary framework (Galloway and Hobday, 1983). Prodelta facies are not thick because the intensity of wave reworking results in widespread dispersal of suspended sediments. This analysis helped define the lateral continuity of strike-oriented sand bodies deposited by wave action reworking sediments supplied from ancient Rio Grande channels eastward into the Cenozoic Burgos Basin in northern México. Seismic amplitude attribute maps were used to define the lateral extent of sand bodies and, therefore, the limits of reservoirs. This technique can be applied in other reservoir characterization and delineation studies.

4.2 BACKGROUND

Results presented here describe a study carried out in a new gas field in the Burgos Basin in northern México (Figure 4.1). The objective of this study was to delineate reservoir boundaries by reflectivity analysis of stratigraphic sequences. The field, a north-south trending anticline, was discovered in 2001. Gas production is from the Vicksburg Formation, in Oligocene rocks deposited in a wave-dominated depositional system. A P-wave seismic data volume was acquired in 1999 and reprocessed in 2001.

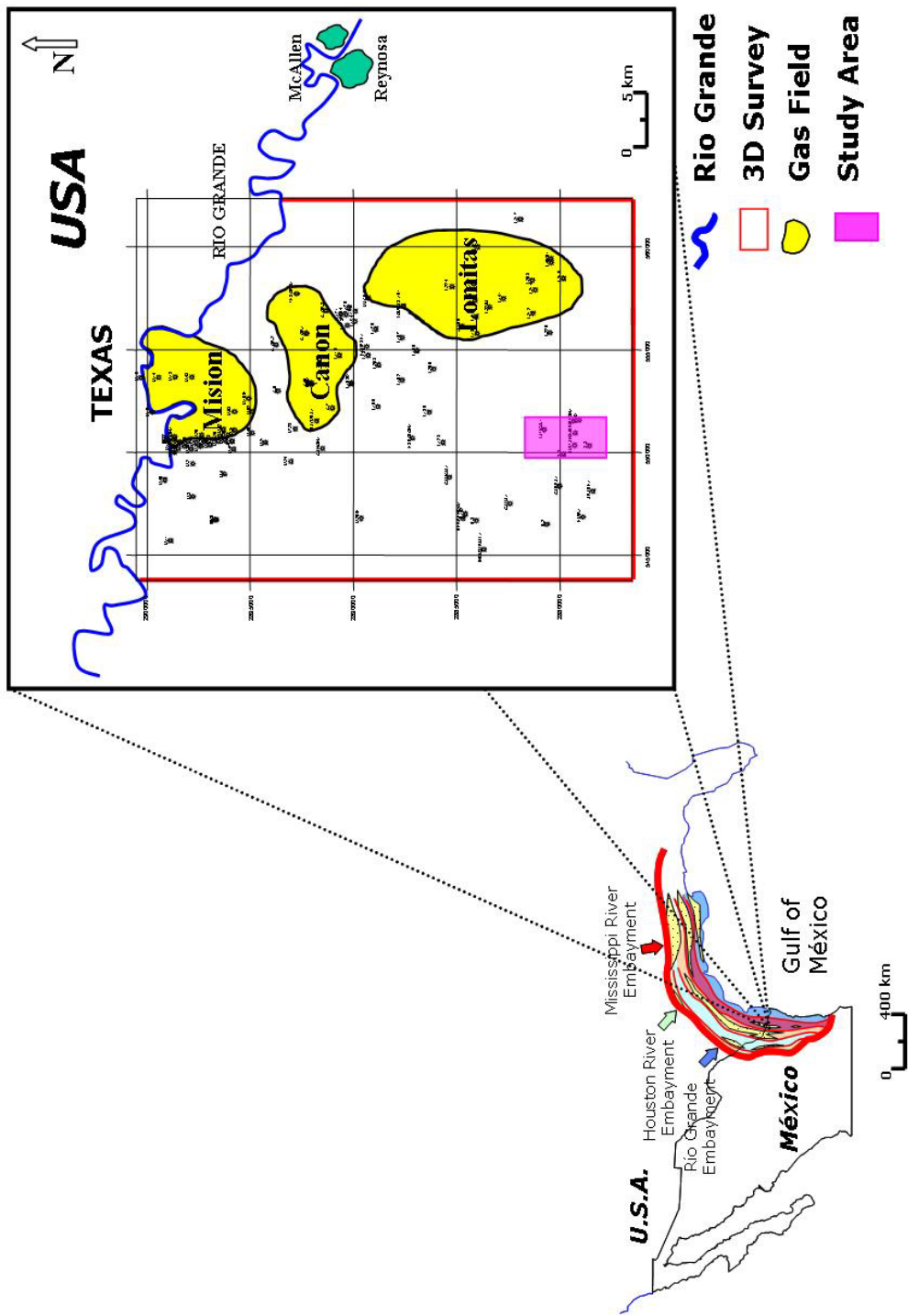


Figure 4.1 Location map showing the position of the study area in the Burgos Basin, northern México.

4.3 METHODOLOGY

This study involved eight main steps:

1. Structural analysis that identifies the main structural components in the study area and constructs a fault framework.
2. Construction of a sequence stratigraphic model and sequence boundary surfaces using seismic data and well logs.
3. Sonic log interpolation to form a low-frequency velocity model.
4. Wavelet extraction from the seismic data at well positions.
5. Seismic inversion of the 3D volume to produce the reflectivity model.
6. Interpretation of seismic horizons onto the reflectivity volume.
7. Amplitude attribute extraction for the seismic volume and reflectivity data.
8. Interpretation and comparison of attribute maps extracted from the seismic and reflectivity data.

4.3.1 Structural Analysis

The structural style of growth faulting in the Vicksburg Formation is due to a combination of rapid sedimentation and flowage of mobile shale from the underlying Jackson Group, which resulted in major low-angle growth faults. These growth faults influenced the pattern of contemporaneous sandstone distribution and the continuity across upthrown and downthrown blocks (Han, 1981; Han and Scott, 1981). In the study area, Vicksburg rock thicknesses are expanded and affected by intense normal faulting with the main growth fault

oriented nearly north-south and following a curvilinear path (Figure 4.2). The Vicksburg Formation is characterized by several overpressured gas fields.

These fields occur in deep-buried sandstone facies at a depth of more than 3.5 km and are associated with stacked deltaic systems affected by syn-sedimentary growth faults.

4.3.2 Stratigraphic Units

The broad stratigraphic model was built with six flooding surfaces identified in well logs and on the seismic data. These surfaces were picked using all of the available logs in each well and exhibited a good correlation. Sedimentary sequences identified in all wells in this study were divided into packages in which six stratigraphic units were defined. In this chapter, unit D is the main goal of study, because it contains the main reservoir in the S gas field. Stratigraphic unit D was subdivided into five seismic markers in the original seismic volume to provide a detailed correlation throughout the reservoirs.

4.3.3 Earth Model

In this part of this project, a 3D property model based on wells and stratigraphic description was built for the sequence stratigraphy framework. The purpose of building a subsurface model for the sparse spike inversion methodology is to generate a set of continuous horizons that can be used to define constraints along the wells and to build a cube of interpolated impedance logs.

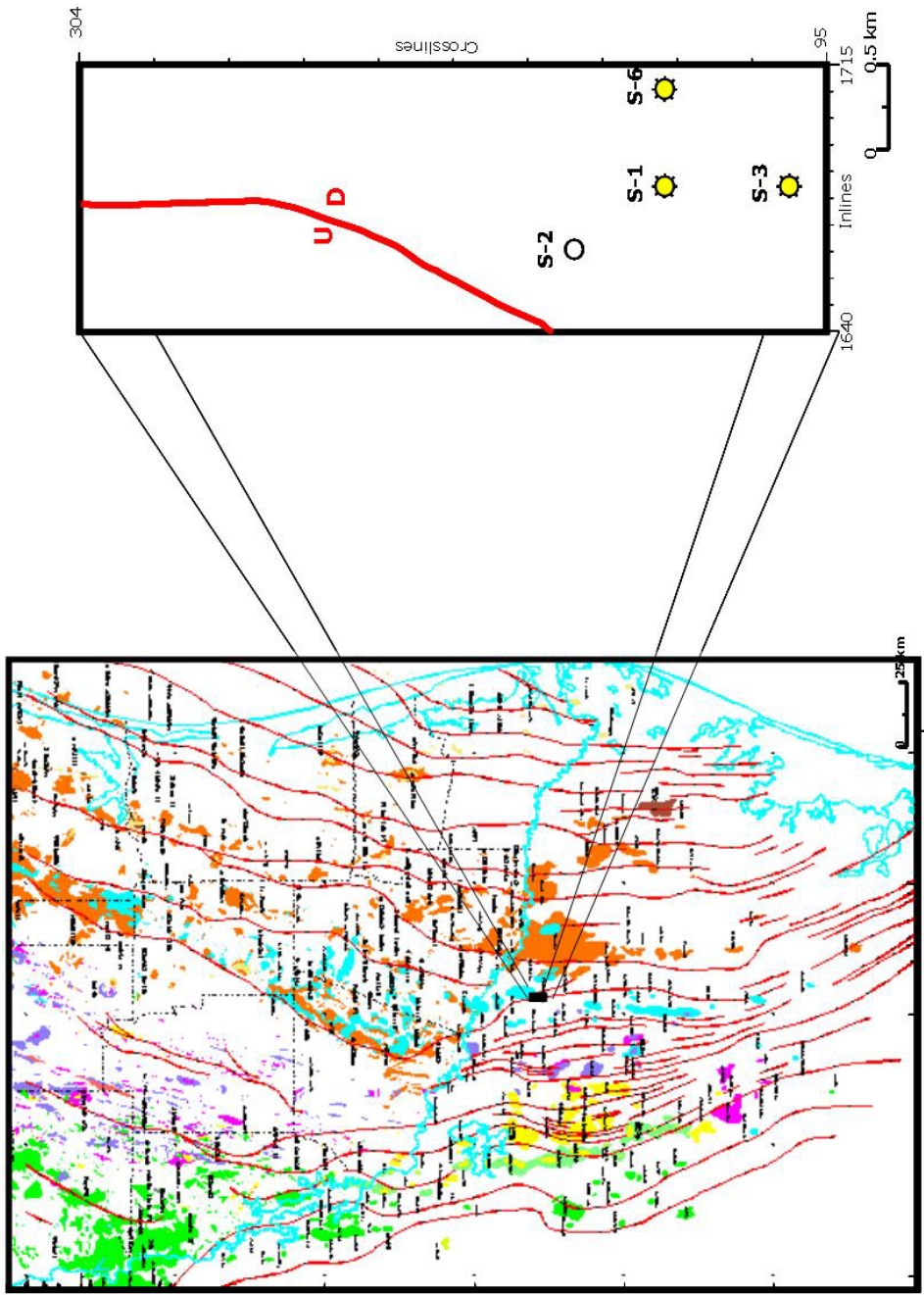


Figure 4.2 Structural regional framework in the study area, shadowed by the black rectangle. The reservoirs are down-dip of the growth fault in the S gas field. The map on the right shows the position of the growth fault and the control wells used in the post-stack inversion processes.

The earth model, or solid model, was built by interpolation of the well logs along continuous strata to form a low-frequency model that is conformable to the top and base of the interpreted interval (Figure 4.3). These interpolated sonic log data are integrated with inverted impedances to provide a high-resolution result consistent with the log data at well ties.

4.3.4 Seismic bandwidth and wavelet extraction

Seismic bandwidth

In any seismic inversion project, it is necessary to know the characteristics of seismic data in terms of bandwidth, noise, velocity anomalies, migration artifacts, multiples, diffractions, and amplitude-versus-offset behavior because all of these effects will be included in the final product. A frequency spectrum extracted from a time window between 1800 and 2500 ms of traces in a seismic line is shown in Figure 4.4. The data were analyzed in the time-frequency spectrum to determine the bandwidth of the seismic traces. This figure shows that the seismic data do not contain sufficient inversion information in the low-frequency interval (0 to 10 Hz). Thus, the low-frequency character must be supplied from well log data inside the seismic image space.

Wavelet extraction

Seismic wavelet extraction is very important in an inversion project. The characteristics of the wavelet make a strong imprint on seismic amplitude variation. To estimate the wavelet from well control, the fundamental inputs are

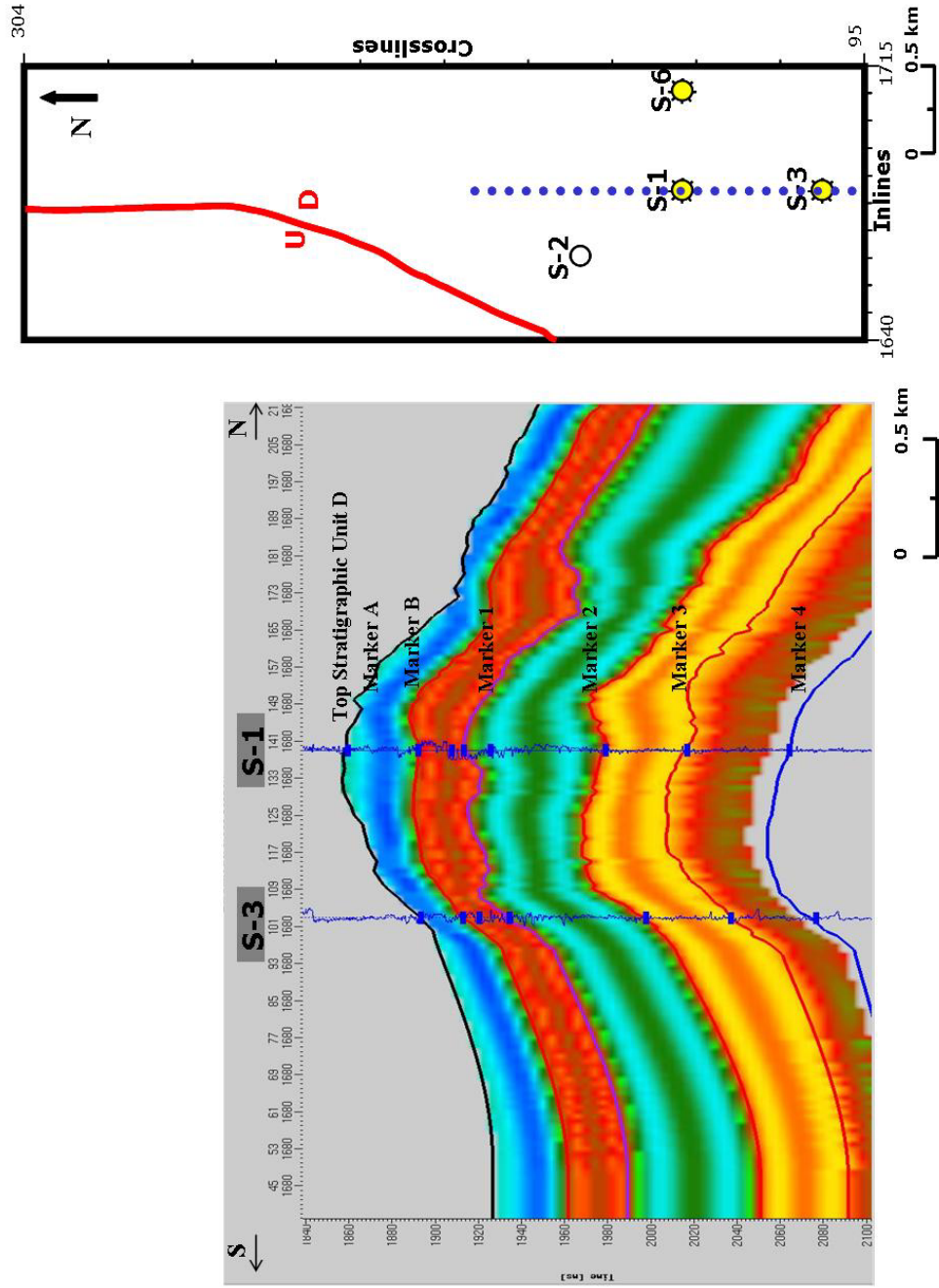


Figure 4.3 Solid model illustrating the sequence boundary D and the subdivision into six micro-layers within the sequence. This earth model represents the interpolation of the six interpreted seismic horizons throughout the study area.

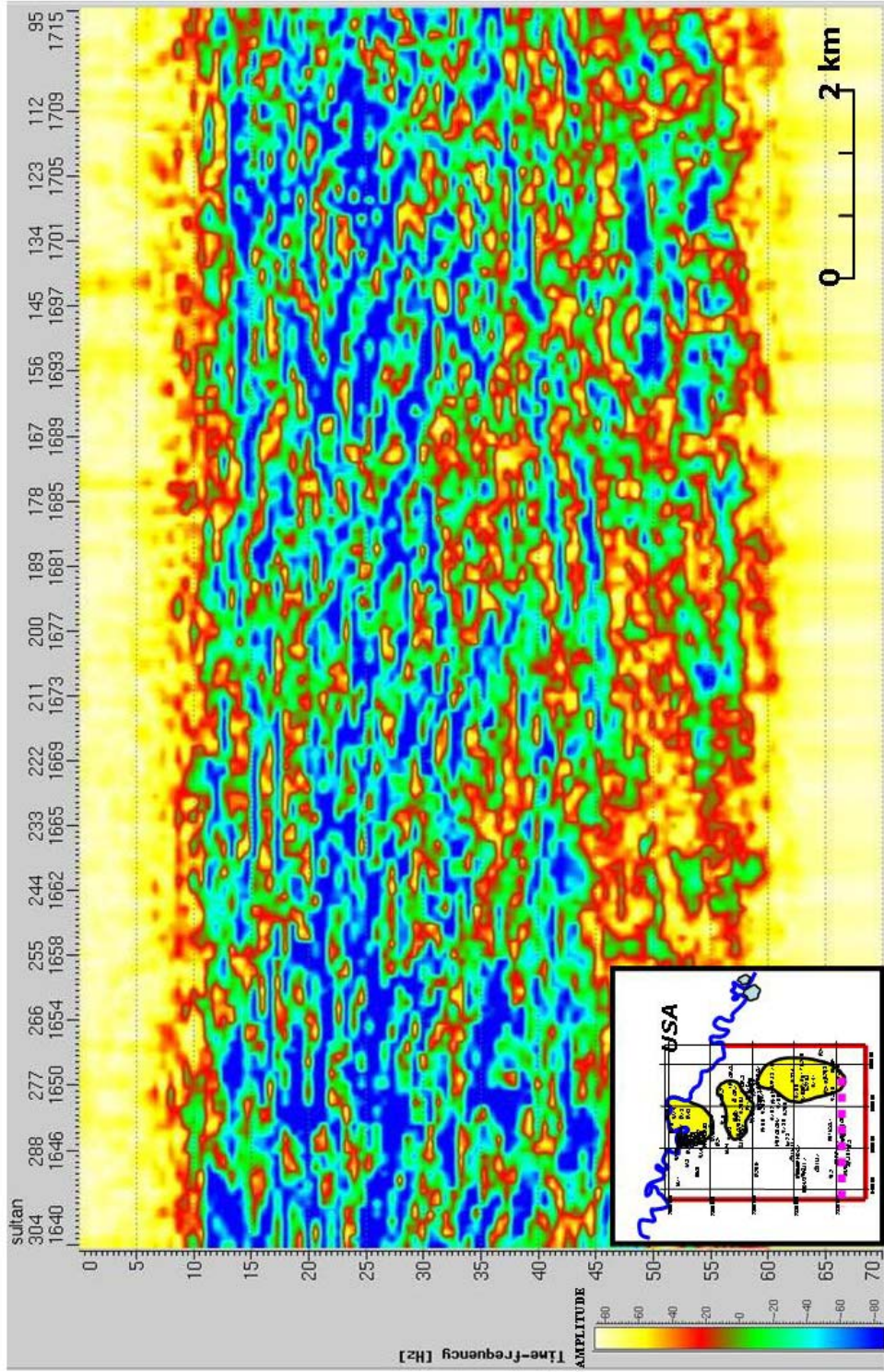


Figure 4.4 Amplitude-frequency character of seismic data extracted in a time window between 2,000 and 2,500 ms. The useful bandwidth is 10-60 Hz.

the seismic traces and the targeted time window. The process is to find a wavelet that produces the best synthetic match to the seismic data.

In this study, a wavelet extraction was performed at control wells and time-depth conversions from checkshots were refined to give an improved synthetic to seismic tie.

A wavelet was extracted at two well locations as follows:

- Check shot corrections were applied to the seismic data adjusting the well data to seismic time.
- A wavelet was estimated from the amplitude spectrum, averaged from ten seismic traces at each well location to generate a zero-phase wavelet.
- Wavelet phase was estimated using a constant-phase spectrum. It was necessary to make an initial bulk shift and stretch and squeeze the time-depth relationship to obtain a good match between seismic and synthetic data.
- A wavelet was estimated using both amplitude and phase spectra. It was necessary again to apply some stretching and squeezing to the time-depth curve.

Once the wavelet was estimated at each of the two wells, an average wavelet was calculated. Figure 4.5 shows the two wavelets estimated at each well location as well as the average wavelet.

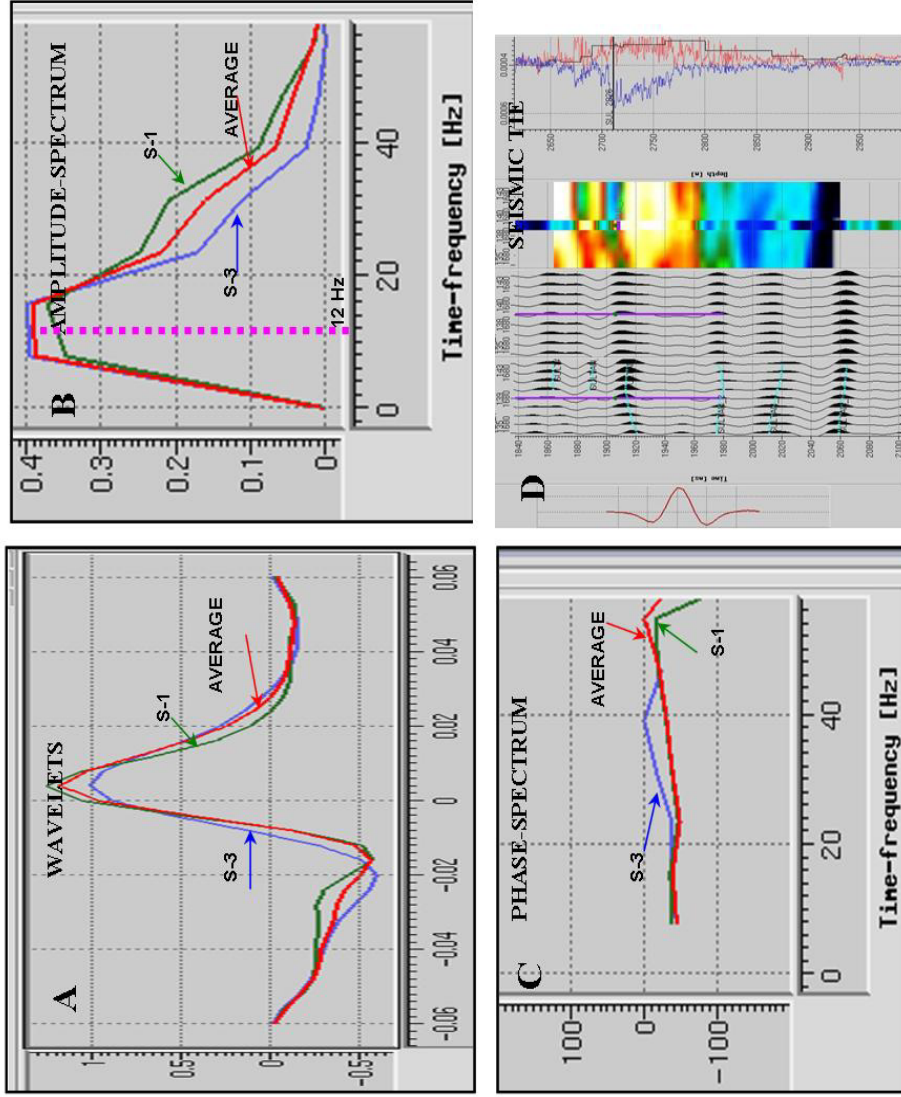


Figure 4.5 Wavelet extractions at two wells on the S field for a time window between 1850 and 2050 ms. (A) Wavelets extracted from wells S-1 and S-3, the average wavelet which in red. (B) Frequency spectrum in which the central frequency is 12 Hz. (C) Phase spectrum for the extracted wavelets. (D) Synthetic seismogram using the average wavelet shows a good match.

4.3.5 Constrained Sparse Spike Inversion (CSSI)

The Constrained Sparse Spike Inversion (CSSI) algorithm, was developed by Jason Geosystems®, uses seismic traces to model subsurface reflectivities with some minimum number of reflection coefficients. The final results are driven by the seismic data, and the bandwidth is increased by the enforcement of sparsity. In this project, a wavelet and a low-frequency model were used as the basis for a constrained, broadband, sparse spike inversion that yielded the reflectivity model. Figure 4.6 shows a flow chart displaying the stages involved in a post-stack seismic inversion.

Constraints

The Constrained Sparse Spike Inversion models the input seismic data as the convolution the seismic extracted wavelet with the reflection coefficients defining the model. Because the wavelet is bandlimited, there is no unique solution to this problem. Therefore, additional constraints must be enforced to estimate a plausible result of several feasible mathematical solutions (Pendrel and Van Riel, 1997). These constraints define the variability of the inversion impedances away from the wells. A mean value or soft trend was defined for each well, and then an average trend was computed using all four wells. This trend is used to guide the acoustic inversion. The well constraints are defined based on the range of interval P-impedance, and they establish the allowable impedance solutions. However, the low-frequency component (usually 0 to 10 Hz) is absent

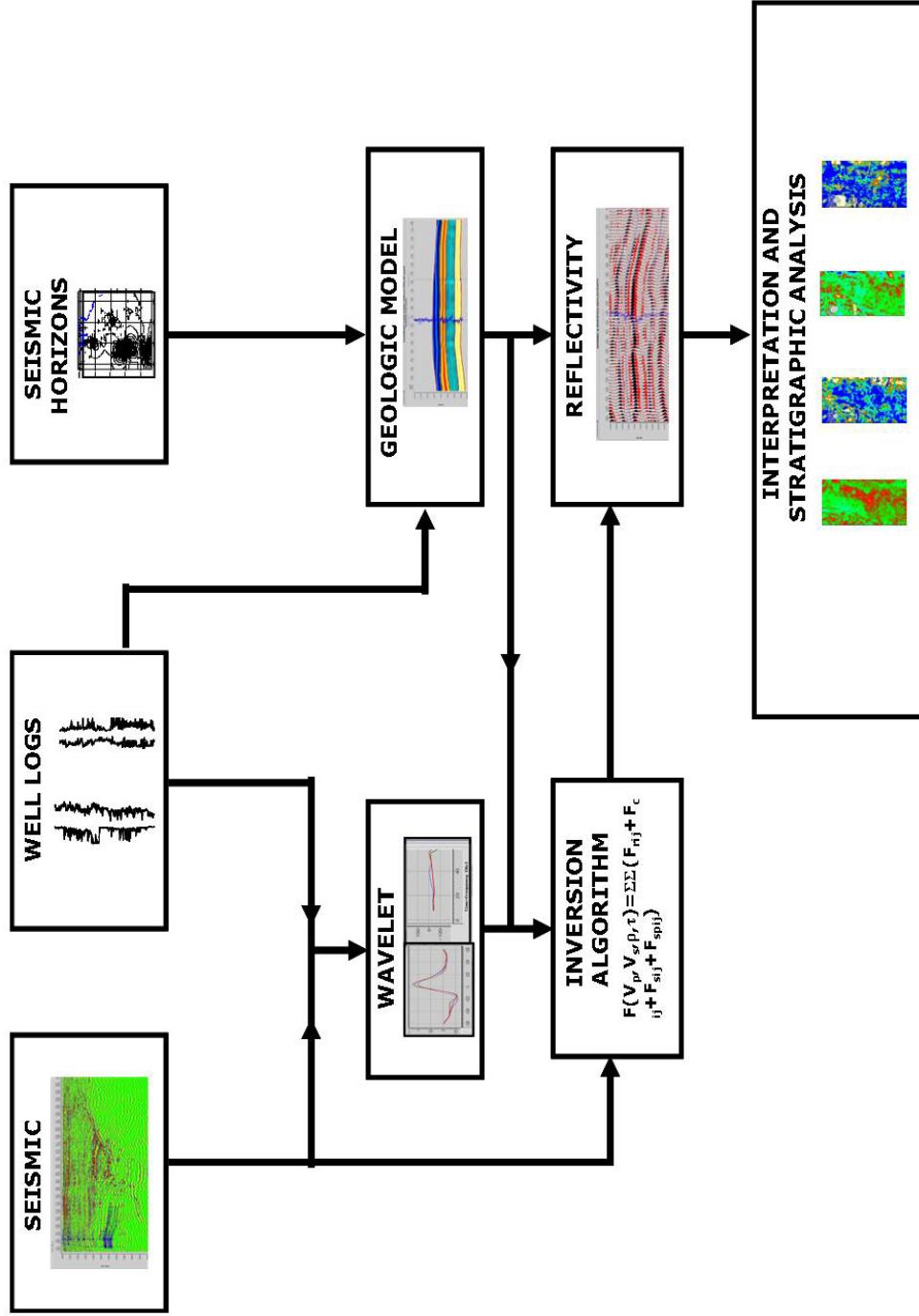


Figure 4.6 Flow chart of the post-stack inversion methodology used in this study. The fundamental inputs are seismic data, well logs, velocity surveys, and the seismic interpretation in the intervals to be inverted.

in the seismic data and hence must be interpolated from sonic log and check-shot data.

Filtering is necessary to accomplish the final trace merging. A high-cut filter (10 Hz) is applied the low-frequency data derived from the well log data, and a band-pass filter (10 to 60 Hz) is applied to the band-limited seismic data.

Sparsity control

The constrained sparse spike inversion minimizes a cost function (CF) subject to value-range constraints. The cost function is given by:

$$CF = [l_1 -norm*(Reflectivity)] + [\lambda * l_2(Seismic_misfit)]$$

First term

Second term

The first term of the equation represents the energy of reflectivity, and the second term represents the seismic misfit. The reflectivity energy term is the sum of the absolute values of the reflection coefficients and ensures sparsity of the reflectivity. The seismic misfit term indicates the difference between seismic and the synthetic and ensures a good fit with the seismic data.

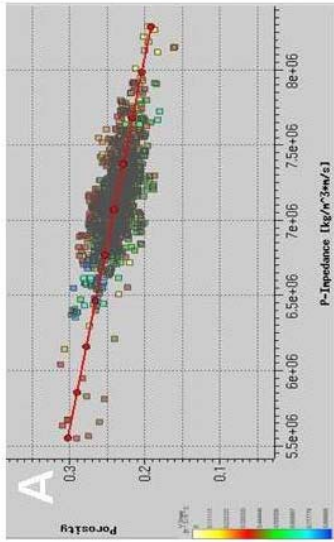
The parameter λ controls the density of spikes in the results. A small λ value will generate a few reflectors and high data residuals (error), whereas a larger λ value will generate many reflectors and a better seismic match. The two terms of the equation cannot be simultaneously reduced, become small residuals occur with a detailed model and a sparse model occurs with a significant data

mismatch. The scalar λ is a relative weight between two terms. A high λ value will also introduce too many insignificant reflectors and will make the results less sparse. The most appropriate λ value is the lowest λ value that produces a high signal-to-noise ratio and good well-log correlation results.

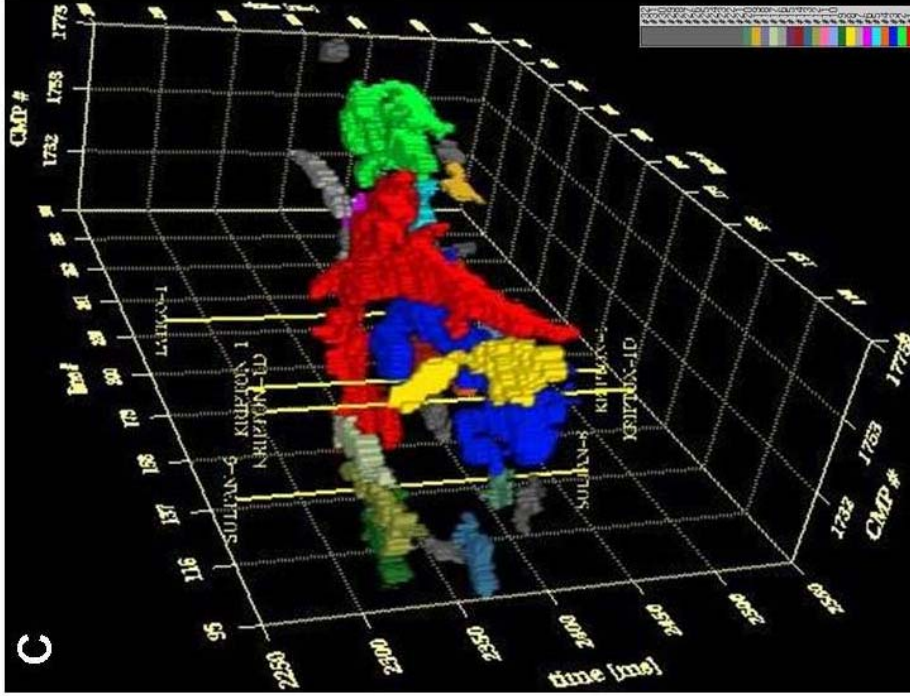
Porosity computation

In seismic inversion to acoustic impedance is used as a direct estimation tool of reservoir properties such as porosity, lithology, and fluid fill (Hegelsen et al., 2000; Latimer and Van Riel, 1996; Torres-Verdín et al., 1999). The conversion of acoustic impedance units to porosity is based on a linear relationship assumed between porosity and acoustic impedance that is applied to the total acoustic impedance volume generated during the inversion. Regression analysis performed on K field logs used to generate P-impedance for the total AI volume yielded desirable correlation coefficients is shown in Figure 4.7(A). The trend obtained from the crossplot of density porosity versus P-impedance was used to convert the total AI volume into a porosity volume. The porosity volume result was useful to establish the spatial variation of porosity and correctly identified more than 90 percent of the sand bodies drilled by the wells shown in Figure 4.7(B). Distinct high-porosity bodies (potential reservoirs) are extracted from the estimated porosity volume in Figure 4.7(C).

POROSITY/P_IMPEDANCE



POROSITY BODIES



POROSITY CUBE

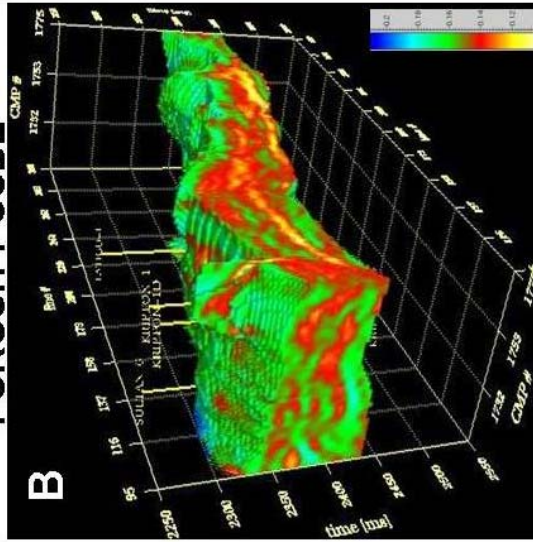


Figure 4.7 Porosity bodies extracted from P-impedance derived from post-stack seismic inversion.

4.3.6 Seismic horizons picking on the reflectivity volume

Seismic horizons interpreted in the post-stack seismic volume were carefully re-interpreted on the reflectivity volume to produce a new horizon set. The latter were mapped to produce additional attribute extractions of amplitude and inverted reflectivity describing spatial and vertical reservoir boundaries after wavelet effects are removed. Figure 4.8 displays a seismic line extracted in the vicinity of S-1 well and shows the comparison between interpreted horizons from the original seismic data and interpreted horizons from reflectivity derived from inversion.

The increase in seismic resolution can be seen, and an improved horizon correlation is achieved using the reflectivity cross-section.

4.3.7 Attribute Extraction

Many authors have been involved in seismic attributes studies, where the reservoir properties are correlated to seismic attributes (Del Valle Garcia et al., (1990); (Sonneland and Barkved, 1990); Lefeuvre and Chanet, 1993); (Magnier, 1994); (Dickerman et al., 1994); (Hansen, 1993, 1996); (Alam et al., 1995); (Hardage et al., 1995); (Matteucci, 1996); and (Gastaldi et al., 1997).

Seismic attributes that are not independent of each other are still useful for studying the time, amplitude, phase, frequency, and attenuation character of seismic data. Amplitude attribute maps were obtained for the inverted reflectivity data and compared with attribute maps constructed directly from seismic.

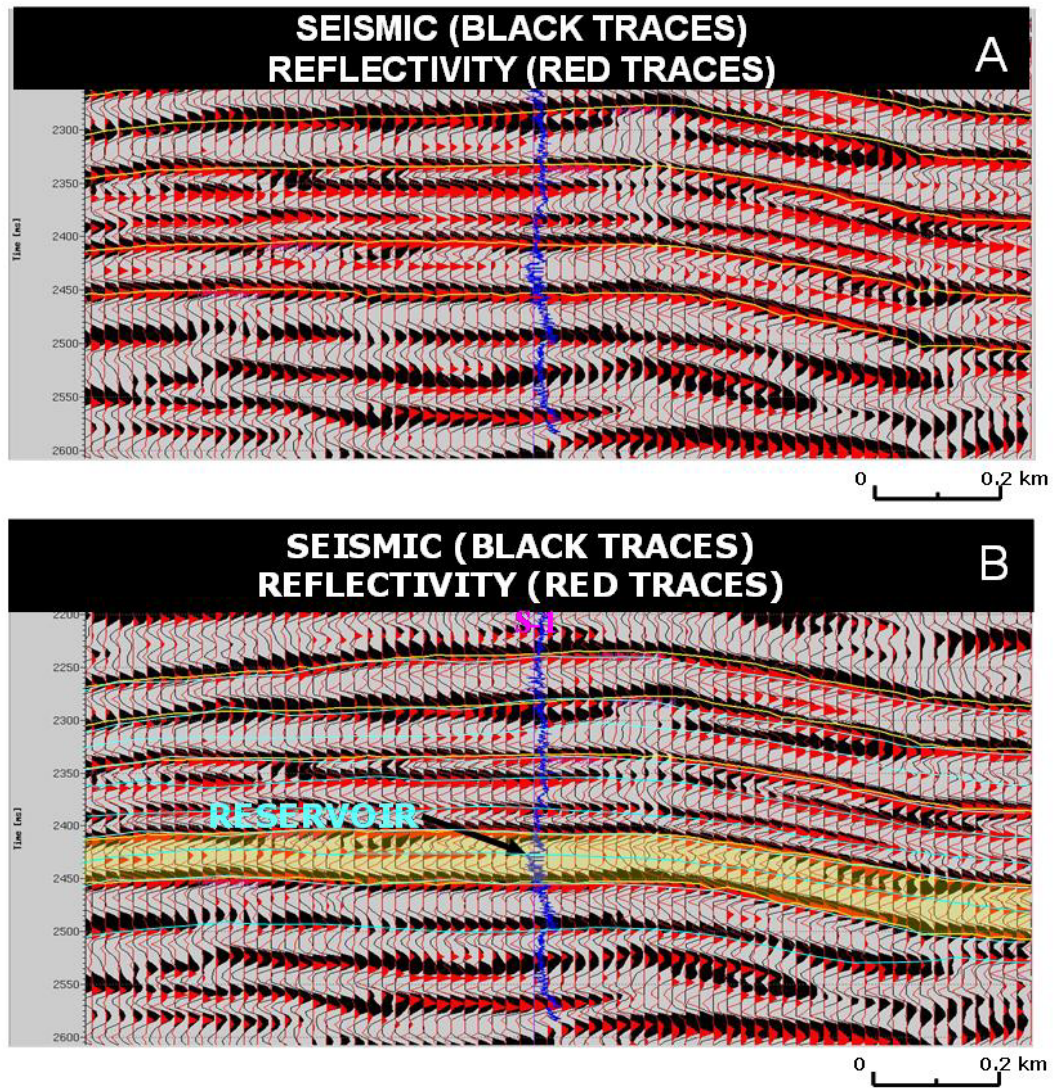


Figure 4.8 Seismic interpreted horizons and reflectivity interpreted horizons used to make a better detailed correlation of seismic interfaces. (A) Interpreted horizons, in yellow, on seismic post-stack data volume. (B) Interpreted horizons, in light blue, following the reflectivity derived from inversion.

Figure 4.9A is an extracted amplitude map at one reservoir interval that shows the comparison between a seismic amplitude map and a reflectivity amplitude map.

The map on the left does not show the real extension of the reservoir because it has the tuning effect, however the map on the right is showing better defined high amplitude anomalies oriented north-south, that suggest the strike orientation of sand bodies and the reservoir boundaries as well. The facies architecture consists of ridge sand bars deposited along the front and margins of the delta where the amalgamated ridge sand bars impart first-order strike orientation to the delta framework. Ridge sand bars coarsen upward and are produced by progradation of a marine shoreface.

Figure 4.9B is an extracted amplitude map at one reservoir interval from the K field that shows the comparison between a seismic amplitude map and a reflectivity amplitude map. The seismic reflection amplitude map on the left does not show the real extension of the reservoir because it is masked by the tuning effect; the map on the right shows better defined anomalies and the reservoir boundaries can be interpreted. The interpretation of this map consists of distal-bar deposits composed of interbedded sands, silt, and mud. Upward, the proportion and thickness of sand and silt beds increase. The interbedded sequence grades into hummocky, planar or low-angle trough cross-stratified sand. The principal structural risk of this map is close to the master fault, on the left, and down-dip growth fault to the east.

S FIELD

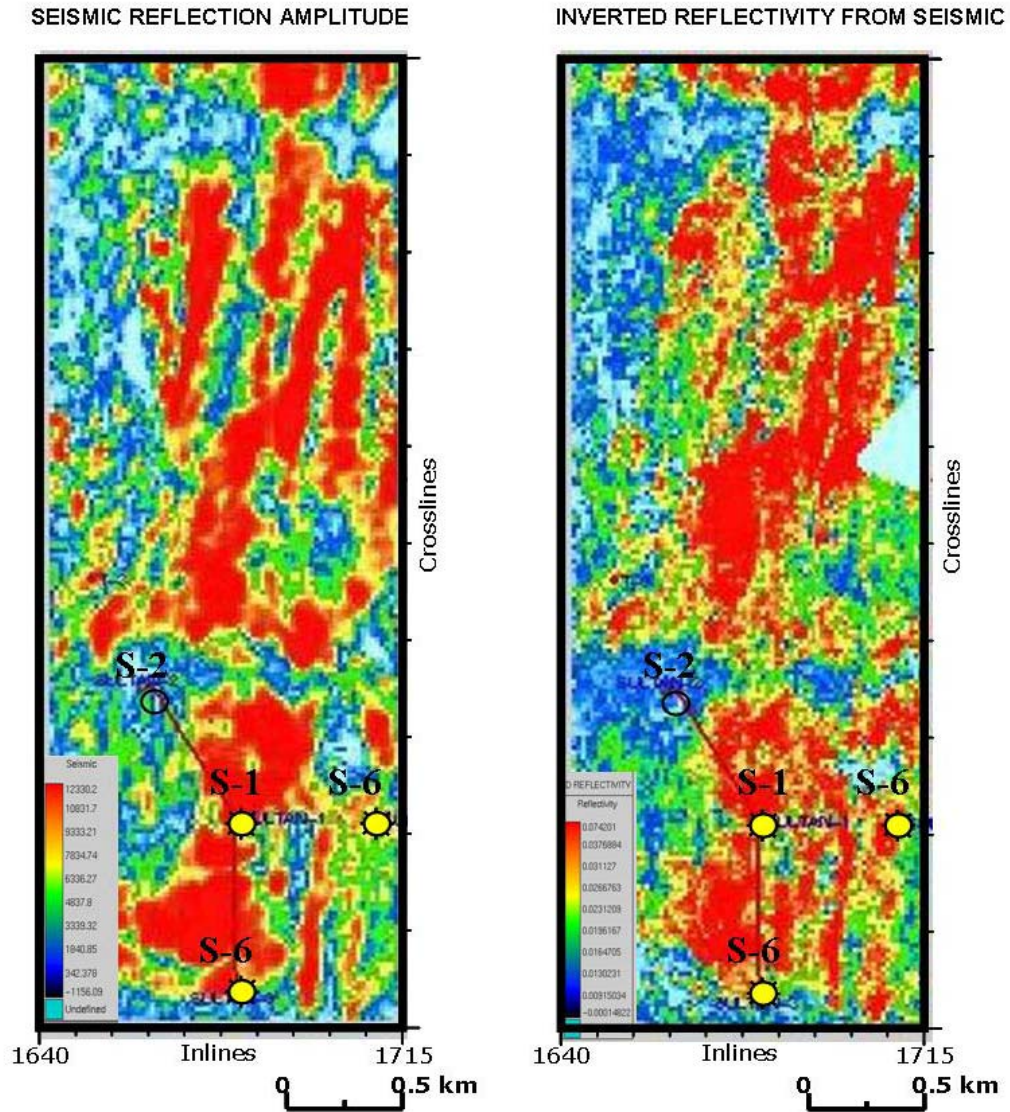


Figure 4.9A Amplitude map extraction for the reservoir interval in the S field. The map on the left is an amplitude attribute extraction from seismic in which the reservoir boundaries are not well delineated; the map on the right shows better defined boundaries where the S-3 well has been drilled and shows the real extension of the gas reservoir.

K FIELD

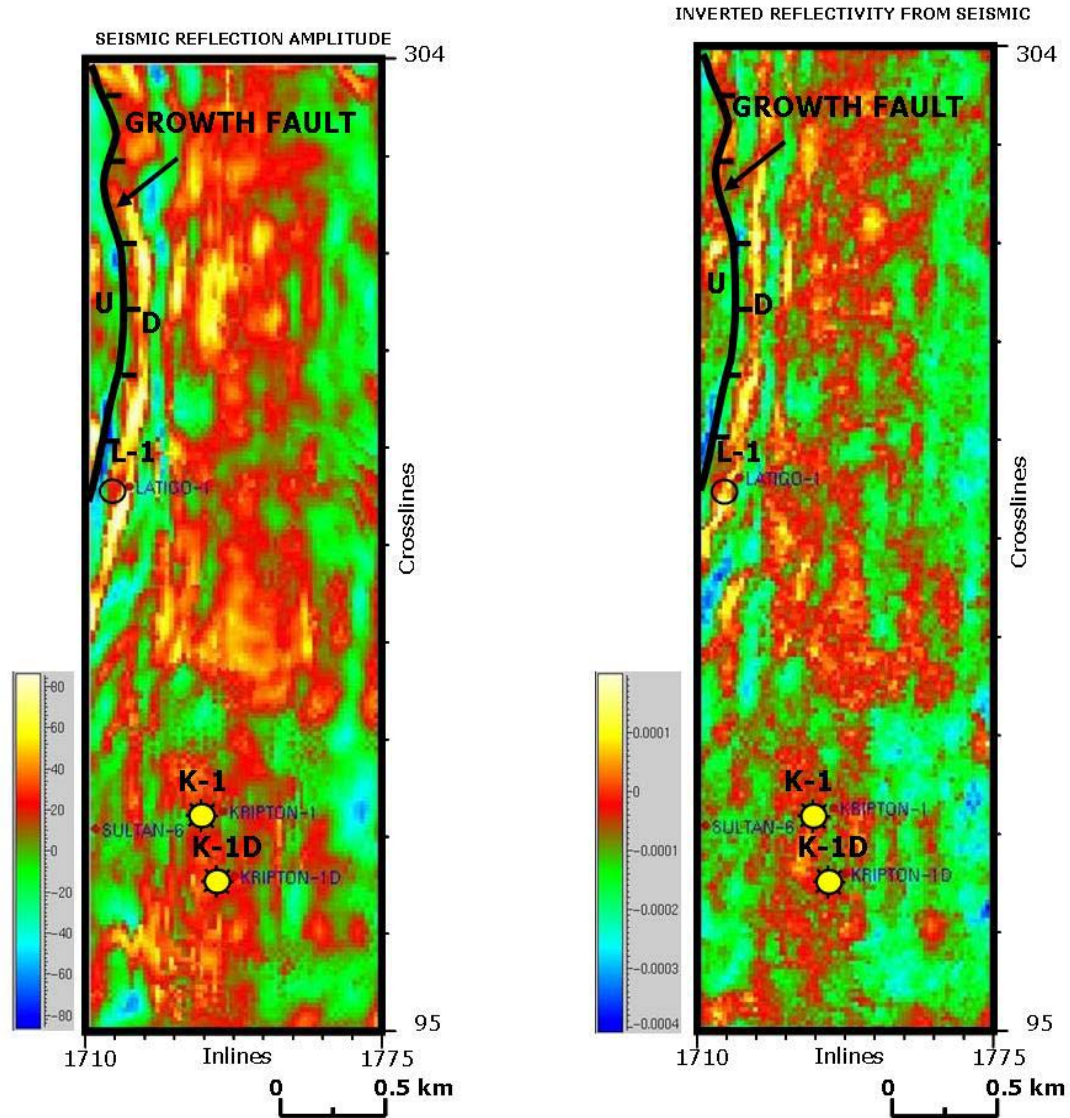


Figure 4.9B Amplitude map extraction for the reservoir interval in the K field. The map on the left is an amplitude attribute extraction from seismic in which the reservoir boundaries are not well delineated; the map on the right shows better defined boundaries of the gas reservoir.

4.3.8 Interpretation of amplitude attribute maps

Facies architecture interpretation in S field from the amplitude attribute map in Figure 4.10A, was supported by the net sand mapping of the stratigraphic unit D, in Figure 4.10B, which shows a north-south oriented or strike oriented distribution of sand bodies in this study. The interpretation of the amplitude attribute map extracted from the inverted reflectivity consists of strike-oriented bars, parallel to coast line, trending north-south and continuing northward, the facies architecture corresponds to ridge sand bars deposited along the front and margins of a wave-dominated delta, where successive constructional and destructional phase beach-ridge complexes amalgamate to form the delta-front sand wedge.

Analogue to Rio Grijalva, Southeast México

The Rio Grijalva, (satellite image, Figure 4.10C) and the Río Usumacita in the coastal lowlands of Tabasco flow into the Bay of Campeche in the southwestern part of the Gulf of México. Geologically and geographically, this region belongs to the Central American land-bridge between North and South America. The rivers flow as separate streams until they merge just before the mouth of the Bay of Campeche.

Numerous river arms and lakes (dark blue) document shifts in the river's courses during the last 400 years. Today, a part of the Río Usumacita's abundant water-flow is entering the Río Grijalva, while the remaining river waters flow into

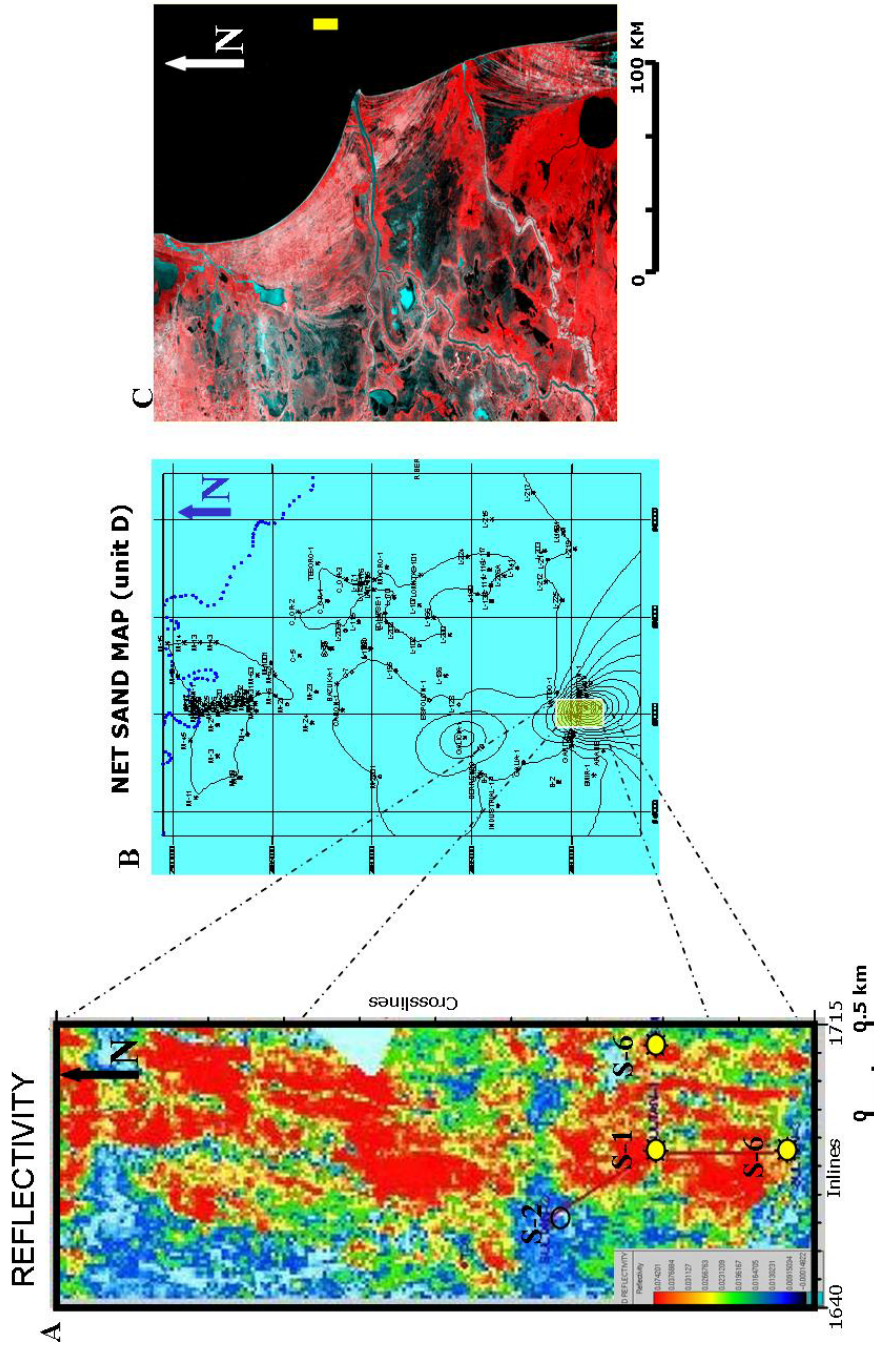


Figure 4.10 Sedimentary model interpreted from amplitude attribute map. (A) Amplitude map extracted from reflectivity derived from seismic inversion at reservoir interval in S gas field same as Figure 4.7a. (B) Net sand map constructed from well data in stratigraphic unit D showing the reservoir as a north-south pattern strike-oriented sand distribution. (C) Satellite image of the Rio Grijalva delta in southern México used as an analogue for the interpreted amplitude map in this study.

the sea. Both rivers have deposited sizeable sediment loads in the bottom-land and embankments (blue in the satellite image).

A series of beach ridges has formed near the coast, especially on the Río Grijalva delta. The ridges are strike-oriented in their development along the courses of the respective coasts and are visible in the conformation of the Río Grijalva Delta. The beach-ridge complex has led to island formation of lagoons where temporarily flooded areas lead to swamp formation (medium blue areas).

Features similar to the strike-oriented sand bars and dip-oriented channels are observed in the seismic reflectivity map of the subject area.

4.4 CONCLUSIONS

- Reflectivity modeling helps in stratigraphic analysis at the reservoir scale. The stratigraphic model can be used in several ways to improve the reflectivity model, enhancing the vertical and spatial resolution and leading to the interpretation of internal facies architecture of the sedimentary sequences.
- The interpretation of flooding surfaces from well log models and reflectivity models provides an additional control on time-depth relationships. The flooding surfaces interpreted in northern Mexico were correlated with southern Texas because there are similar characteristics in well response.
- The inverted reflectivity modeling helped to improve the vertical resolution and horizontal continuity of seismic events. Amplitude attribute

maps extracted from reflectivity at reservoir intervals showed better defined sequences and the reservoir boundaries could be spatially delineated.

- Reflectivity amplitude maps were constructed to make an interpretation of the sedimentary model based on the inverted reflectivity.
- In the S field, the facies architecture consists of ridge sand bars deposited along the front and margins of the delta, where the amalgamated ridge sand bars impart first-order strike orientation to the delta framework. Ridge sand bars coarsen upward and are produced by progradation of a marine shoreface.
- In the K field, the facies architecture is correlated to distal bar deposits composed of interbedded sands, silt, and mud. Upward, the proportion and thickness of sand and silt beds increase. The interbedded sequence grades into hummocky, planar or low-angle trough cross-stratified sand.
- The final attribute maps helped in the development of the gas fields, positioning new wells and better relocating some programmed wells.

Chapter 5

Stratigraphic Analysis of Reflectivity Data II: Lamé Petrophysical Parameters as Lithology and Fluid Discriminators

5.1 INTRODUCTION

Angle dependent inversion (ADI) transforms multiple angle-stacks into acoustic and shear impedances, and density volumes. Analysis of these volumes produces Lamé's elastic parameters, λ and μ , which are useful for discriminating lithology from fluids. From well log petrophysical data analysis we expect reservoir sandstones to exhibit lower values of λ and higher values of μ (Goodway et al., 1997, Barrios-Rivera et al., 2002). Angle-dependent inversion was applied to the S and K gas fields, in the Burgos Basin of México (Figure 5.1). Prospective interval extends from target depths of 2800 to 3550 m. These gas fields occur in clastic sediments within the Vicksburg Formation. Sedimentary models indicate a wave-dominated delta and a growth-fault structural environment for the sediments. Goals of this study were to determine the extension of the gas reservoirs and to predict rock quality, and to better understand reservoir geometry and continuity.

5.1.1 Data set

PEMEX provided a high-quality 30-fold 3D seismic survey that was acquired in 1999, that allowed local geoscientists to interpret a new structural trend related to a growth fault. Some structural prospects have been drilled

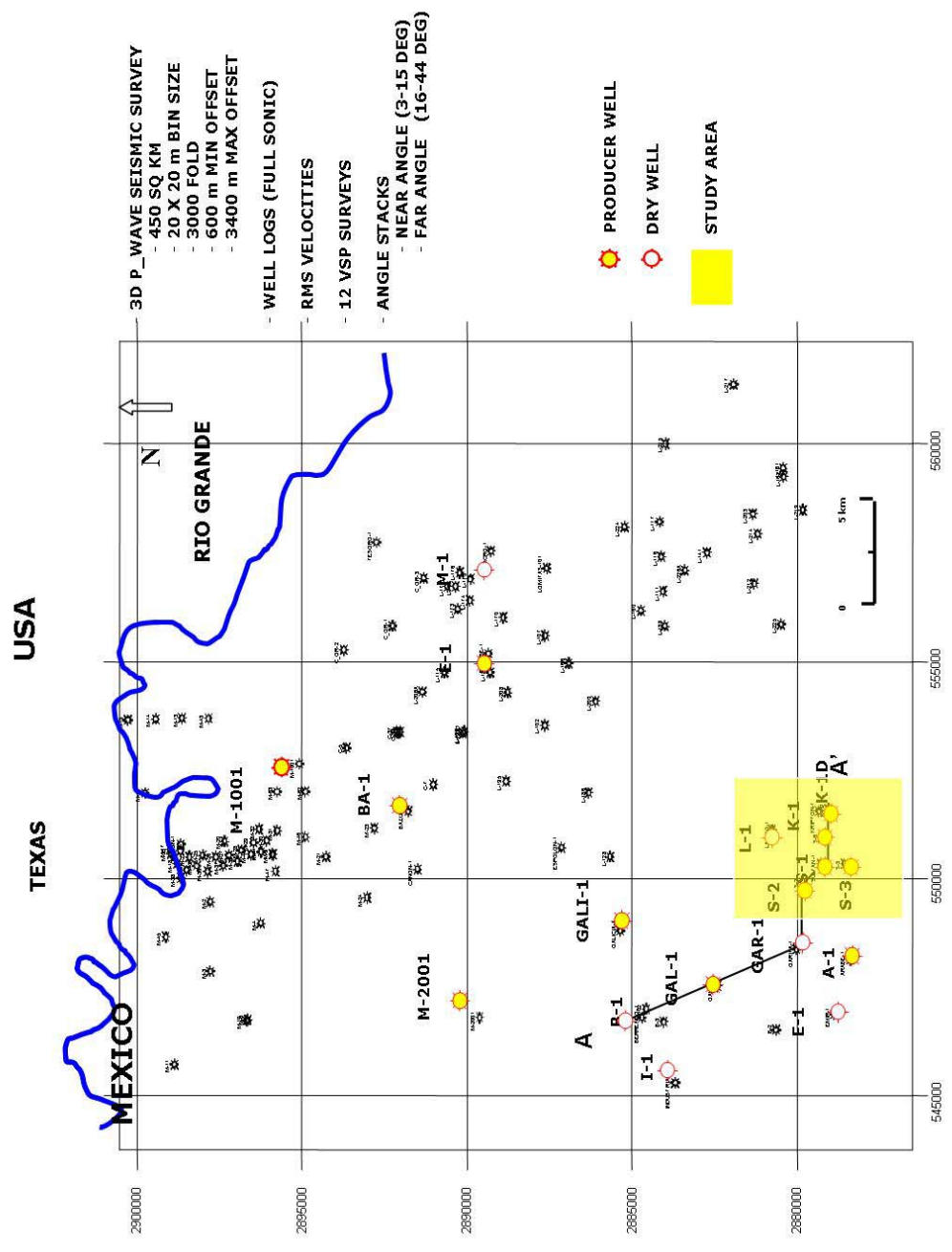


Figure 5.1 Location map of study area displaying key well locations and the study area (in yellow). Well correlation A-A' corresponds to Figure 2.5, shown in Chapter II.

successfully. The bin size is 20 x 20 m. Offsets ranged from 620 to 3420 m. and provided a suitable range of angle information at the target interval. The seismic data have been pre-stack migrated, with angle stacks of 3 to 15 degrees and 16 to 44 degrees extracted. A complete set of well logs, including P-wave sonic, S-wave sonic, and density logs from the reservoir interval was available for this study.

5.2 METHODOLOGY

This study involves eight main steps:

1. Well logs were analyzed to determine reservoir quality rocks.
2. Porosity ranges were discriminated in acoustic and shear impedance domains. This was done by crossplotting analysis of well log data across these reservoir intervals.
3. Angle dependent inversion was performed to estimate the P-impedance, S-impedance, reflectivity, and density volumes.
4. Reflectivity analysis data from near-angle and far-angle stacks were used to re-trace seismic horizons.
5. Attribute extraction from pre-stack reflectivity data was performed to estimate the facies architecture of the reservoirs. Extracted attributes consisted of the λ and μ elastic constants and density ρ .
6. Lamé's parameters, λ and μ , were computed from acoustic and shear impedances and combined with density volumes to discriminate between rocks and fluids.

7. A porosity volume was estimated from acoustic and shear impedances and density volumes, as well, as bulk and shear modulus relationships.
8. Facies architecture was interpreted for the gas reservoirs in the study area.

5.2.1 Petrophysical Analysis

Petrophysical analysis was achieved for eleven key wells with a complete set of log curves, including caliper, spontaneous potential (SP), gamma ray (GR), resistivity (LLD, ILM, ILD), neutron-porosity (NPHI), density-porosity (DPHI), bulk density (RHOB), sonic (BHC), and dipole sonic log (DSI). Detailed log analysis consisting of volume of shale, effective porosity, and water saturation at reservoir intervals was accomplished in those key wells. Laboratory petrophysical analysis from core data was useful for calibrating porosity, as well as the shear and bulk moduli, which were used in Lamé's petrophysical parameter computations. This calculation was already explained in chapter III, and the final results were used in this part of the study.

5.2.2 Angle-Dependent Inversion

Angle-dependent inversion requires the calculation of elastic impedance for each well as a function of angle θ (Connolly, 1999). A wavelet was estimated for each angle stacked data set, and these angle stacks volumes were inverted with Jason's software using the Simultaneous Constrained Sparse Spike® Inversion algorithm (Figure 5.2). This algorithm is an extension of the zero-offset

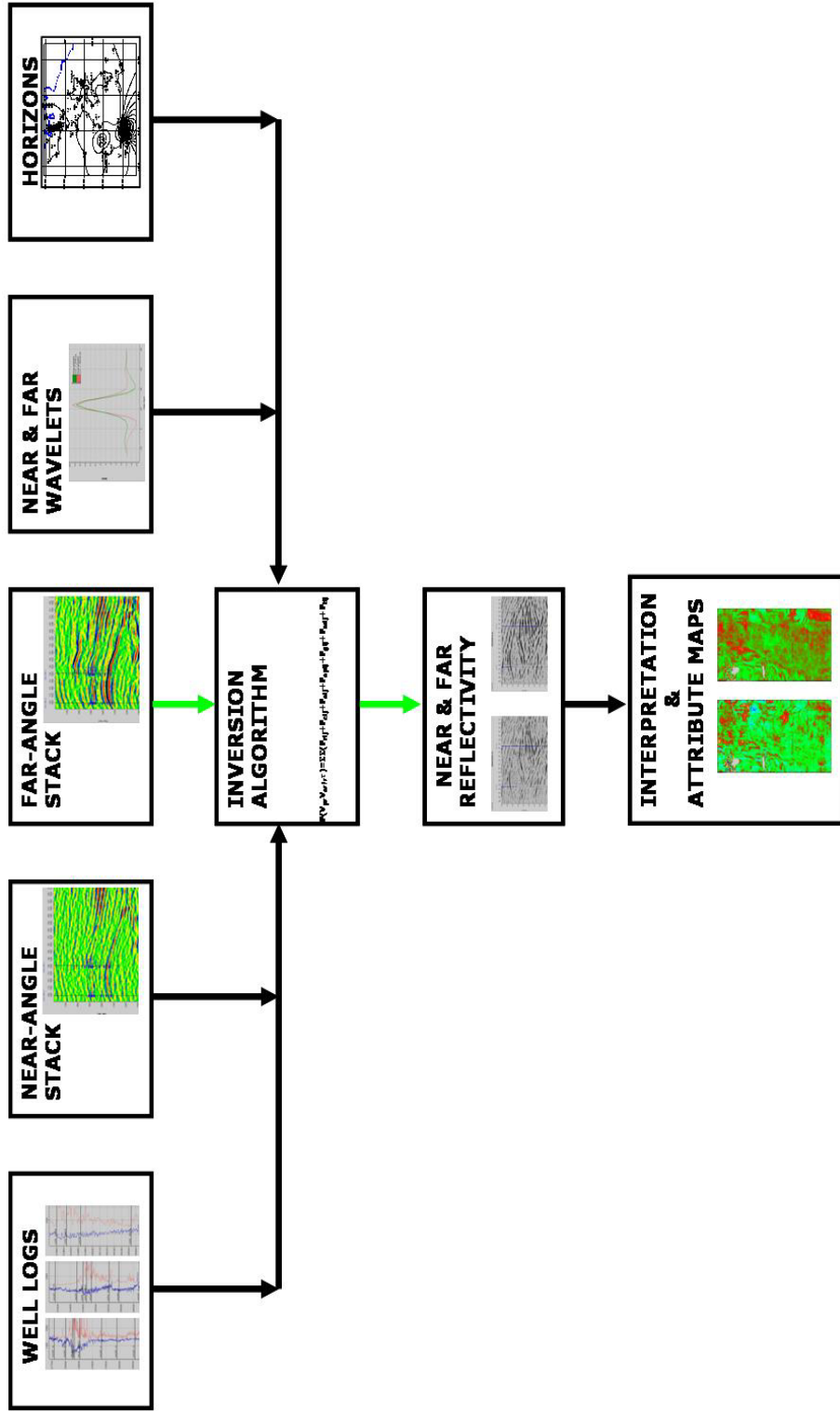


Figure 5.2 Flow chart describing the methodology of simultaneous inversion of partial stack seismic cubes. The inputs necessary to accomplish this process are the angle stacks, well logs, and seismic horizons. The well logs are used to compute elastic impedance using the P-wave, S-wave and density logs; the angle stacks are used to define the amplitude behavior with incidence angle.

CSSI method in which a single volume of stacked seismic is inverted into a normal acoustic impedance data set (Pendrel and Van Riel, 1997).

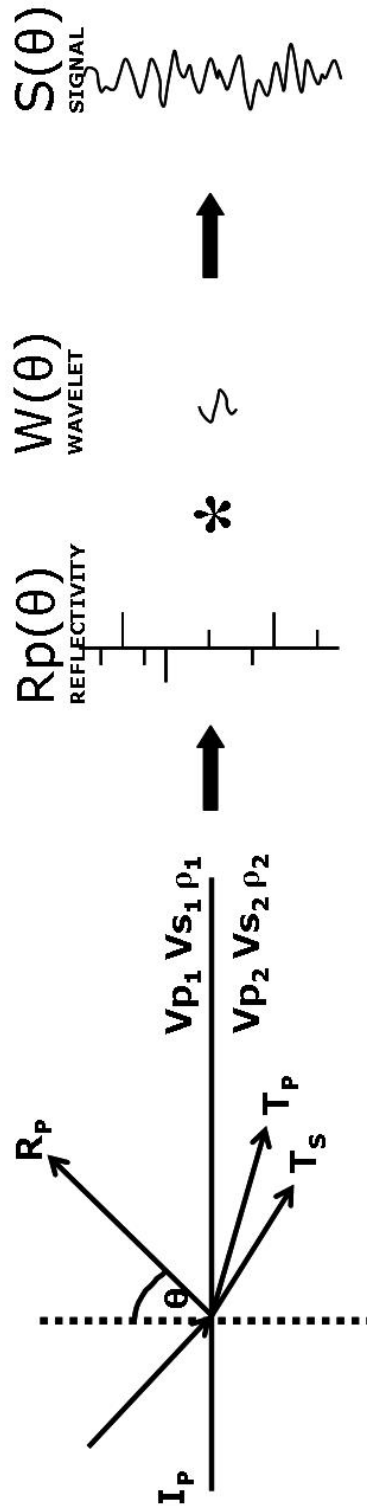
In simultaneous inversion, the seismic amplitude variation with angle is incorporated into the inversion process in the form of partial stacks. It is assumed that the convolutional model still holds at non-zero angles (Figure 5.3), but the well log impedance (density x velocity) is no longer the appropriate reflectivity. The convolutional model for angle-dependent inversion is shown below.

5.2.3 Angle Sub-Stacks Computation

Amplitude versus angle (AVA) describes elastic reflectivity as it varies with angle of incidence. Traces from a common mid-point (CMP) gather are defined by offset only, but the variation of reflection amplitude from interfaces in the subsurface depends on the angle of incidence. Elastic inversion of far offsets, therefore, requires data to be gathered over ranges of known angles of incidence.

The traces of each CMP gather are split spatially and temporally into a range of angles using the velocity function at each gather to calculate how the normal CMP gather should be split into ranges of angle of incidence. Angle gathers from a particular angle range are then stacked to produce angle stacks. The number of stacks depends on the number of angles chosen. For AVA inversion analysis, near-angle and far-angle stacks are produced, and perhaps also mid-angle stacks. Input to the construction of angle gathers should be fully normal move out (NMO) corrected, stretch muted, and pre-stack migrated CMP gathers. Multiple and general noise attenuation through stacking will not be as

ANGLE-DEPENDENT CONVOLUTIONAL MODEL



Where,
 $S(\theta) = R_p(\theta) * W(\theta)$
 $S(\theta)$ = IS ANGLE SEISMIC
 $R_p(\theta)$ = IS ANGLE REFLECTIVITY, CALCULATED FROM ZOEPRITZ EQUATIONS
 (USING WELL P-SONIC, S-SONIC, AND DENSITY LOGS)
 $W(\theta)$ = ANGLE WAVELET, ESTIMATED USING ANGLE REFLECTIVITY AND ANGLE SEISMIC

Figure 5.3 Illustration of the angle-dependent convolutional model.

effective as usual CMP stacking because the angle gathers will not contain the full range of offsets or have the fold found in conventional CMP gathers. Therefore, pre-stack multiple attenuation on normal gathers is preferable. As with inversion of full-offset stack data, the post-stack processing sequence should be kept simple, but signal enhancement techniques may be required.

Angle stacks were computed using Hampson & Russell® software. The migrated gathers were provided by PEMEX Exploración y Producción of Reynosa, Tamaulipas, México. Angle stacks were calculated using the rms velocities. Figure 5.4 outlines the complete process to compute the angle stacks. The input data necessary to compute the angle stacks are the pre-stack time-migrated gathers and the rms velocities along with the acquisition geometry. CMP gathers were transformed into angle gathers and then summed into subsets of reflection angles. For this study the angle gathers were stacked into two large subsets, near and far. Near-angle gathers included incidence angles from 3 to 15 degrees. Far-angle gathers included incidence angles from 16 to 44 degrees.

5.2.4 Elastic Impedance Computation

Elastic impedance is a derived parameter calculated from angle-stacked reflectivity. Borehole-derived elastic impedance was calculated using the density, compressional, and shear sonic logs in the S-1 and K-1 wells. Elastic impedance is defined as the impedance whose reflectivity corresponds to the reflectivity of angle-stacked reflection amplitudes. Elastic impedance must be calculated when P_impedance alone does not characterize the reservoir and the P_impedance

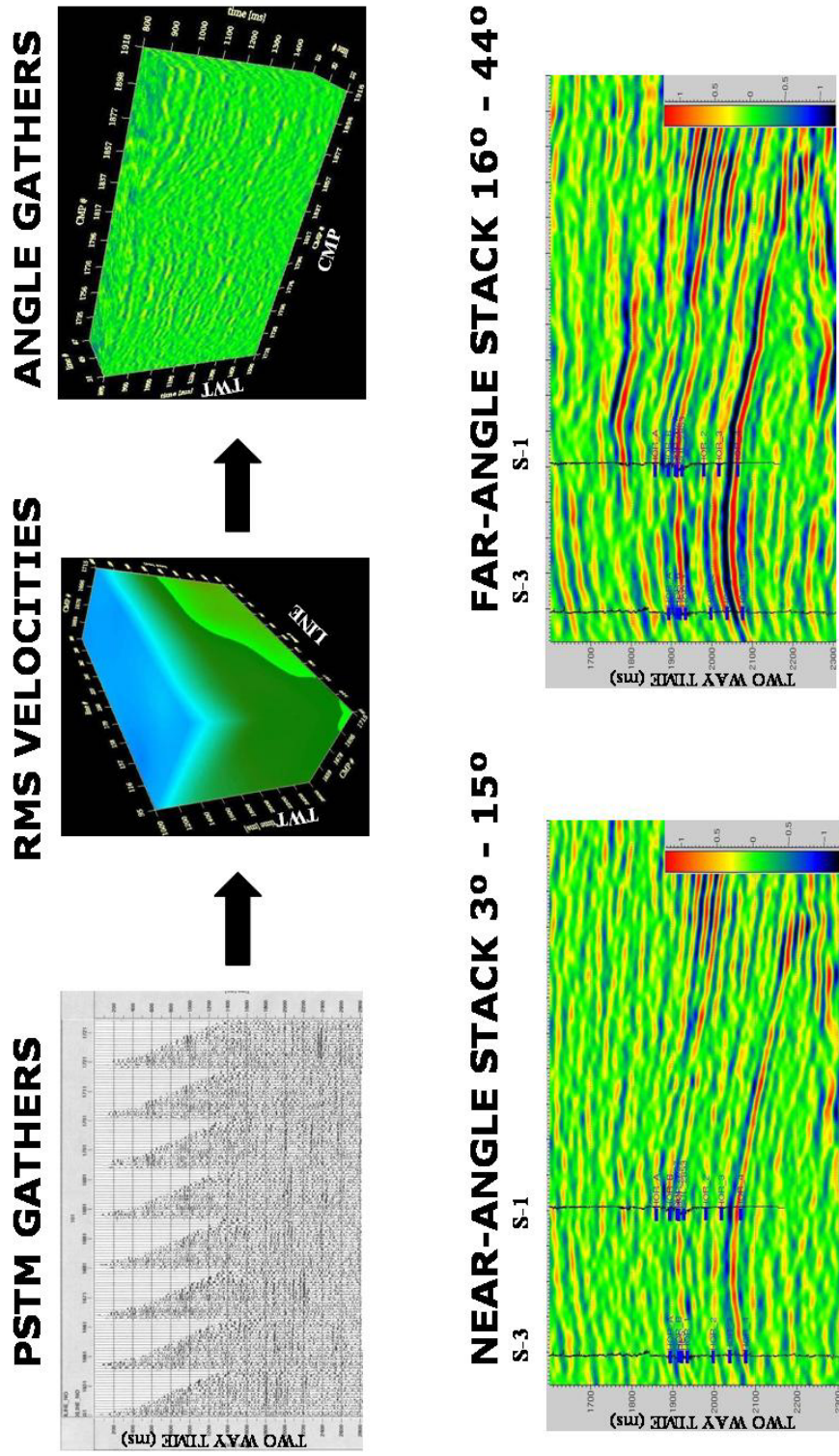


Figure 5.4 Methodology used for the computation of angle stacks. The initial inputs are the time migrated gathers and the rms velocities. The gathers are converted into incidence angle gathers, then the angle gathers were stacked into two families: near-angle stack including 3-15 degrees and far-angle stack from 16-44 degrees. The variation of amplitude versus incidence angle can be seen in the near and far seismic displays.

versus S_impedance crossplot show separation. There are several methods for calculating elastic impedance from full Zoeppritz representations, the Aki-Richards approximation of Zoeppritz, and a method published by Connolly (1999). The analysis of the elastic impedance versus acoustic impedance over the available seismic angle ranges gives an indication of how successful the subsequent inversion to elastic impedance will be in discriminating fluids and lithology. In Figure 5.5 images from elastic and acoustic impedance, and near-angle and far-angle reflectivity values computed in the S-1 well are displayed to show the AVA effects. The crossplot P_impedance versus S_impedance, in the upper image, shows separation between the two impedances hence indicating potential AVA effects.

The lower images display the elastic and acoustic impedance derived from log data; the red line corresponds to the acoustic impedance, and the cyan line is the elastic impedance. Differences between two impedances can be seen at reservoir intervals in the far-angle elastic impedance results.

5.3 REFLECTIVITY ANALYSIS

Once the angle-dependent inversion was accomplished, the resulting products were the near-angle and far-angle reflectivities. In the next section of this chapter, a pre-stack reflectivity analysis will be performed with the following steps:

- Seismic horizon tracing on near-angle and far-angle sets

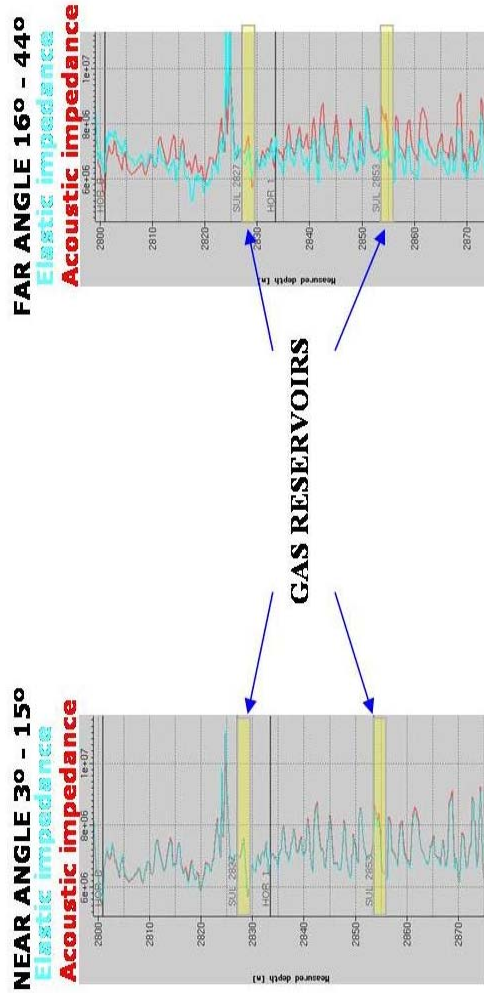
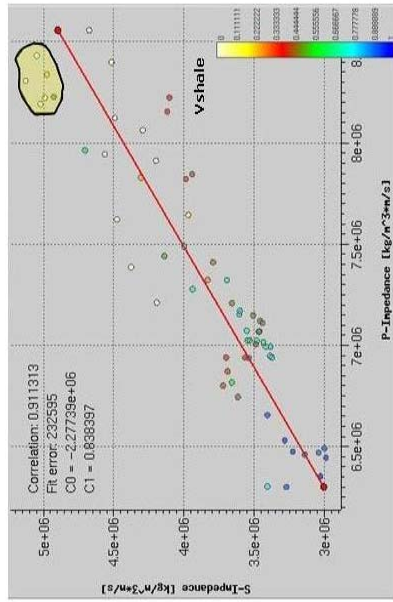


Figure 5.5 Elastic and acoustic impedance computation in the S-1 well. For the near-angle stack the result is comparable to zero offset or zero incidence, but for the far-angle stack, the elastic impedance shows range changes in reservoir intervals. This behavior indicates that fluids are present.

- Seismic horizon re-tracing on near-angle and far-angle reflectivities derived from angle-dependent inversion.
- Amplitude attribute maps from seismic and reflectivity angle stacks.
- Interpretation and relationships of sedimentary facies.

Six seismic horizons were traced in the near-angle and far-angle seismic stacks Figure 5.6. Nine horizons were re-traced in the reflectivity volumes derived from inversion for the near and far stack to give a more detailed interpretation. The dotted horizon in the seismic and reflectivity displays was used to compare various attribute maps.

5.4 AMPLITUDE ATTRIBUTE EXTRACTION

Amplitude attribute maps were generated using the reflectivity from post-stack inversion and near-angle and far-angle reflectivities from pre-stack inversion as input and were then interpreted to estimate the spatial distribution of reservoirs.

In Figure 5.7, (A) full-angle reflectivity, (B) near-angle reflectivity, and (C) far-angle reflectivity are shown for S field and (D) full-angle reflectivity, (E) near-angle reflectivity, and (F) far-angle reflectivity for K field at reservoir intervals, respectively. In both cases, the best response of the reservoir boundaries is given by the far reflectivity.

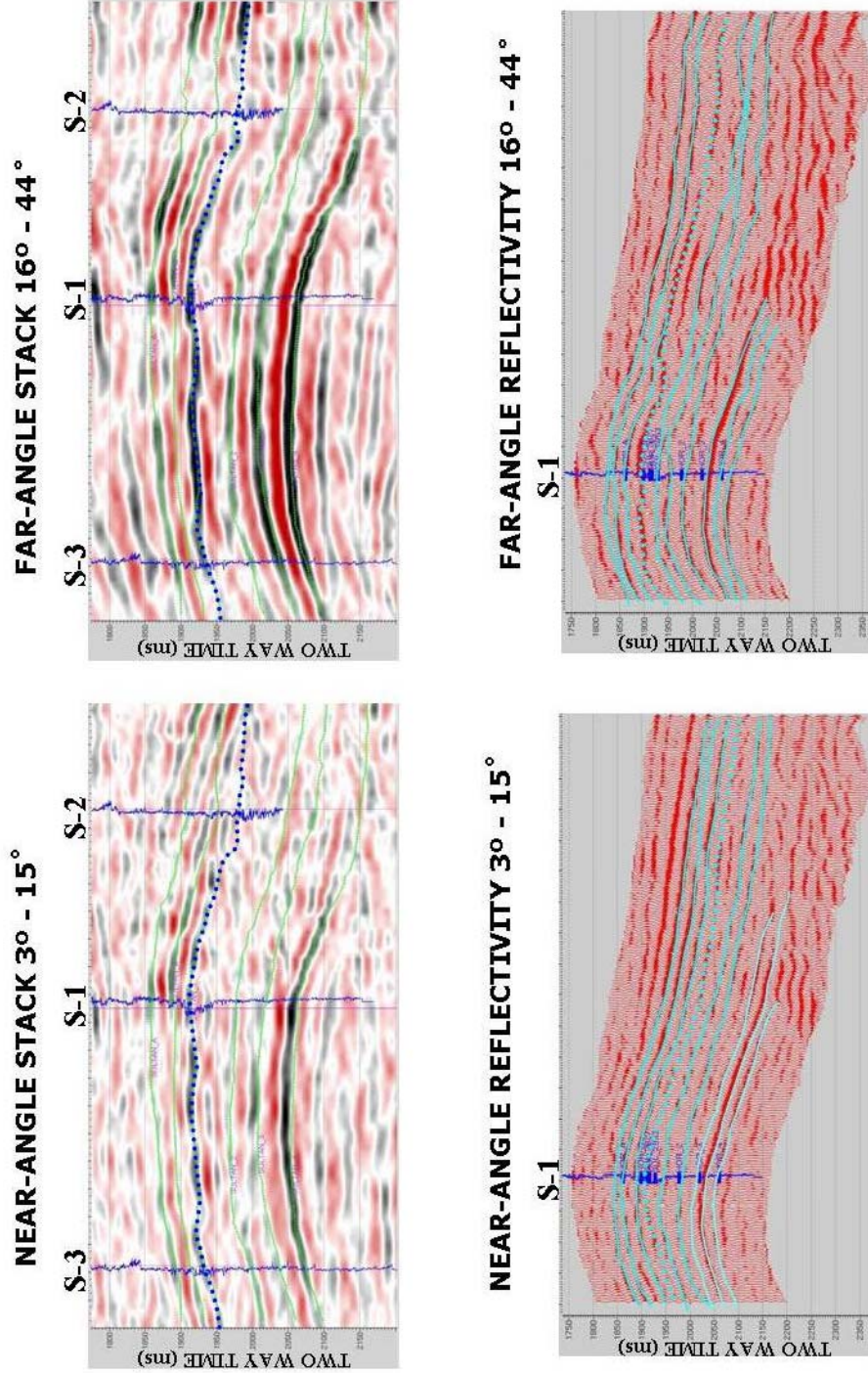


Figure 5.6 Comparison between the seismic interpretation and a detailed tracing of horizons on the reflectivity. The dotted horizons were used to extract the amplitude maps at the reservoir interval.

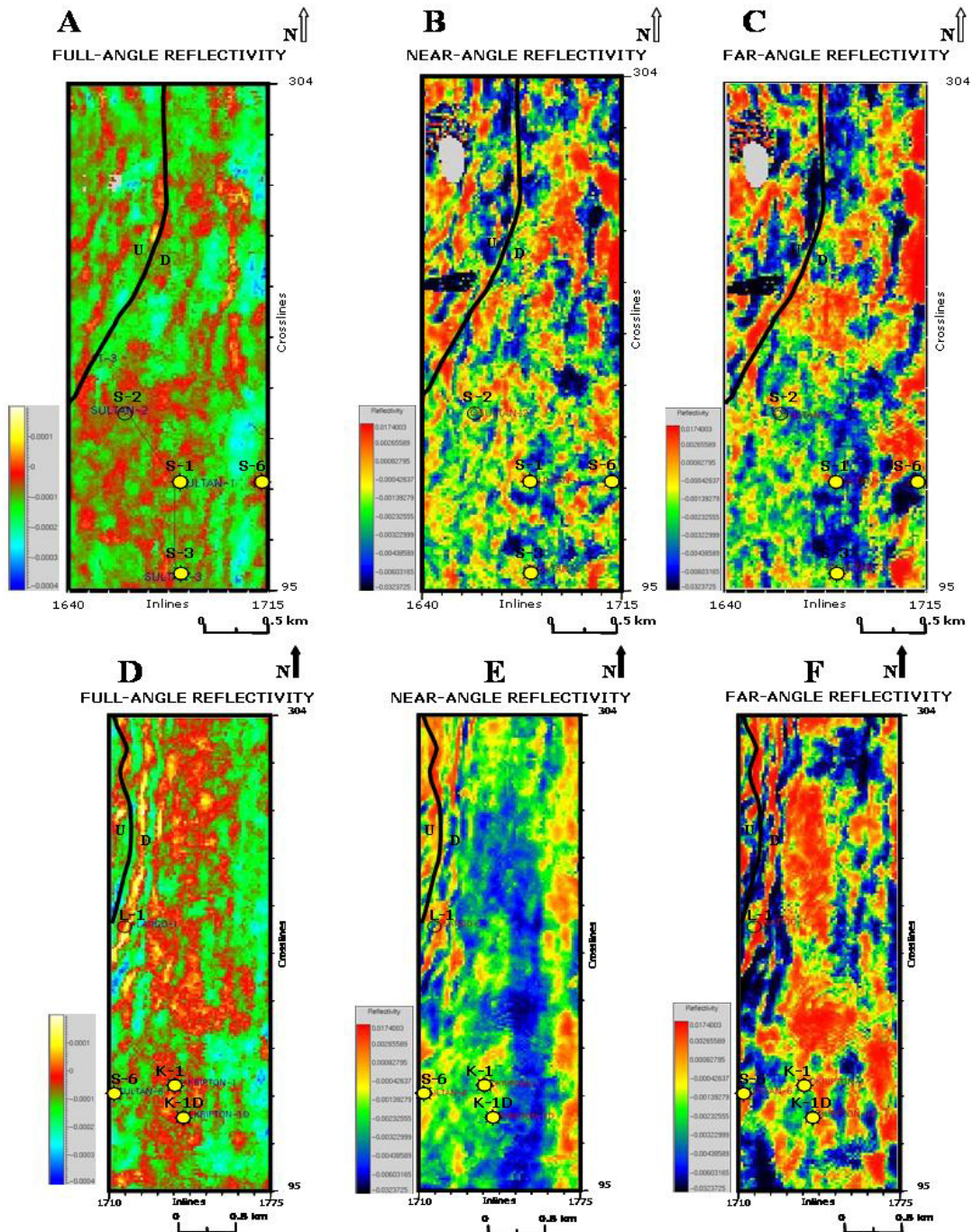


Figure 5.7 Amplitude maps displaying the reflectivity from post-stack and pre-stack inversion across the S and K fields. In both cases, far-angle reflectivity shows the best response in terms of fluid discrimination and rock quality.

5.4.1 S Field Amplitude Attribute Reflectivity Maps

- (A) This is an amplitude map of the inverted reflectivity from the full-angle reflectivity, and it shows a good spatial delineation of the reservoir. In this map north-south oriented anomalies interpreted as sand bodies parallel to the coast line are displayed.
- (B) This is an amplitude map of the inverted reflectivity extracted from the near-angle substack from 3° to 15° of incidence angle. It shows a subtle change in sign (negative values) of the reflectivity in the reservoir zone. This change in sign is related to the shale effect in the reflectivity model. Near-angle reflectivity, or the close to zero incidence-angle map, is similar to the full-angle reflectivity or zero-offset map.
- (C) This is an amplitude map of the inverted reflectivity extracted from the far angle including incidence angles from 16° to 44° . This map shows an interesting feature in the reservoir area, consisting of a strong negative anomaly due to the volume of the shale effect.

5.4.2 K field Amplitude Attribute Reflectivity Maps

- (D) This is an amplitude map of the inverted reflectivity from the full-angle reflectivity showing a good spatial resolution in the reservoir zone. This map shows strike-oriented anomalies

related to distal sand bars within a wave-dominated delta system.

- (E) This is an amplitude map of the inverted reflectivity extracted from the near-angle substack from 3° to 15° of incidence angle. Positive anomalies can be seen where the K-1 and K-1D wells were drilled. The interpretation of this map is that the volume of shale effect is present in this map, displaying a north-south negative anomaly to the east of the K field. This map is similar to the full-angle reflectivity because was built in ranges close to the zero-incidence angle.
- (F) This is an amplitude map of the inverted reflectivity extracted from the far angle stack involving incidence angles ranging from 16° to 44° . The positive anomaly in reflectivity is stronger than that in the near-angle map. This response reflects to the rock quality more than to fluids, because the lithology of the reservoir is related to shaly sands.

5.5 LAMÉ PARAMETERS, ROCK QUALITY, AND FLUID DISCRIMINATION

Using P-impedance, S-impedance, and density volumes, the Lamé's petrophysical parameters, $\lambda \cdot \rho$ and $\mu \cdot \rho$, were computed and interpreted as lithology and fluids discriminators.

From the petrophysical analysis the ranges from the Lamé's parameters were obtained. These values were useful to constrain the volumes from the petrophysical properties.

5.5.1 Lambda/mu Ratio Maps

Lambda/mu ratio is related to V_p/V_s by

$$\left(\frac{V_p}{V_s}\right) = \sqrt{\frac{\lambda}{\mu} + 2} \quad \left(\frac{V_p}{V_s}\right)^2 = \frac{\lambda}{\mu} + 2 \quad \frac{\lambda}{\mu} = \left(\frac{V_p}{V_s}\right)^2 - 2$$

For the S reservoir,

$$\frac{\lambda}{\mu} \cong 1.31 \quad V_p \approx 3787 \text{ m/s} \quad V_s \approx 2080 \text{ m/s}$$

For the K reservoir,

$$\frac{\lambda}{\mu} \cong 1.15 \quad V_p \approx 3630 \text{ m/s} \quad V_s \approx 2045 \text{ m/s}$$

In Figure 5.8, lambda/mu ratio final extraction is shown in a section view (A) and an extracted map (B) from the reservoir at 2827-2847 m through the S-2, S-1, and S-3 wells in the S field. The lambda/mu ratio section (A) shows the

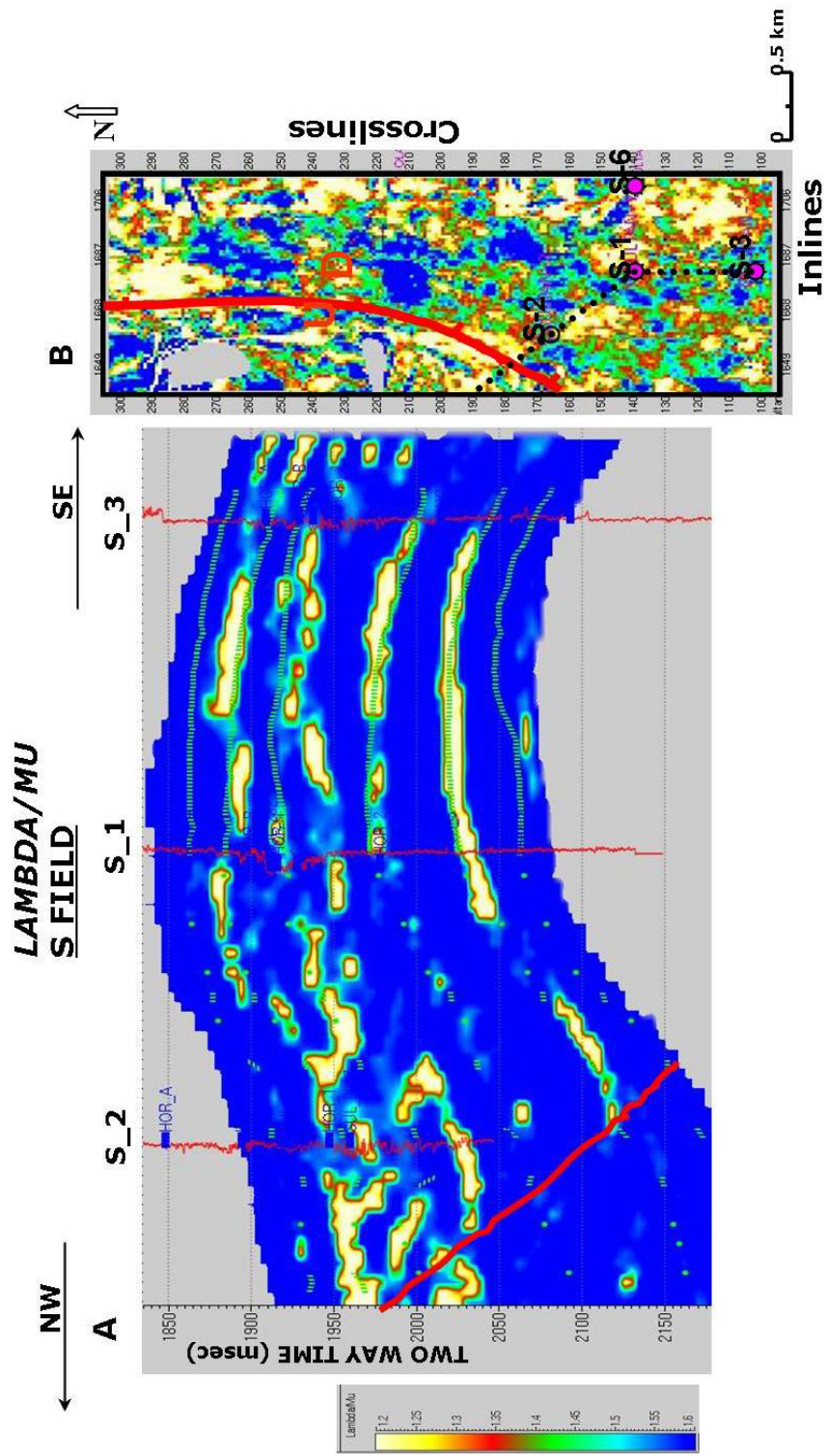


Figure 5.8 Section and map showing the extraction of lambda/mu ratio in the S field.

definition at the reservoir zone with a series of anomalies following the structural trend. The range of values of λ/μ ratio in the reservoir for the petrophysical analysis is between 1.25 and 1.35. Therefore, according to the scale in the left of the figure, the anomalies in yellow and red correspond to the range of values in which the gas reservoir is included. This section shows a series of interrupted anomalies at the reservoir interval. Otherwise there are a good continuity amplitude anomalies, above and below the reservoir, where shaly rocks have been drilled, which means that the best response in the λ/μ ratio map is related to shaly intervals.

The map (B) on the right was extracted from a seismic horizon tied with the top of the sand of the reservoir. This map is displaying anomalies with values for λ/μ ratio between 1.05 and 1.25 oriented north-south. These anomalies show that wells S-1 and S-6 have been drilled in low values of λ/μ ratio and wells S-2, and S-3 were drilled in a high value of λ/μ ratio.

Lithologically this means, that wells S-1 and S-6 must be more sandy than wells S-2 and S-3, which is the case. In this map, λ/μ ratio is useful to discriminate lithology from sands and shales. Comparing this λ/μ ratio map against that from post-stack reflectivity map in Figure 4.10A (Chapter 4), it can be shown that the λ/μ ratio map is useful as a lithologic discriminator. Strike-oriented anomalies related to delta-front sand bars are displayed in this λ/μ ratio map.

In Figure 5.9, lambda/mu ratio final extraction is shown in a section view (A) and extracted map (B) from the reservoir at 3450-3460 meters through the K-1, and K-1D wells in the K field. The lambda/mu ratio section (A) shows the definition at the reservoir zone with a series of anomalies following the structural pattern. The range of values of lambda/mu in the reservoir for the petrophysical analysis is between 1.2 and 1.3. Anomalies in yellow and red correspond to the range of values in which the gas reservoir is included. The section shows similar values of lambda/mu ratio and it is difficult to discriminate lithology at the reservoir interval because the values are similar. Comparing this lambda/mu ratio map with the post-stack reflectivity map, they are the similar, showing a large anomaly in the K field zone related to distal sand bars. The lambda/mu ratio map shows higher values spatially distributed throughout the reservoir zone

The map (B) on the right was extracted from a seismic horizon on the top of the reservoir. This map is displaying anomalies with values for lambda/mu ratio between 1.45 and 1.6 oriented north-south. These anomalies are suggesting a strong influence of the shales present in the reservoir rock, that masking the possibility to discriminate between fluids. The interpretation of this map is that lambda/mu ratio in the K field is discriminating between sands and shales, showing high-value anomalies related to distal sand bars.

Figures 5.10 and 5.11 show a comparison between post-stack bandlimited impedance and lambda/mu ratio. Figure 5.10 corresponds to the S field area. Lambda/mu ratio is showing some similarities with the bandlimited P_impedance map in north-south oriented negative amplitude anomalies. Figure 5.11

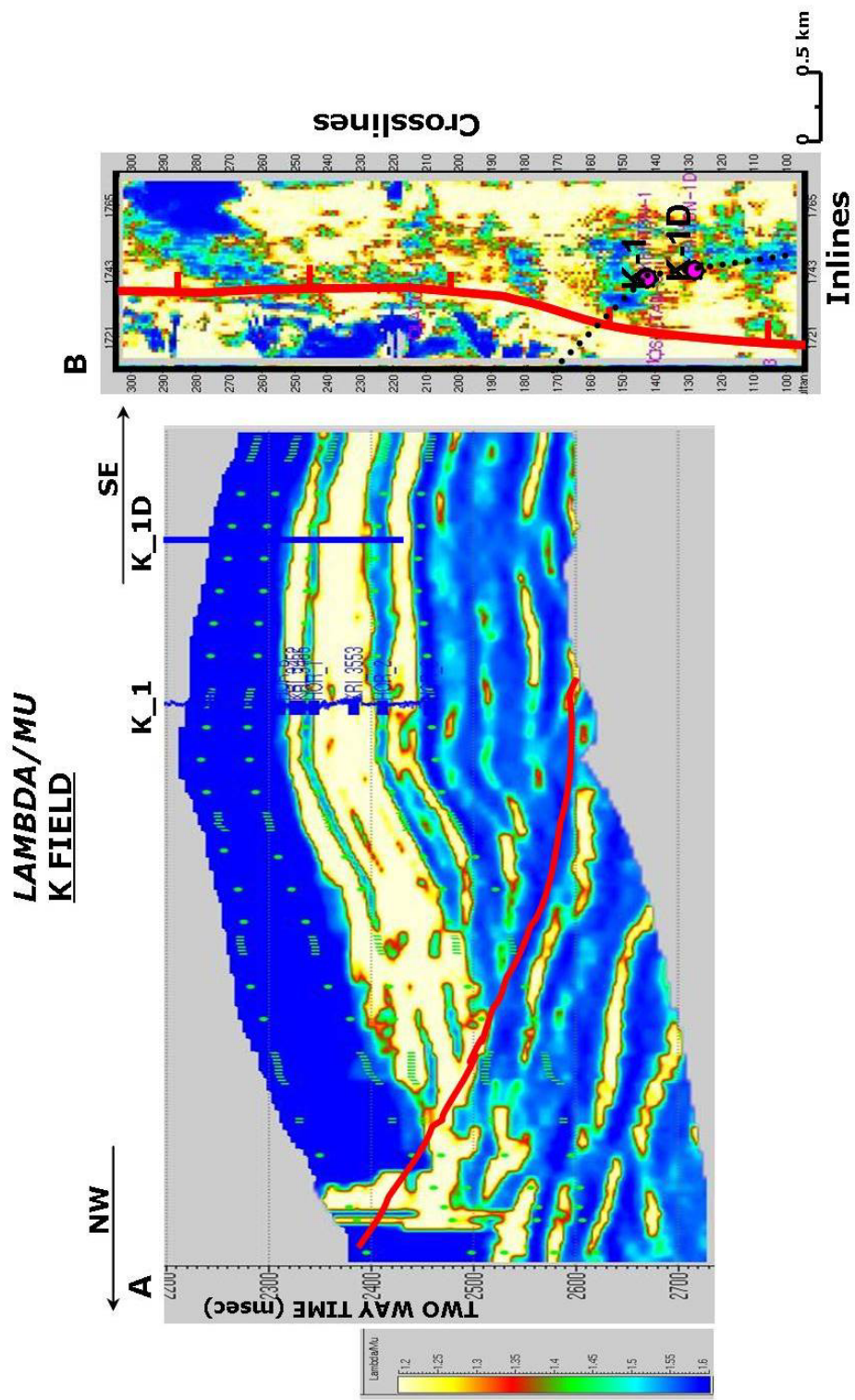


Figure 5.9 Section and map showing the extraction of lambda/mu ratio in the K field.

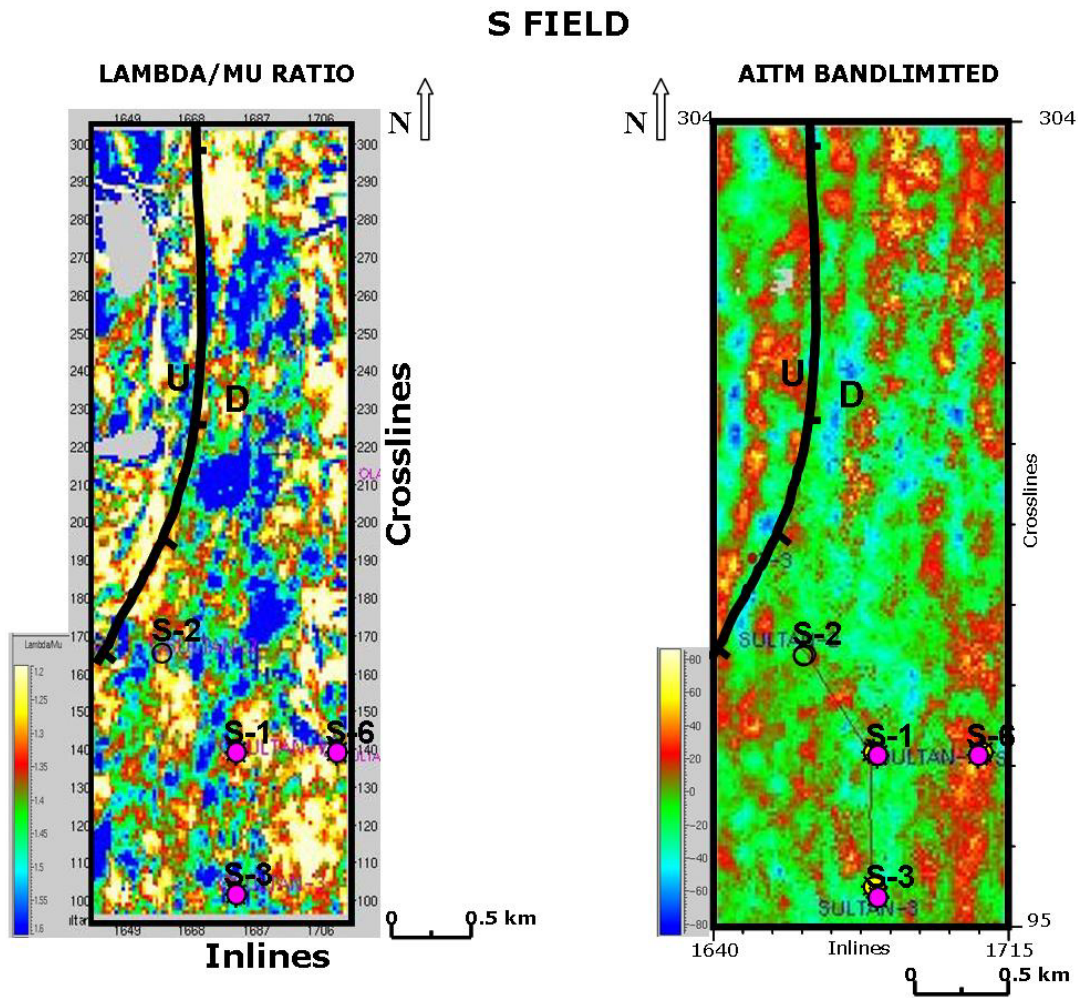


Figure 5.10 Comparison between lambda/mu ratio and bandlimited P_i impedance from post-stack seismic inversion, displaying similarities in the reservoir zone from the S field, indicating north-south amplitude anomalies related to sand bodies.

K FIELD

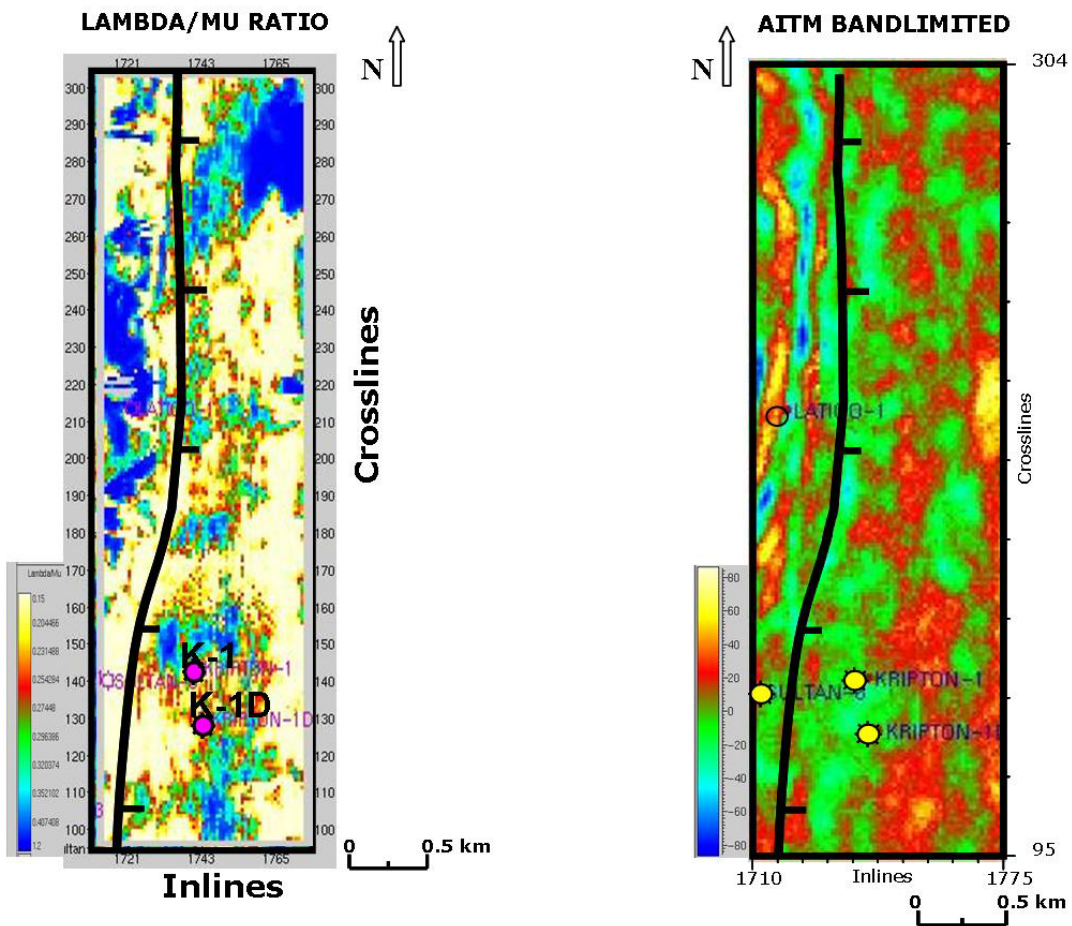


Figure 5.11 Comparison between lambda./mu ratio and bandlimited P_impedance from post-stack seismic inversion showing strike oriented anomalies.

corresponds to the K field area and displays negative amplitude anomalies in the bandlimited P_impedance map correlating to high values in the lambda/mu map.

5.6 CONCLUSIONS

The conclusion of this chapter is that rock quality maps was done with simultaneous inversion methodology using the Lamé's parameters of lambda/mu ratio, lambda*rho, or mu*rho.

The shale content effect is present in crossplots, masking fluid discrimination in the S and K fields.

Rock quality discrimination could be done in S field because the stratigraphic characteristics of clean, and high porosity sandstones helped to define the reservoirs.

K field lithologic characteristics consisting in shaly sandstones, and thin beds was possible to determine rock quality in the reservoir zone.

Comparison between bandlimited P_impedance maps from post-stack inversion and lambda/mu ratio maps shows a good correlation, showing nearly the same strike-oriented amplitude anomalies.

Chapter 6

Discussion of Results

6.1 STRUCTURE

Two structural systems were identified in the Burgos Basin: (1) a Laramide compressional system affecting Upper Paleogene and Mesozoic rocks characterized by reverse faulting, and (2) an extensional system characterized by low-angle normal faulting affecting Paleogene-Recent rocks.

A decoupling (detachment) level separating both structural systems was identified between at the base of Paleogene, where the deepest low-angle normal faults converge. This detachment level is located in the top of Cretaceous in the west portion of the area and at the base of the Jackson Formation in the central-east portion of the Burgos Basin.

Growth faults are curvilinear in map view, are very continuous, and are several kilometers long. The main growth faults bound five structural blocks in which the main reservoirs have been identified. Vicksburg reservoirs in the Burgos Basin are very productive down-dip growth faults, and the reservoirs occur mostly in rollover anticline traps where fault closures play important roles as seals. The Vicksburg Formation is very complex because of sliding on the unstable shales of the Jackson Group.

6.2 STRATIGRAPHY

A stratigraphic framework was delineated by identifying and correlating, flooding surfaces associated with six stratigraphic units, named A to F, within the Vicksburg Formation. These units are constrained to fault-bounded, structurally-defined provinces.

The stratigraphic framework is very similar between South Texas and northern México because the major flooding-surface marker horizons that define the Vicksburg stratigraphy in the Burgos Basin can be correlated north into Texas. The producing intervals in South Texas fields can be identified and assigned to equivalent genetic stratigraphic intervals of the Burgos Basin. The depositional architectures of delta-flank, shoreface, and beach-ridge facies as well as delta mouth bar and distributary channel facies in Vicksburg reservoirs of Texas are also comparable to those in the Burgos Basin.

6.3 PETROPHYSICS

Petrophysical analysis is a fundamental process in any inversion project. A well log data base including porosity, density, gamma ray, and sonic curves is necessary to establish meaningful relationships between rocks and fluids.

Crossplotting was useful in defining petrophysical reservoir intervals of interest and was helpful in discriminating fluids and rocks at key wells.

Lamé's petrophysical parameters, $\lambda \cdot \rho$, $\mu \cdot \rho$, and λ/μ , were used as control points in the pre-stack seismic inversion process.

A well log data base including porosity, density, gamma ray, and sonic curves was necessary for such an analysis and for establishing the relationship between rocks and fluids. The methodology used here consisted of log editing and computing shale volume, effective porosity, water saturation, and elastic properties. Mud filtrate invasion in sonic and density well logs is present because the environmental effects were not totally corrected for.

Crossplotting was useful for defining the petrophysical properties in reservoir intervals of interest and was helpful for discriminating between fluids and rocks at key wells. As a result of this, high P_impedance sandstones were defined with crossplots and low density linked to low values of $\lambda\rho$ were used to discriminate fluid at seismic frequency.

Lamé's petrophysical parameters, $\lambda\rho$ and $\mu\rho$, were analyzed as tool for fluid and lithology discriminators. Clean and good porosity sandstone from S field provided the best way to discriminate between fluid and lithology; shaly sandstone from K reservoir having low porosity does not show a gas effect in fluid-substitution modeling.

However, the shale effect, the mud filtrate invasion, and the presence of gas are the most important issues in this petrophysical analysis and are present in all data.

6.4 POST-STACK INVERSION

Reflectivity modeling is a good tool for stratigraphic analysis at reservoir scale. The stratigraphic model can be used in several ways to improve the reflectivity model.

All of these steps are used to tie well log data to seismic or reflectivity.

The interpretation of flooding surfaces from well log models and reflectivity models provides an additional control on time-depth relationships. The flooding surfaces interpreted in northern México were correlated with those in South Texas because there are similar characteristics in well response and it is easy to recognize them.

Inverted reflectivity modeling helped to improve the vertical resolution and horizontal continuity of seismic events. Amplitude attribute maps extracted from reflectivity at reservoir intervals showed better defined sequences and the reservoir boundaries could be spatially delineated.

Reflectivity amplitude maps were constructed to make the interpretation of the sedimentary model based on the reflectivity. The final attribute maps helped in the development of the gas fields, positioning new wells and better relocating some programmed wells.

In the S field, the facies architecture consists of ridge sand bars deposited along the front and margins of the delta, where the amalgamated ridge sand bars impart first-order strike orientation to the delta framework. Ridge sand bars coarsen upward and are produced by progradation of a marine shoreface.

In K field, the facies architecture is correlated to distal bar deposits composed of interbedded sands, silt, and mud. Upward, the proportion and thickness of sand and silt beds increase. The interbedded sequence grades into hummocky, planar, or low-angle trough cross-stratified sand.

The final attribute maps helped in the development of the gas fields, positioning new wells and better relocating some programmed wells.

6.5 ANGLE-DEPENDENT INVERSION

Rock quality maps were done with simultaneous inversion methodology using the Lamé's parameters like λ/μ ratio, $\lambda \cdot \rho$ or $\mu \cdot \rho$.

Shale content effect is present in crossplots, masking fluid discrimination in S and K fields.

Rock quality discrimination could be done in S field because the stratigraphic characteristics of clean, high-porosity sandstones helped to define the reservoirs.

K field lithologic characteristics consisting in shaly sandstones, and thin beds was possible to determine rock quality in the reservoir zone.

Comparison between bandlimited $P_{\text{impedance}}$ maps from post-stack inversion and λ/μ ratio maps shows a good correlation, showing slightly the same strike-oriented amplitude anomalies.

Appendix A

Well Database

WELL	LOG START DEPTH (METERS)	STOP DEPTH (METERS)	STEP (METERS)	UWI	ELEV. (METERS)	ELEV TYPE
A-1	0.0764	2706.8523	0.1524	1010003880	88.52	KB
BAZ-1	20.1170	2456.2305	0.1524	1010003881	58.55	KB
BER-1	25.1524	2685.1472	0.1524	1010000148	71.30	KB
BER-2	492.0000	2500.9400	0.1524	1010000149	65.00	KB
BER-3	295.0000	2100.0291	0.1524	1010000150	82.00	KB
CA-1	398.2500	2799.9260	0.1524	1010000217	43.00	KB
CA-3	25.0000	4009.9631	0.1524	1010000218	36.30	KB
CA-3D	792.0000	2707.1250	0.1250	1010000219	37.00	KB
CA-3T	1395.0000	2310.0000	0.2500	1010000220	37.10	KB
CA-5	302.2500	2553.0000	0.1250	1010000221	38.00	KB
CA-7	20.2618	2530.9041	0.1524	1010000222	36.40	KB
CA_OR-1	505.0000	2404.7500	0.2500	1010000323	42.00	KB
CA_OR-2	975.0000	2700.0000	0.2500	1010000324	42.00	KB
CA_OR-3	500.0000	2600.0757	0.1524	1010000325	44.00	KB
CHI-1	155.0000	2499.9834	0.1524	1010000257	59.00	KB
DRA-1	20.0203	3874.5188	0.1000	1010001430	77.32	KB
EC-1	17.9834	2799.8931	0.1524	1010001115	67.00	KB
EM-1	5.0000	2010.1266	0.1524	1010003785	82.01	KB
ES-1	25.0549	3192.3047	0.1250	1010000600	59.00	KB
GAL-1	25.5274	2109.9021	0.1250	6699856	76.05	KB
GALI-1	29.1084	2514.1421	0.1524	448890765	64.13	KB
GAR-1	144.2380	2509.4827	0.1524	1010000687	85.00	KB
IND-1	3.5049	2128.8730	0.1524	123450008	60.21	KB
K-1	12.0000	3707.5459	0.1524	1010003882	107.50	KB
K-1D	18.0000	3517.5459	0.1524	1010003882	95.50	KB
LAT-1	50.0000	2999.8601	0.1524	1010000811	85.00	KB
L-101	25.0000	1901.3525	0.1524	1010000769	67.00	KB
L-102	230.0000	1985.0000	0.2500	1010000770	66.00	KB
L-107	260.0000	2140.4673	0.1524	1010000771	71.00	KB
L-115	35.0000	2905.7500	0.2500	1010000773	47.00	KB
L-116	25.0000	1950.0000	0.2500	1010000774	87.00	KB
L-117	250.0000	1900.0000	0.2500	1010000775	96.00	KB
L-123	1375.0000	1994.5000	0.1250	1010000776	64.00	KB
L-128	50.0000	2495.0000	0.2500	1010000777	74.00	KB
L-138	25.0000	1900.0000	0.2500	1010000779	84.00	KB
L-141	300.0000	1900.0000	0.2500	1010000780	97.00	KB

L-160	275.0000	1800.0000	0.2500	1010000781	78.00	KB
L-161	25.0000	1850.0000	0.2500	1010000782	83.97	KB
L-162	25.0000	1600.0000	0.2500	1010000783	88.00	KB
L-164	25.0000	2609.8616	0.1524	1010000784	50.00	KB
L-170	271.5000	1800.0000	0.1250	1010000786	56.00	KB
L-171	280.0000	1575.0000	0.2500	1010000787	43.00	KB
L-173	300.0000	1800.0000	0.2500	1010000788	58.00	KB
L-174	275.0000	1800.0000	0.2500	1010000789	59.00	KB
L-175	300.0000	1590.0000	0.2500	1010000790	57.00	KB
L-176	250.3048	1589.9008	0.3048	1010000791	55.00	KB
L-185	275.0000	2149.9810	0.1524	1010000792	48.20	KB
L-186	401.5240	2500.0720	0.3048	1010000793	73.00	KB
L-193	398.7500	2400.0703	0.1524	1010000794	53.00	KB
L-193D	400.0000	2000.0000	0.2500	1010000795	53.00	KB
L-195	400.0000	2400.8635	0.1524	1010000796	57.00	KB
L-200	400.0000	2400.0000	0.2500	1010000797	76.00	KB
L-203	25.0000	2500.0000	0.2500	1010000798	96.10	KB
L-206A	25.0952	2599.8984	0.1524	1010000799	43.60	KB
L-208	182.8804	2400.4570	0.0762	1010000800	64.00	KB
L-212	400.0000	2510.0000	0.2500	1010000801	102.00	KB
L-214	275.0000	1800.0000	0.2500	1010000802	93.00	KB
L-215	250.0000	2000.0000	0.2500	1010000803	92.00	KB
L-217	275.0000	1800.0000	0.2500	1010000804	74.00	KB
L-219	275.0000	1850.0000	0.2500	1010000805	80.50	KB
L-224	250.0000	1449.9976	0.3048	1010000806	85.00	KB
L-225	275.0000	1600.0000	0.2500	1010000807	113.00	KB
L-226A	275.0000	1575.0000	0.2500	1010000808	98.00	KB
MAC-1	0.0640	3031.9634	0.1000	1010000875	73.80	KB
M-1	65.2273	1825.7175	0.0381	1010000831	40.00	KB
M-2	92.9642	1852.9591	0.0762	1010000832	42.00	KB
M-3	182.8804	2449.9602	0.0762	1010000833	45.00	KB
M-4	185.9284	537.8969	0.0762	1010000834	45.00	KB
M-8	4.8768	1642.9515	0.0762	1010000835	45.00	KB
M-9	4.8768	559.3091	0.0381	1010000836	43.00	KB
M-10	306.3246	1947.9808	0.0762	1010000837	45.00	KB
M-11	9.4480	2068.9866	0.0762	1010000838	43.00	KB
M-13	15.2400	3004.4958	0.0762	1010000839	40.00	KB
M-14	182.8804	2631.5723	0.0762	1010000840	39.00	KB
M-15	182.8804	2274.9556	0.0762	1010000841	39.00	KB
M-16	274.3206	1909.1567	0.0762	1010000842	40.00	KB
M-17	15.2400	502.8448	0.0762	1010000843	41.00	KB
M-18	91.4633	579.8554	0.0762	1010000844	42.00	KB

M-19	91.4402	578.9688	0.0762	1010000845	36.00	KB
M-20	91.4402	672.0092	0.0762	1010000846	50.00	KB
M-22	91.4402	464.8209	0.0762	1010000848	36.00	KB
M-23	496.5000	2250.0718	0.1524	1010000849	41.00	KB
M-24	500.0000	2205.0000	0.2500	1010000850	43.00	KB
M-25	300.0309	1524.9598	0.0465	1010000851	41.00	KB
M-26	300.0000	1525.0000	0.2500	1010000852	38.00	KB
M-27	325.0000	1325.0000	0.2500	1010000853	40.00	KB
M-28	300.0000	1525.0000	0.2500	1010000854	39.00	KB
M-29	300.0000	1515.0000	0.2500	1010000855	38.00	KB
M-30	300.0000	1525.0000	0.2500	1010000856	39.00	KB
M-31	300.0000	1525.0000	0.2500	1010000857	39.00	KB
M-32	300.0000	1510.0000	0.2500	1010000858	36.00	KB
M-33	300.0000	1525.0000	0.2500	1010000859	41.00	KB
M-34	91.4402	464.8209	0.0762	1010000860	41.00	KB
M-35	300.0000	1525.0000	0.2500	1010000861	40.00	KB
M-36	300.0000	1525.0000	0.2500	1010000862	40.00	KB
M-37	300.0000	1525.0000	0.2500	1010000863	41.00	KB
M-38	305.0000	1525.0000	0.2500	1010000864	42.00	KB
M-39	300.0000	1520.0000	0.2500	1010000865	40.00	KB
M-40	300.0000	1520.0000	0.2500	1010000866	39.00	KB
M-41	305.0000	1510.0000	0.2500	1010000867	42.00	KB
M-42	300.0000	1525.0000	0.2500	1010000868	41.00	KB
M-43	800.0000	2705.0000	0.2500	1010000869	41.00	KB
M-45	293.2494	3399.9744	0.1524	1010000870	45.00	KB
M-46	6.2484	2104.9487	0.1524	1010000871	41.00	KB
M-47	141.2748	2101.2908	0.1524	1010000872	41.00	KB
M-62	22.6960	2098.4956	0.1000	1010003917	41.00	KB
M-63	17.6510	2139.4009	0.1250	1010003056	39.00	KB
M-1001	34.5187	3437.4651	0.0762	1010002817	41.00	KB
M-2001	300.0000	2494.4880	0.1524	1010002859	46.90	KB
PAS-14	300.0000	2550.0337	0.3048	1010001237	85.20	KB
RIB-1	25.0000	4499.9282	0.1524	1010001271	69.00	KB
SAN JAC-1	24.5000	2499.9380	0.1524	1010001585	62.00	KB
S-1	17.6361	3367.8831	0.1250	1010003672	115.00	KB
S-2	10.3524	3125.7129	0.1524	1010004122	100.00	KB
S-3	15.3524	3005.7129	0.1524	1010004162	85.00	KB
S-102	129.2350	1907.2858	0.1524	1010000560	82.00	KB

Table A.1 Data base of the wells used on this study.

Appendix B

Time Depth Tables and Velocity Graphs

A-1				
Depth (m)	Two-way time (ms)	One-way time (ms)	Average Velocity m/s	Interval Velocity m/s
0.00	0.00	0.0	0	0
7.40	7.06	3.5	2096.32	2096.32
107.40	146.40	73.2	1467.21	1435.34
207.50	237.80	118.9	1745.16	2190.37
307.40	301.00	150.5	2042.52	3161.39
407.50	372.80	186.4	2186.16	2788.30
507.40	453.00	226.5	2240.18	2491.27
607.50	519.80	259.9	2337.44	2997.01
707.50	596.60	298.3	2371.77	2604.17
807.50	682.60	341.3	2365.95	2325.58
907.50	737.00	368.5	2462.69	3676.47
1007.50	792.80	396.4	2541.62	3584.23
1107.50	850.40	425.2	2604.66	3472.22
1207.50	926.40	463.2	2606.87	2631.58
1307.50	987.00	493.5	2649.44	3300.33
1407.50	1045.00	522.5	2693.78	3448.28
1507.50	1103.00	551.5	2733.45	3448.28
1607.50	1166.00	583.0	2757.29	3174.60
1707.40	1223.00	611.5	2792.15	3505.26
1807.50	1293.00	646.5	2795.82	2860.00
1907.50	1377.00	688.5	2770.52	2380.95
2007.40	1454.00	727.0	2761.21	2594.81
2107.50	1529.00	764.5	2756.70	2669.33
2207.50	1604.00	802.0	2752.49	2666.67
2307.40	1674.00	837.0	2756.75	2854.29
2407.50	1746.00	873.0	2757.73	2780.56
2507.50	1819.00	909.5	2757.01	2739.73
2607.50	1898.00	949.0	2747.63	2531.65

Table B.1 Velocity data from the A-1 well.

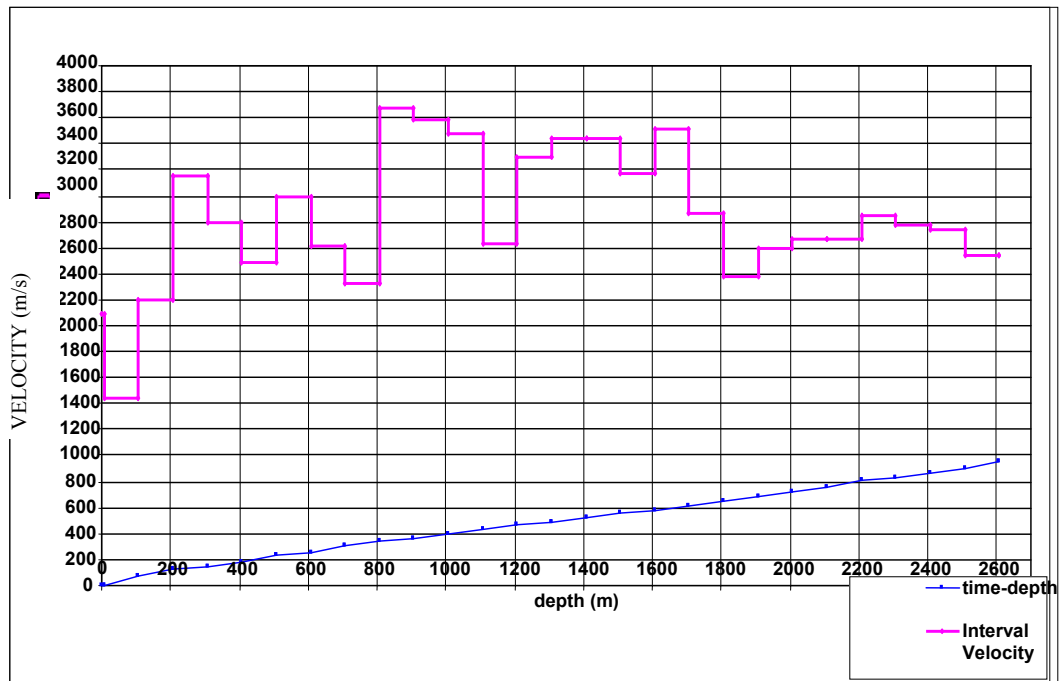


Figure B.1 Time-depth graph and interval velocities from the A-1 well

Baz-1				
Depth (m)	Two-way time (ms)	One way-time (ms)	Average Velocity m/s	Interval Velocity m/s
30	28.47	14.2	2107.48	2107.48
90	85.4	42.7	2107.73	2107.85
150	143.37	71.7	2092.49	2070.04
210	199.61	99.8	2104.10	2133.71
270	254.13	127.1	2124.90	2201.03
330	304.81	152.4	2165.28	2367.80
390	356.23	178.1	2189.60	2333.72
420	381	190.5	2204.72	2422.29
480	431.2	215.6	2226.35	2390.44
540	476.5	238.3	2266.53	2649.01
600	522.93	261.5	2294.76	2584.54
660	567.66	283.8	2325.34	2682.76
720	609.41	304.7	2362.94	2874.25
780	655.31	327.7	2380.55	2614.38
840	699.33	349.7	2402.30	2726.03
870	720.99	360.5	2413.35	2770.08
930	762.46	381.2	2439.47	2893.66
990	805.02	402.5	2459.57	2819.55
1050	846.3	423.2	2481.39	2906.98
1110	889.46	444.7	2495.90	2780.35
1170	932.15	466.1	2510.33	2810.96
1230	977.15	488.6	2517.53	2666.67
1290	1015.08	507.5	2541.67	3163.72
1350	1051.43	525.7	2567.93	3301.24
1410	1085.76	542.9	2597.26	3495.48
1470	1120.18	560.1	2624.58	3486.35
1530	1153	576.5	2653.95	3656.31
1590	1186.27	593.1	2680.67	3606.85
1650	1220.44	610.2	2703.94	3511.85
1710	1255.3	627.7	2724.45	3442.34
1770	1291.99	646.0	2739.96	3270.65
1830	1325.18	662.6	2761.89	3615.55
1890	1358.44	679.2	2782.60	3607.94
1950	1389.14	694.6	2807.49	3908.79
2010	1420.38	710.2	2830.23	3841.23

Table B.2 Velocity data from the Baz-1 well

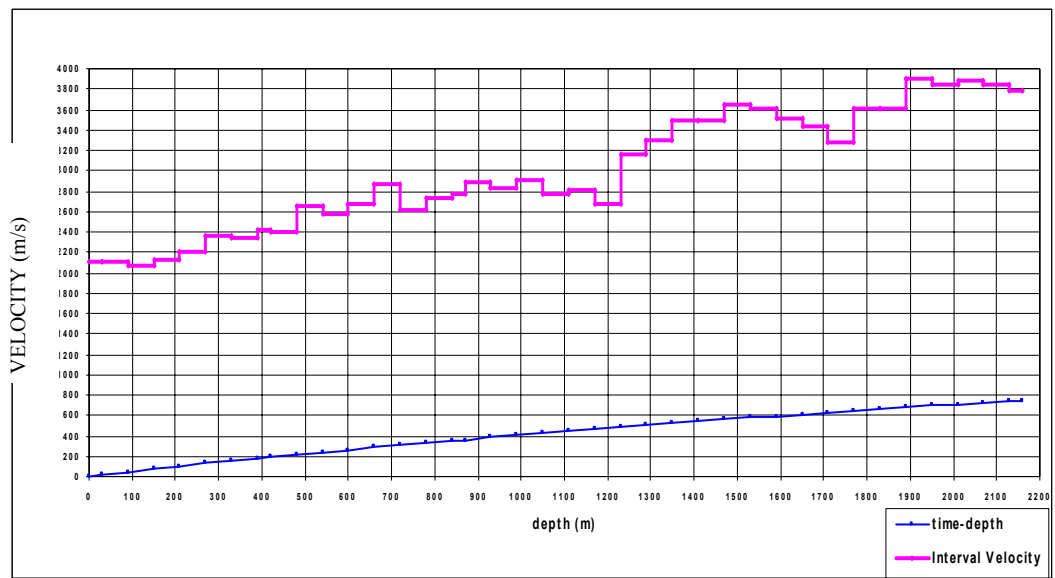


Figure B.2 Time-depth and interval velocities graph from the Baz-1 well.

Dra-1				
Depth (m)	Two-way time (ms)	One-way time (ms)	Average Velocity m/s	Interval Velocity m/s
-112.75	0	0.0	0	0
37.25	150.4	75.2	495.35	1994.68
209.95	304.1	152.1	1380.80	2247.23
409.95	468.5	234.3	1750.05	2433.09
609.95	618.9	309.5	1971.08	2659.57
809.95	774.9	387.5	2090.46	2564.10
1009.95	937.8	468.9	2153.87	2455.49
1109.85	1025.9	513.0	2163.66	2267.88
1209.75	1113.3	556.7	2173.27	2286.04
1309.05	1196.1	598.1	2188.86	2398.55
1406.55	1277.2	638.6	2202.55	2404.44
1500.25	1353.1	676.6	2217.50	2469.04
1588.35	1423.9	712.0	2230.99	2488.70
1672.05	1474.4	737.2	2268.11	3314.85
1754.55	1526.2	763.1	2299.24	3185.33
1835.85	1581.1	790.6	2322.24	2961.75
1916.15	1630.1	815.1	2350.96	3277.55
1997.55	1686.7	843.4	2368.59	2876.33
2079.45	1743.5	871.8	2385.37	2883.80
2162.75	1804.9	902.5	2396.53	2713.36
2248.45	1877	938.5	2395.79	2377.25
2333.55	1954	977.0	2388.49	2210.39
2416.45	2029.4	1014.7	2381.44	2198.94
2499.65	2103.4	1051.7	2376.77	2248.65
2581.75	2178.6	1089.3	2370.10	2183.51
2663.95	2248.1	1124.1	2369.96	2365.47
2745.75	2300.6	1150.3	2386.99	3116.19
2826.95	2355.6	1177.8	2400.20	2952.73
2907.85	2417.7	1208.9	2405.47	2605.48
2988.75	2478.6	1239.3	2411.64	2656.81
3070.45	2539.7	1269.9	2417.96	2674.30
3236.25	2627.2	1313.6	2463.65	3789.71

Table B.3 Velocity data from the Dra-1 well

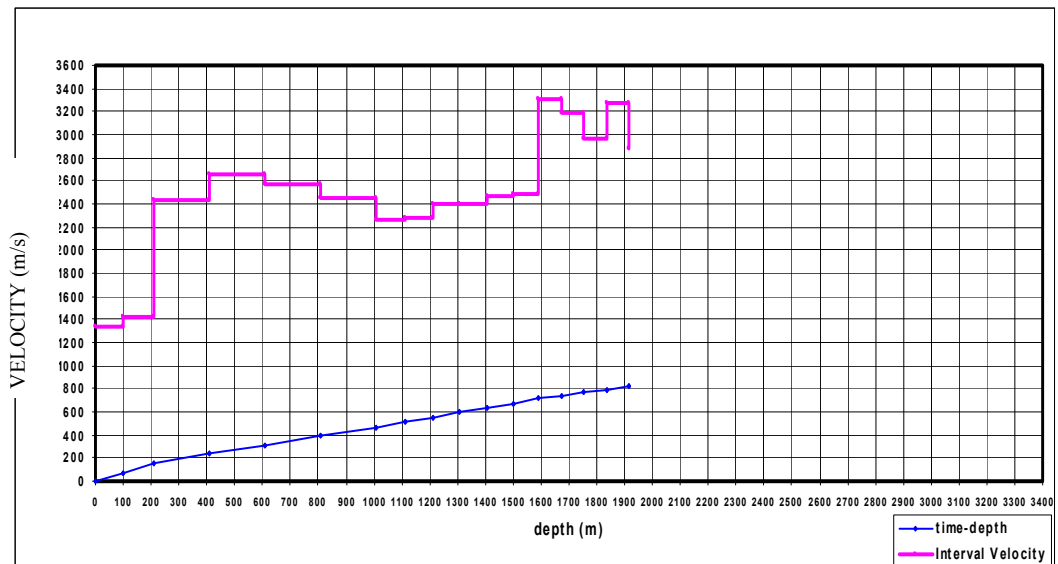


Figure B.3 Time-depth and interval velocities graph from the Dra-1 well.

Ec-1				
Depth (m)	Two-way time (ms)	One-way time (ms)	Average Velocity m/s	Interval Velocity m/s
0	0	0.0	0	0
116	100	50.0	2320.00	2320.00
233.3	200	100.0	2333.00	2346.00
347.7	300	150.0	2318.00	2288.00
466.4	400	200.0	2332.00	2374.00
593.5	500	250.0	2374.00	2542.00
727.3	600	300.0	2424.33	2676.00
867.4	700	350.0	2478.29	2802.00
1008.5	800	400.0	2521.25	2822.00
1156.4	900	450.0	2569.78	2958.00
1299	1000	500.0	2598.00	2852.00
1449	1100	550.0	2634.55	3000.00
1609.7	1200	600.0	2682.83	3214.00
1787.9	1300	650.0	2750.62	3564.00
1961	1400	700.0	2801.43	3462.00
2119.6	1500	750.0	2826.13	3172.00
2273.2	1600	800.0	2841.50	3072.00
2415.7	1700	850.0	2842.00	2850.00
2555.8	1800	900.0	2839.78	2802.00
2698.2	1900	950.0	2840.21	2848.00
2712.5	1910	955.0	2840.31	2860.00

Table B.4 Velocity data from the Ec-1 well.

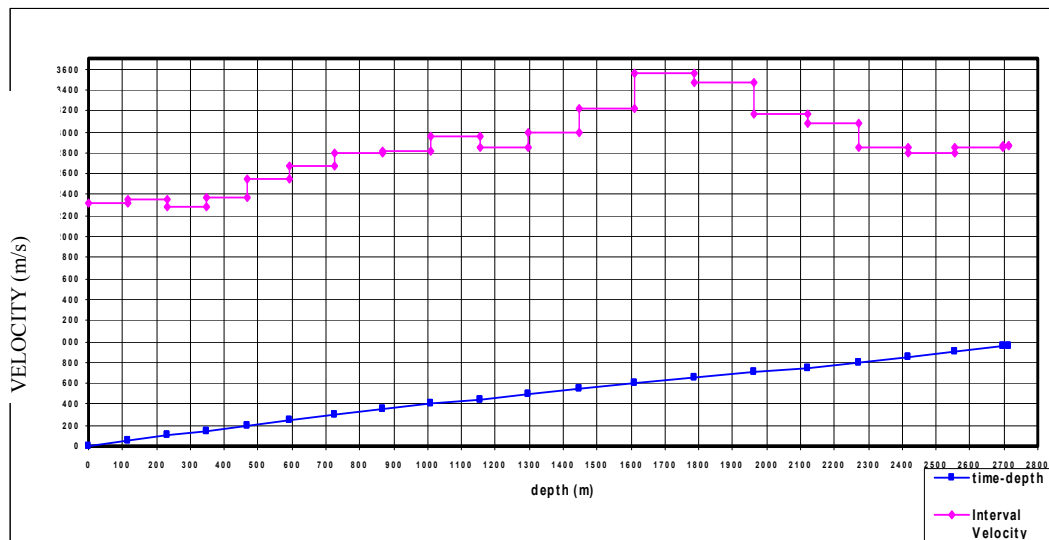


Figure B.4 Time-depth and interval velocities data from the Ec-1 well.

Em-1				
Depth (m)	Two- way time (ms)	One- way time (ms)	Average Velocity m/s	Interval Velocity m/s
0	0	0.0	0	0
121.9	100	50.0	2438.00	2438.00
217	200	100.0	2170.00	1902.00
317.5	300	150.0	2116.67	2010.00
446	400	200.0	2230.00	2570.00
591	500	250.0	2364.00	2900.00
742.1	600	300.0	2473.67	3022.00
898.4	700	350.0	2566.86	3126.00
1046.7	800	400.0	2616.75	2966.00
1203.9	900	450.0	2675.33	3144.00
1373.1	1000	500.0	2746.20	3384.00
1540.6	1100	550.0	2801.09	3350.00
1706.2	1200	600.0	2843.67	3312.00
1866.2	1300	650.0	2871.08	3200.00
1998.9	1380	690.0	2896.96	3317.50

Table B.5 Velocity data from the Em-1 well

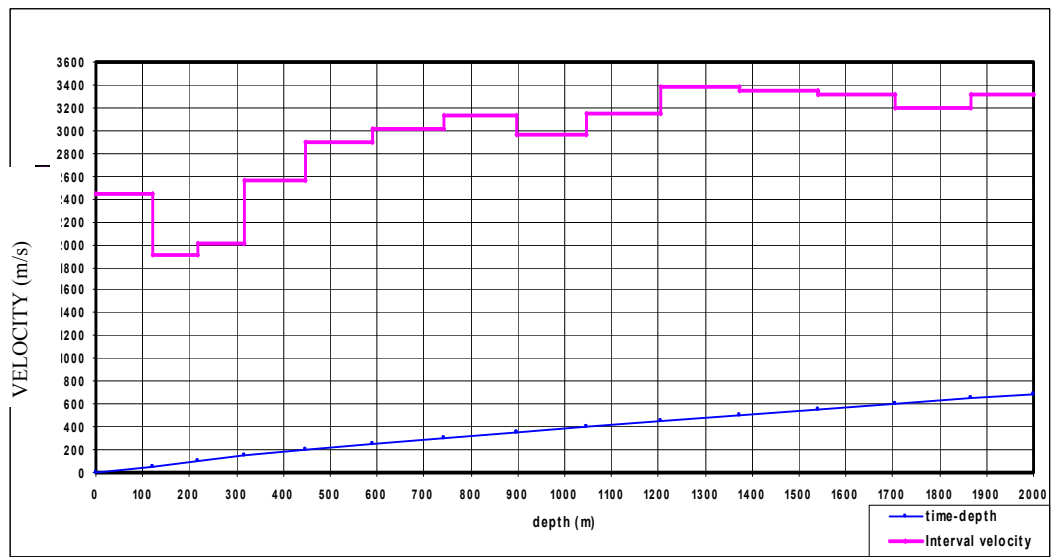


Figure B.5 Time-depth and interval velocities graph from the Em-1 well.

Gal-1				
Depth (m)	Two- way time (ms)	One- way time (ms)	Average Velocity m/s	Interval Velocity m/s
0	0	0.0	0	0
90	100	50.0	1800.00	1800.00
191.5	200	100.0	1915.00	2030.00
303.7	300	150.0	2024.67	2244.00
428.9	400	200.0	2144.50	2504.00
557.9	500	250.0	2231.60	2580.00
689.5	600	300.0	2298.33	2632.00
828.4	700	350.0	2366.86	2778.00
970.6	800	400.0	2426.50	2844.00
1122.9	900	450.0	2495.33	3046.00
1285.5	1000	500.0	2571.00	3252.00
1451.4	1100	550.0	2638.91	3318.00
1621.1	1200	600.0	2701.83	3394.00
1777.9	1300	650.0	2735.23	3136.00
1927.7	1400	700.0	2753.86	2996.00
2000.3	1450	725.0	2759.03	2904.00

Table B.6 Velocity data from the Gal-1 well

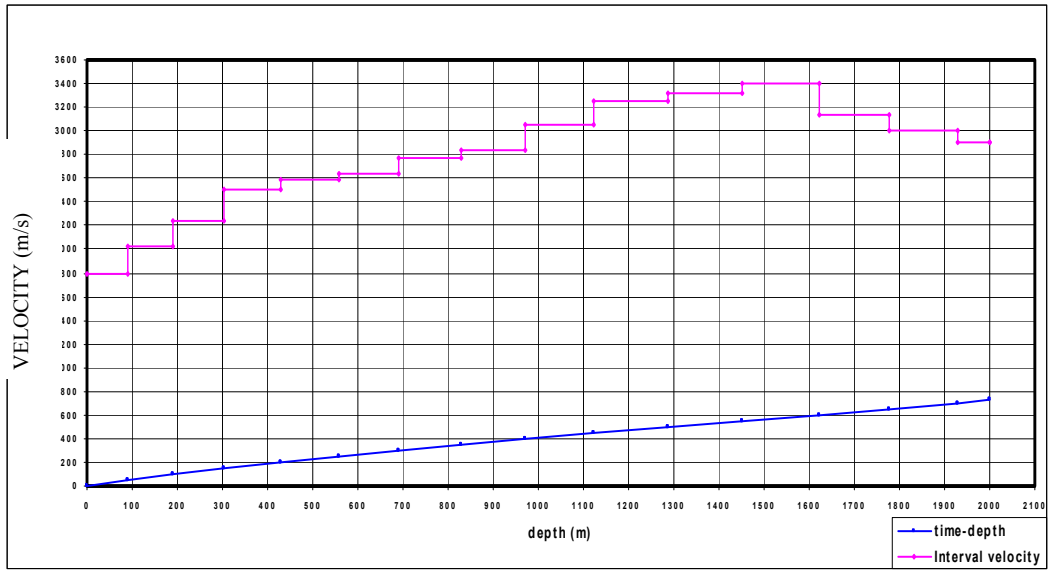


Figure B.6 Time-depth and interval velocities graph from the Gal-1 well.

Gali-1				
Depth (m)	Two-way time (ms)	One-way time (ms)	Average Velocity m/s	Interval Velocity m/s
0	0	0.0	0	0
93.8	100	50.0	1876.00	1876.00
196.7	200	100.0	1967.00	2058.00
308.1	300	150.0	2054.00	2228.00
428.4	400	200.0	2142.00	2406.00
557.6	500	250.0	2230.40	2584.00
690.3	600	300.0	2301.00	2654.00
827.1	700	350.0	2363.14	2736.00
967.1	800	400.0	2417.75	2800.00
1110.3	900	450.0	2467.33	2864.00
1270	1000	500.0	2540.00	3194.00
1442.7	1100	550.0	2623.09	3454.00
1612.5	1200	600.0	2687.50	3396.00
1787.1	1300	650.0	2749.38	3492.00
1972.9	1400	700.0	2818.43	3716.00
2142.1	1500	750.0	2856.13	3384.00
2312.2	1600	800.0	2890.25	3402.00
2439.9	1670	835.0	2922.04	3648.57

Table B.7 Velocity data from the Gali-1 well

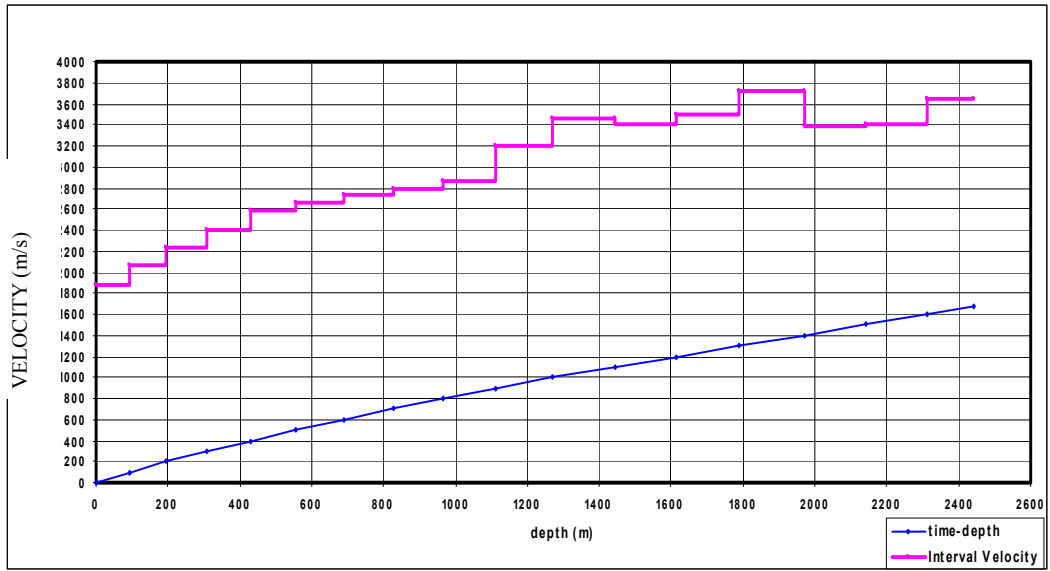


Figure B.7 Time-depth and interval velocities from the Gali-1 well.

Ind-1				
Depth (m)	Two-way time (ms)	One-way time (ms)	Average Velocity m/s	Interval Velocity m/s
0	0	0.0	0	0
100	108.9	54.5	1836.55	1836.55
200	217.7	108.9	1837.39	1838.24
300	321.2	160.6	1868.00	1932.37
400	403.1	201.6	1984.62	2442.00
500	485.1	242.6	2061.43	2439.02
600	565.4	282.7	2122.39	2490.66
700	639.6	319.8	2188.87	2695.42
800	713.7	356.9	2241.84	2699.06
900	787.9	394.0	2284.55	2695.42
1000	861.2	430.6	2322.34	2728.51
1100	934.6	467.3	2353.95	2724.80
1200	1005	502.5	2388.06	2840.91
1300	1063.7	531.9	2444.30	3407.16
1400	1122.4	561.2	2494.65	3407.16
1500	1182	591.0	2538.07	3355.70
1560	1217.3	608.7	2563.05	3399.43
1600	1240.1	620.1	2580.44	3508.77
1660	1274.7	637.4	2604.53	3468.21
1700	1295.3	647.7	2624.87	3883.50
1760	1328.6	664.3	2649.41	3603.60
1800	1353.5	676.8	2659.77	3212.85
1860	1383.4	691.7	2689.03	4013.38
1900	1403	701.5	2708.48	4081.63
1960	1433.1	716.6	2735.33	3986.71
1980	1444.6	722.3	2741.24	3478.26
1994	1450.7	725.4	2749.02	4590.16

Table B.8 Velocity data from the Ind-1 well

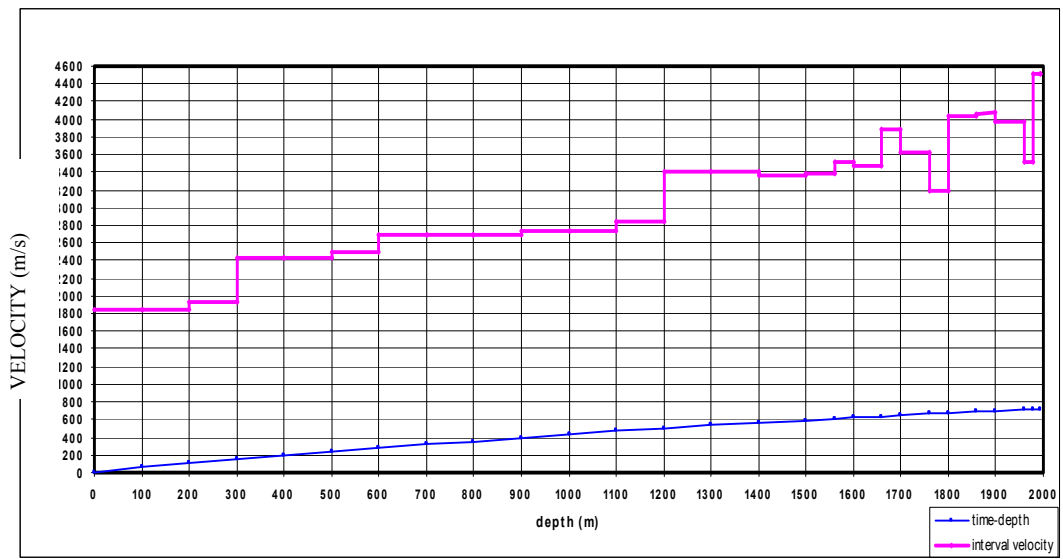


Figure B.8 Time-depth and interval velocities graph from the Ind-1 well.

K-1				
Depth (m)	Two- way time (ms)	One- way time (ms)	Average Velocity m/s	Interval Velocity m/s
0	0	0.0	0	0
100	95.1	47.6	2103.05	2103.05
200	188.4	94.2	2123.14	2143.62
400	369.8	184.9	2163.33	2293.58
500	451.1	225.6	2216.80	2460.02
600	532.3	266.2	2254.37	2463.05
700	613.5	306.8	2281.99	2463.05
800	690.6	345.3	2316.83	2594.03
900	762.8	381.4	2359.73	2770.08
1000	832.9	416.5	2401.25	2853.07
1100	903	451.5	2436.32	2853.07
1200	970	485.0	2474.23	2985.07
1300	1033.6	516.8	2515.48	3144.65
1400	1095.7	547.9	2555.44	3220.61
1500	1156.1	578.1	2594.93	3311.26
1700	1273.8	636.9	2669.18	3401.36
1800	1330.3	665.2	2706.16	3539.82
1900	1389.3	694.7	2735.19	3389.83
2000	1444.3	722.2	2769.51	3636.36
2200	1566	783.0	2809.71	3236.25
2400	1684	842.0	2850.36	3521.13
2500	1738.3	869.2	2876.37	3683.24
2600	1790.3	895.2	2904.54	3846.15
2700	1857.9	929.0	2906.51	2958.58
2800	1930.9	965.5	2900.20	2739.73
2900	2004	1002.0	2894.21	2735.98
3000	2075.2	1037.6	2891.29	2808.99
3100	2147.3	1073.7	2887.35	2773.93
3200	2217.4	1108.7	2886.26	2853.07
3300	2291.7	1145.9	2879.96	2691.79
3400	2361.7	1180.9	2879.28	2857.14
3500	2425.4	1212.7	2886.12	3139.72
3600	2495.3	1247.7	2885.42	2861.23
3640	2517.8	1258.9	2891.41	3555.56

Table B.9 Velocity data from the Ind-1 well

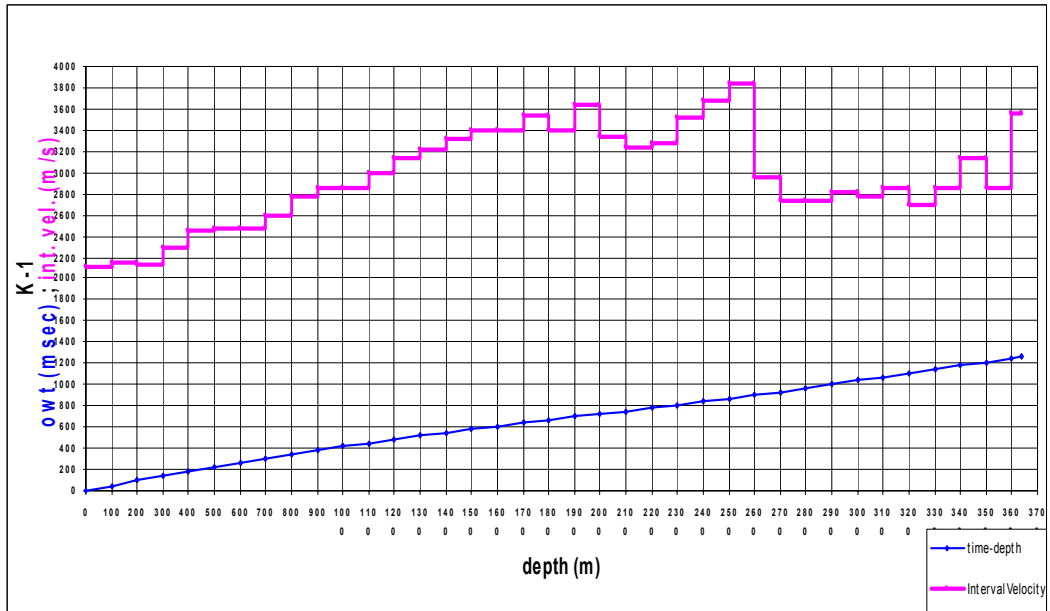


Figure B.9 Time-depth and interval velocities graph from the K-1 well.

Mac-1				
Depth (m)	Two-way time (ms)	One-way time (ms)	Average Velocity m/s	Interval Velocity m/s
0	0	0.0	0	0
226	278	139.0	1625.90	1625.90
526	510	255.0	2062.75	2586.21
726	650	325.0	2233.85	2857.14
1026	858	429.0	2391.61	2884.62
1226	992	496.0	2471.77	2985.07
1501	1178	589.0	2548.39	2956.99
1751	1316	658.0	2661.09	3623.19
2001	1472	736.0	2718.75	3205.13
2251	1628	814.0	2765.36	3205.13
2501	1782	891.0	2806.96	3246.75
2751	1924	962.0	2859.67	3521.13
2926	2016	1008.0	2902.78	3804.35

Table B.10 Velocity data from the Mac-1 well

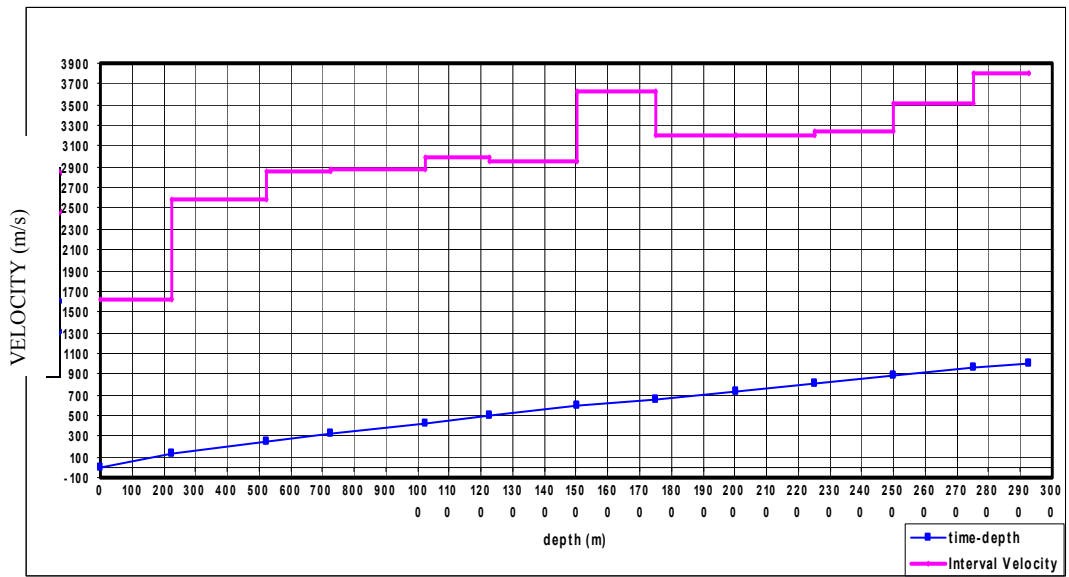


Figure B.10 Time-depth and interval velocities graph from the Mac-1 well.

M-1001				
Depth (m)	Two-way time (ms)	One-way time (ms)	Average Velocity m/s	Interval Velocity m/s
0	0.0	0.0	0	0
200	208.5	104.3	1918.47	1918.47
400	385.0	192.5	2077.92	2266.29
600	539.0	269.5	2226.35	2597.40
800	687.0	343.5	2328.97	2702.70
1000	833.0	416.5	2400.96	2739.73
1200	972.0	486.0	2469.14	2877.70
1450	1118.0	559.0	2593.92	3424.66
1650	1236.0	618.0	2669.90	3389.83
1850	1366.0	683.0	2708.64	3076.92
2060	1511.0	755.5	2726.67	2896.55
2270	1648.0	824.0	2754.85	3065.69
2500	1795.0	897.5	2785.52	3129.25
2715	1926.0	963.0	2819.31	3282.44
2930	2059.0	1029.5	2846.04	3233.08
3140	2201.0	1100.5	2853.25	2957.75
3300	2330.0	1165.0	2832.62	2480.62

Table B.11 Velocity data from the M-1001 well

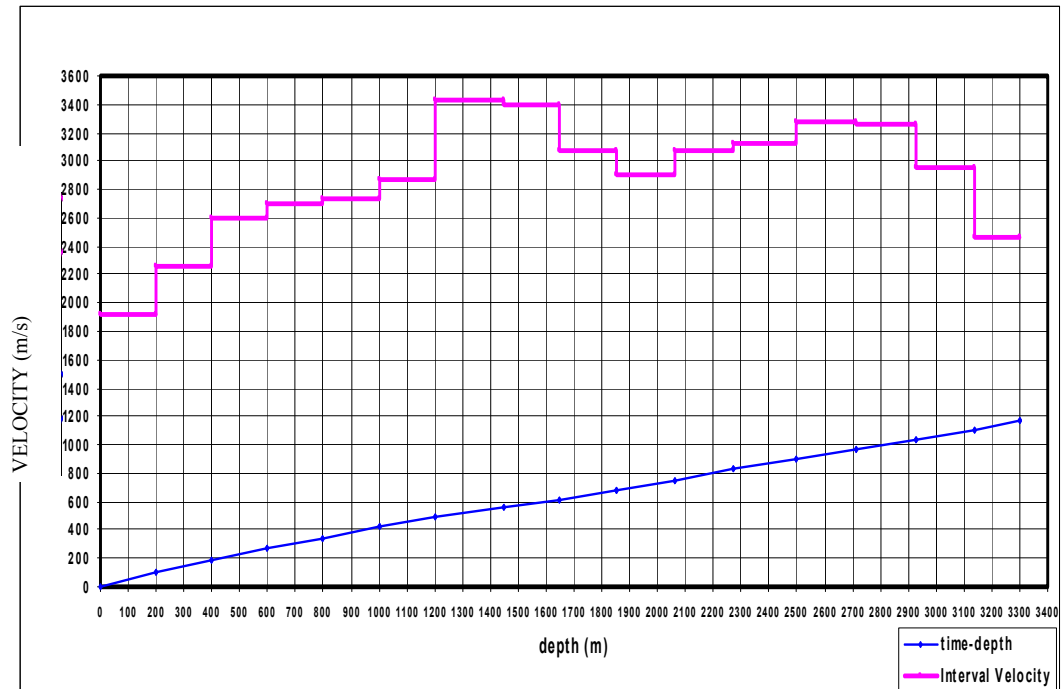


Figure B.11 Time-depth and interval velocities from the M-1001 well.

S-1				
Depth (m)	Two- way time (ms)	One- way time (ms)	Average Velocity m/s	Interval Velocity m/s
0	0	0.0	0	2158.27
150	139	69.5	2158.27	2158.27
255	232	116.0	2198.28	2258.06
355	314	157.0	2261.15	2439.02
465	397	198.5	2342.57	2650.60
560	471	235.5	2377.92	2567.57
660	540	270.0	2444.44	2898.55
760	609	304.5	2495.89	2898.55
860	678	339.0	2536.87	2898.55
955	742	371.0	2574.12	2968.75
1065	810	405.0	2629.63	3235.29
1175	882	441.0	2664.40	3055.56
1280	950	475.0	2694.74	3088.24
1385	1015	507.5	2729.06	3230.77
1485	1074	537.0	2765.36	3389.83
1590	1133	566.5	2806.71	3559.32
1690	1188	594.0	2845.12	3636.36
1795	1248	624.0	2876.60	3500.00
1890	1304	652.0	2898.77	3392.86
1990	1364	682.0	2917.89	3333.33
2095	1422	711.0	2946.55	3620.69
2200	1478	739.0	2977.00	3750.00
2290	1540	770.0	2974.03	2903.23
2390	1614	807.0	2961.59	2702.70
2490	1692	846.0	2943.26	2564.10
2590	1772	886.0	2923.25	2500.00
2690	1850	925.0	2908.11	2564.10
2800	1926	963.0	2907.58	2894.74
3000	2080	1040.0	2884.62	2597.40

Table B.12 Velocity data from the S-1 well

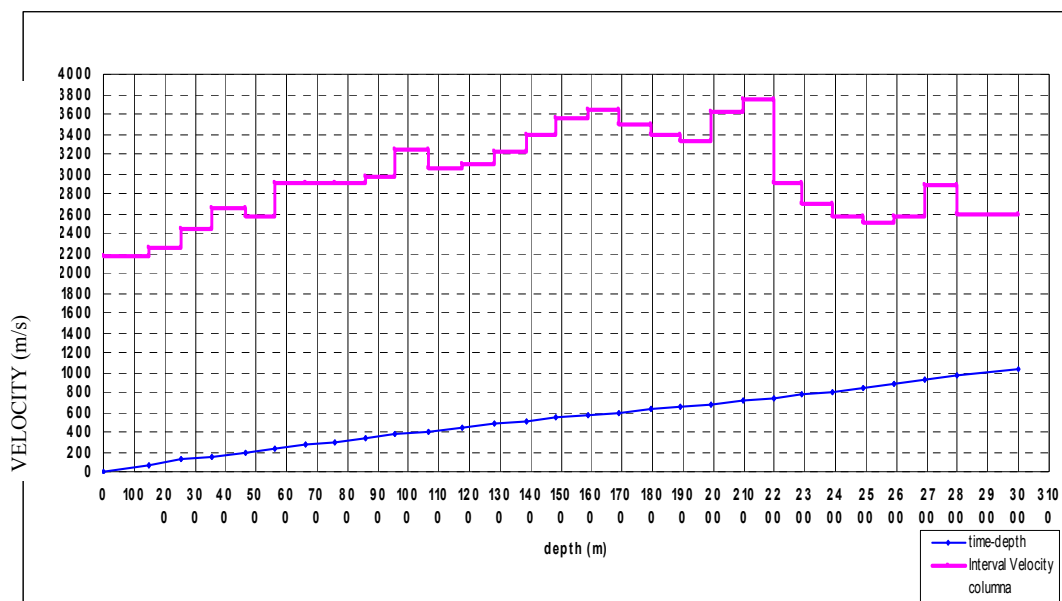


Figure B.12 Time-depth and interval velocities graph from the S-1 well.

S-2

Depth (m)	Two-way time (ms)	One-way time (ms)	Average Velocity m/s	Interval Velocity m/s
0	0	0.0	0	0
150	139	69.5	2158.27	2158.27
255	232	116.0	2198.28	2258.06
355	314	157.0	2261.15	2439.02
465	397	198.5	2342.57	2650.60
560	471	235.5	2377.92	2567.57
660	540	270.0	2444.44	2898.55
760	609	304.5	2495.89	2898.55
860	678	339.0	2536.87	2898.55
955	742	371.0	2574.12	2968.75
1065	810	405.0	2629.63	3235.29
1175	882	441.0	2664.40	3055.56
1280	950	475.0	2694.74	3088.24
1385	1015	507.5	2729.06	3230.77
1485	1074	537.0	2765.36	3389.83
1590	1133	566.5	2806.71	3559.32
1690	1188	594.0	2845.12	3636.36
1795	1248	624.0	2876.60	3500.00
1890	1304	652.0	2898.77	3392.86
1990	1364	682.0	2917.89	3333.33
2095	1422	711.0	2946.55	3620.69
2200	1478	739.0	2977.00	3750.00
2290	1540	770.0	2974.03	2903.23
2390	1614	807.0	2961.59	2702.70
2490	1692	846.0	2943.26	2564.10
2590	1772	886.0	2923.25	2500.00
2690	1850	925.0	2908.11	2564.10
2800	1926	963.0	2907.58	2894.74
3000	2080	1040.0	2884.62	2597.40

Table B.13 Velocity data from the S-2 well

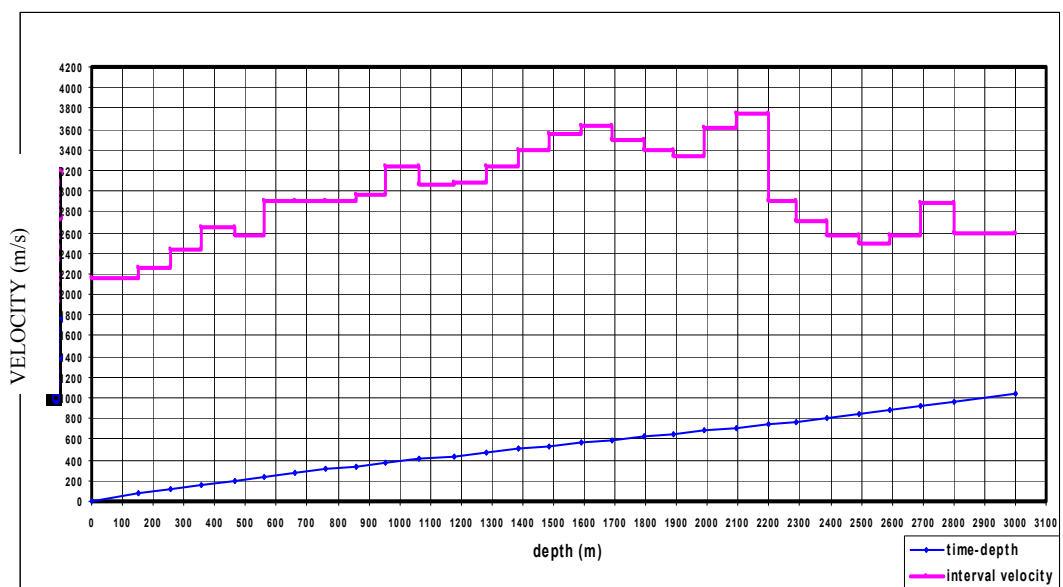


Figure B.13 Time-depth and interval velocities from the S-2 well.

Appendix C

Cored Intervals

Well name	CORE_1 (meters)	CORE_2 (meters)	CORE_3 (meters)
BAZ-1	1614-1622	1810-1817	1832-1840
IND-1	1819-1827		
MAC-1	2254-2262	2700-2708	
M-29D	1695-1703		
M-46	1770-1778		
M-47	1650-1658		
M-62	1581-1589		
M-1001	1881-1889	2059-2067	
S-1	2791-2799	2825-2833	

Table C.1 Core intervals in wells from the study area

Appendix D

Production Database

Well Name	Result	Shows (meters)	Intervals (meters)	Gas (mmcf/d)	Condensate (bpd)	Water (bpd)
A-1	Producer	1870, 2154, 2198, 2231	2280-2285 2254-2258 2149-2153	1.6 4.2 3.2	1.4 41 12	0
BAZ-1	Producer		1927-1938 1826-1839 1647-1655	0.258 2.939 0.8	216 68 48	0
EC-1	Producer	2085, 2235	2373-2406 2333-2349 2223-2248	2.336 1.723 1.026	36 38 --	0
EM-1	Non Commercial		1579-1603 1499-1548	0.13 0.361	50 5	--
GAL-1	Producer	1801, 1831	1952-1956	3.1	149	0
GALI-1	Producer	2047, 2248	2302-2305	3.7	108	24
K-1	Producer	512, 2775, 2986, 3214, 3455, 3555	1303-1307* 3553-3564 3464-3479 } 3450-3462 }	4.41 3.2 7.407	0 2 2	
MAC-1	Non Commercial	2253, 2565, 2698	2920-2928 2246-2255	0.3 0.8	7 32	220 48
M-1001	Producer	-----	2020-2032 2063-2072	6 28	0 0	0 0
IND-1	Non Commercial	-----	----- ---	-----	-----	----- -----
S-1	Producer	-----	2823-2825 2865-2872	6.2 3.4	1.5 2.0	0 0

Table D.1 Production data from the last drilled wells in the Vicksburg trend in the Burgos Basin (Data from PEMEX, E & P, Reynosa, Tamps)

Field	Gas Reserves		WELL			Production (Bcfd)
	Original	Produced	Total	Producer		
				Original	Present	
Cuitláhuac	1077	124	104	87	68	
Lomitas	49.6	46.9	40	15	4	0.15
Misión	47.1	28.8	40	22	3	3.00
Tinta	23.4	15.2	7	5	2	0.05
Polvareda	25.1	19.5	6	2	2	2.70
Pascualito	91.8	59.3	23	15	10	1.80
Pípila	46.3	13.0	7	6	6	1.20
Torrecillas	23.6	9.1	17	10	4	0.50
Gomeño	0.8	0.5	1	1	0	0.00
Truje	5.8	0.3	2	2	0	0.00
Indígena	3.6	0.62	4	3	1	0.01
Blanquita	0.2	0.17	4	1	0	0.00
Río Bravo	2.6	0.14	4	2	0	0.00
Total	1396.9	317.53	259	171	100	66.31

Table D.2 Production data for Vicksburg fields in the Burgos Basin (data from PEMEX, E & P, Reynosa, Tamps.)

Bibliography

- Alam, A. S., Matsumoto, C. H., and Caragounis, P., 1995, Quantitative porosity prediction from seismic attributes, Society of Exploration Geophysicists, Sixty-fifth Annual International Meeting, p. 313-315
- Asquith, G., 1982, Basic well log analysis for geologists: American Association of Petroleum Geologists, Tulsa, OK., 216 p.
- Bally, A. W., 1989, Phanerozoic Basins of North America; *in* The Geology of North America, Vol. A, The Geology of North America-An Overview, Bally, A. W., ed., The Geological Society of America, p. 397-446.
- Barrios-Rivera, J., Torres-Verdín, C., Salazar-Soto, H., Herrera-Mercado, V., and Mendez-Pineda, M., 2002, Lamé parameters and acoustic and shear volumes from simultaneous inversion. X Simposio de Geofísica y Exposición, Veracruz, Ver., México, Abstracts.
- Berg, R. R., and Habeck, M. F., 1982, Abnormal pressures in the Lower Vicksburg, McAllen Ranch field, South Texas: Gulf Coast Association of Geological Societies Transactions, v. 32, p. 247-253.
- Biot, M. A., 1956a, Theory of propagation of elastic waves in a fluid-saturated porous solid. I. Low frequency range: J. Acoust. Soc. Am., 28, 168-178.
- Biot, M. A., 1956b, Theory of propagation of elastic waves in a fluid-saturated porous solid. II. Higher frequency range: J. Acoust. Soc. Am., 28, 179-191.
- Brown, A. R., 1999, Interpretation of 3-Dimensional Seismic Data, 5th ed: AAPG Memoir # 42, Tulsa, OK., 514 p.
- Bruce, C. H., 1972, Pressured shale and related sediment deformation: a mechanism for development of regional contemporaneous faults: Gulf Coast Association of Geological Societies Transactions, v. 22, p. 23-31.
- Bruce, C. H., 1983, Shale tectonics, Texas coastal area of growth faults, *in* A. W. Bally, ed., Seismic expression of structural styles, Vol. 2: American Association of Petroleum Geologists Studies in Geology Series, No. 15, p. 2.3.1.1-7.

- Busch, D. A., 1973, Oligocene studies, Northeast Mexico: Gulf Coast Association of Geological Societies Transactions, v. 23, p. 136-145.
- Busch, D. A., 1975, Influence of growth faulting on sedimentation and prospect evaluation: American Association of Petroleum Geologists Bulletin, v. 59, p. 217-230.
- Castagna, J. P., and Backus, M. M., Eds., 1993, Offset-dependent reflectivity Theory and practice of AVO analysis: Society of Exploration Geophysicists, 348 p.
- Cavazos-Prado, S., 1969, Los horizontes bioestratigráficos de correlación en el estudio estratigráfico y sedimentológico del Oligoceno en la Cuenca de Burgos, *in* Seminario sobre Exploración Petrolera, Mesa Redonda No.1, Problemas de Exploración de la Cuenca de Burgos: Instituto Mexicano del Petróleo, p. 68-73.
- Cloos, E., 1968, Experimental analysis of Gulf Coast fracture patterns: American Association of Petroleum Geologists Bulletin, v. 52, p. 420-444.
- Coleman, J. M., and Galloway, W. E., 1990, Sequence stratigraphic analysis of the lower Oligocene Vicksburg Formation of Texas, *in* Society of Economic Paleontologists and Mineralogists Foundation, Gulf Coast Section, Eleventh Annual Research Conference Programs and Abstracts, p. 99-112.
- Combes, J. M., 1990, Depositional systems and tectonic-eustacy history of the Oligocene Vicksburg episode of the northern Gulf Coast: The University of Texas at Austin, Ph.D. dissertation, 537 p.
- Connolly, P., 1999, Elastic impedance: The Leading Edge, V. 18, p. 438-452.
- Corpus Christi Geological Society, 1968, Natural gas in post-Eocene formations in South Texas, *in* Beebe, B. W., ed., Natural gases of North America: American Association of Petroleum Geologists Memoir 9, v. 1, p. 233-263.
- Currie, J. B., 1956, Role of concurrent deposition and deformation of sediments in development of salt-dome graben structures: American Association of Petroleum Geologists Bulletin, v. 40, p. 1-16.
- Del Valle García, R. Ramírez, and Cuauhtémoc, L., 1990, Nuevas perspectivas de interpretación sismoestratigráfica, por medio de atributos sísmicos no

convencionales: Revista del Instituto Mexicano del Petróleo, número 22, p. 6-13

- Dickerman, K., Caamano, E., and Roopa, G., 1994, Spatial distribution of reservoir properties using seismic attributes correlated to log properties, American Association of Petroleum Geologists, International Conference and Exhibition; Abstracts, *in* AAPG Bulletin, 78, p. 1140.
- Diegel, F. A., et al., 1995, Cenozoic structural evolution and tectono-stratigraphic framework of the northern Gulf coast continental margin, *in* M.P.A. Jackson, D.G. Roberts, and S. Snelson, eds., Salt tectonics: a global perspective: AAPG Memoir 65, p. 109-151.
- Dufour, J., et al., 1998, AVO analysis to extract rock parameters on the Blackfoot 3C-3D seismic data: SEG Expanded Abstracts.
- Echánove-Echánove, O., 1976, Geología del Paleoceno-Eoceno, Cuenca de Burgos, *in* III Simposio de Geología del Subsuelo, Distrito Frontera Noreste, Reynosa, Tamaulipas: PEMEX internal report.
- Echánove-Echánove, O., 1986, Geología petrolera de la Cuenca de Burgos: Boletín de la Asociación Mexicana de Geólogos Petroleros, v. 28, p. 3-69.
- Edwards, M. B., 1980, The Live Oak delta complex: an unstable, shelf-edge delta in the deep Wilcox trend of South Texas: Gulf Coast Association of Geological Societies Transactions, v. 30, p. 71-79.
- Eguiluz, S., Bernabé, G., Mendoza, M., and Meckel, L., 2001, Estudio del Play Vicksburg Sur en la Cuenca de Burgos, México, Pemex, Exploración y Producción, Activo de Exploración Reynosa, Grupo de Plays-Larry Meckel, unpublished.
- Fisher, W. L., 1969, Facies characterization of Gulf Coast Basin delta systems, with some Holocene analogues: Gulf Coast Association of Geological Societies Transactions, v. 19, p. 239-261.
- Fisher, W. L., Brown, L. F., Jr. Scott, A. J., and McGowen, J. H., 1969, Delta systems in the exploration for oil and gas: The University of Texas at Austin, Bureau of Economic Geology, 212 p.
- Galloway, W. E., and Hobday, D. K., 1983, Terrigenous clastic depositional systems, applications to petroleum, coal, and uranium exploration: New York, Springer-Verlag, 489 p.

- Galloway, W. E., 1986a, Depositional and structural framework of the distal Frio Formation, Texas coastal zone and shelf. The University of Texas at Austin, Bureau of Economic Geology Geological Circular 86-8, 16 p.
- Galloway, W. E., 1986b, Growth faults and fault-related structures of prograding terrigenous clastic continental margins: Gulf Coast Association of Geological Societies Transactions, v. 36, p. 121-128.
- Galloway, W. E., 1989a, Genetic stratigraphic sequences in basin analysis I; Architecture and genesis of flooding-surface bounded depositional units: American Association of Petroleum Geologists Bulletin, v. 73, p. 125-142.
- Galloway, W. E., 1989b, Genetic stratigraphic sequences in basin analysis II; Application to northwest Gulf of Mexico Cenozoic basin: American Association of Petroleum Geologists Bulletin, v. 73, p. 143-154.
- García del Angel, A., 1969, Problemas de la futura exploración con pozos profundos en la Cuenca de Burgos, *in* Seminario sobre Exploración Petrolera, Mesa Redonda No. 1, Problemas de Exploración de la Cuenca de Burgos: Instituto Mexicano del Petróleo, p. 68-124.
- Gassmann, F., 1951a, Elastic waves through a packing of spheres: Geophysics, 16, p. 673-685.
- Gassmann, F., 1951b. Über die Elastizität poröser Medien: Vierteljahrsschr. derschweiz Naturforsch. Gesellschaft Zurich, v. 96, p. 1-121.
- Gastaldi, C., Biguenet, J. P., and de Pazzis, L., 1997, Reservoir characterization from seismic attribute; an example from the Peciko Field (Indonesia), The Leading Edge, 16, p. 263-266.
- Geerstma, J., 1961, Velocity-log interpretation: The effect of rock bulk compressibility: Society of Petroleum Engineers. J., I, p. 235-248.
- González-García, R., 1976, Bosquejo geológico de la Zona Noreste: III Simposio de Geología del Subsuelo, DFNE, Reynosa, Tams., Petróleos Mexicanos, p. 120.
- Goodway, B., et al., 1997, Improved AVO fluid detection and lithology discrimination using Lamé petrophysical parameters: 'λρ', 'μρ', and 'λμ fluid stack' from P and S inversions: CSEG Abstracts, p. 453.

- Hamblin, W. K., 1965, Origin of "reverse drag" on the downthrown side of normal faults: American Association of Petroleum Geologists Bulletin, v. 76, p. 1145-1164.
- Han, J. H., 1981, Genetic stratigraphy and associated growth fault structures of the Vicksburg Formation, South Texas: The University of Texas at Austin, Ph.D. dissertation 178 p.
- Han, J. H., and Scott, A. J., 1981, Relationships of syndepositional structures and delatation, Vicksburg (Oligocene), South Texas: Society of Economic Paleontologists and Mineralogists, Gulf Coast Section, Second Annual Research Conference, Program and Abstracts, p. 33-40.
- Hansen, T., 1996, Reservoir characterization by cokriging petrophysical well data and seismic attributes, Transactions of SPWLA Annual Logging Symposium, 37 p.
- Hansen, T., 1993, Mapping of petrophysical properties based on statistical correlations with seismic attributes: The Log Analyst, v. 34, p. 90.
- Hardage, B. A., Pendelton, V. M., Simmons, J. L., and Edson, R., 1995, A 3-D seismic case history evaluating fluviially deposited thin-bed reservoirs in a gas-producing property: The University of Texas at Austin, Bureau of Economic Geology, Geological Circular 95-I.
- Hardin, G. C., 1967, Notes on Cenozoic sedimentation in the Gulf Coast Geosyncline, *in* Geology of the Gulf Coast and Central Texas: Houston Geological Society, p. 1-15.
- Hastings, J. O., Jr., 1984, Structure, depositional environment, and pressure characteristics of the Vicksburg Formation, South Texas: Javelina and East McCook fields, Hidalgo County, Texas: Texas A&M University, Master's thesis, 162 p.
- Hegelsen, J., Magnus, I., Prosser, S., Saigal, G., Aamodt, G., Dolberg, D., and Busman, S., 2000, Comparison of constrained sparse spike and stochastic inversion for porosity prediction at Kristin Field: The Leading Edge, v. 19 (4), p. 400-408.
- Hernández-Mendoza, J. J., 2000, Interpretation and distribution of depositional systems: Oligocene Frio depisode in the subsurface of Burgos Basin, Northeastern Mexico: The University of Texas at Austin, M.S. Thesis, 256 p.

- Hill, D. P., Lennon, R. B., and Wright, C. L., 1991, Making an old gem sparkle, the rejuvenation of McAllen Ranch field, Texas: Gulf Coast Association of Geological Societies Transactions, v. 41, p. 325-335.
- Kosters, E. C., Bebout, D. G., Seni, S. J., Garrett, C. M., Jr., Brown, L. F., Jr., Hamlin, H. S., Dutton, S. P., Ruppel, S. C., Finley, R. J., and Tyler, Noel, 1989, Atlas of major Texas gas reservoirs: The University of Texas at Austin, Bureau of Economic Geology Special Publication, 161 p.
- Langford, R. P., Wermund, E. G., Grigsby, J. D., Guevara, E. H., Zinke, S. K., Collins, R. E., Sippel, M., Hower, T., Lord, M., Kocberber, S., and Howard, W. E., 1992, Secondary natural gas recovery: reservoir heterogeneity and potential for reserve growth through infield drilling: an example from McAllen Ranch field, Hidalgo County, Texas: The University of Texas at Austin, Bureau of Economic Geology, topical report prepared for the Gas Research Institute and U.S. Department of Energy, under contract nos. 5088-212-1718 and DE-FG21-88MC25031, GRI-92/0122, 289 p.
- Langford, R. P., and Combes, J. M., 1994, Depositional environments of unstable margin-shelf deltas of the Oligocene Vicksburg Formation, McAllen Ranch field, South Texas: The University of Texas at Austin, Bureau of Economic Geology Report of Investigations No. 219, 60 p.
- Latimer, R. B., and van Riel, P., 1996, Integrated seismic reservoir characterization and modeling: a Gulf of Mexico 3-D case study. <http://www.jasongeo.com/frame.html>.
- Lefeuvre, F., and Chanet, A., 1993, Reservoir characterization; a seismic attributes approach: Society of Exploration Geophysicists, Annual Meeting, 63, p. 289-292.
- Loucks, R. G., 1978, Sandstone distribution and potential for geopressed geothermal energy production in the Vicksburg Formation along the Texas Gulf Coast: Gulf Coast Association of Geological Societies Transactions, v. 28, p. 239-271.
- Magnier, B., 1994, Reservoir characterization by using 3-D seismic attributes with log properties: American Association of Petroleum Geologists Bulletin, v. 78, p. 1153.

- Matteucci, G., 1996, Seismic attribute analysis and calibration; a general procedure and a case study, Society of Exploration Geophysicists, Annual Meeting, 66, p. 373-376.
- Mayall, M. J., Teilding, C. A., Oldroyd, J. D., Pulham, A. J., and Sakurai, S., 1992, Facies in a shelf-edge delta—an example from the subsurface Gulf of Mexico, Middle Pliocene, Mississippi Canyon, Block 109: American Association of Petroleum Geologists Bulletin, v. 76, p. 435-448.
- Ostrander, W. J., 1984, Plane-wave reflection coefficients for gas sands at nonnormal angles of incidence: Geophysics, v. 49, p. 1637-1648.
- Peel, F. J., C. J. Travis, and J. R. Hossack, 1995a, Genetic structural provinces and salt tectonics of the Cenozoic offshore U. S. Gulf of Mexico: a preliminary analysis: *in* M. P. A. Jackson, D. G. Roberts, and S. Snelson, eds., Salt tectonics: a global perspective: AAPG Memoir 65, p. 153-175.
- PEMEX, 1993, Estudio regional integrado de los sistemas sedimentarios del sur de Texas y norte de México: PEMEX-Chevron, unpublished.
- PEMEX, 1994, Estudio del Potencial Remanente en la Cuenca de Burgos, Reynosa, Tamaulipas: PEMEX, Exploración y Producción, Region Norte, unpublished.
- PEMEX, 1999, Modelo depositacional y distribución de arenas del Oligoceno Frío (Frío No Marino Basal) en el área Misión-Lomitas-Tinta, Cuenca de Burgos, México), Pemex Exploración y Producción, Activo de Exploración Reynosa, Grupo Camargo-Larry Meckel, unpublished.
- PEMEX, 2002, Estudio de plays Vicksburg-Frío de la Cuenca de Burgos, México. Preparado para PEMEX, Exploración y Producción, por The Scotia Group, unpublished.
- Pendrel, J., and Van Riel, P., 1997. Methodology for seismic inversion and modeling: a Western Canadian Reef example: CSEG Recorder, V. XXII, p. 5.
- Pérez-Cruz, G. A., 1992, Geologic Evolution of the Burgos Basin, Northeastern Mexico: Ph.D. dissertation, Rice University, Houston, Texas, 155 p.
- Pickett, G. R., 1993, Acoustic Character Logs and Their Applications in Formation Evaluation, Journal of Petroleum Technology, v. 15, pp. 650-677.

- Picou, E. B., Jr., 1981, McAllen Ranch field: depositional environments of reservoir sandstones and associated shales- the Shell Oil viewpoint: Society of Economic Paleontologists and Mineralogists, Gulf Coast Section, p. 113.
- Rainwater, E. H., 1964, Transgressions and regressions in the Gulf Coast Tertiary: Gulf Coast Association of Geological Societies Transactions, v. 14, p. 217-230.
- Rodríguez-Santana, B., 1969, Sedimentos del Oligoceno de la Cuenca de Burgos- Aspecto regional, *in* Seminario sobre Exploración Petrolera, Mesa Redonda No. 1, Problemas de Exploración de la Cuenca de Burgos: Instituto Mexicano del Petróleo, p. 45.
- Rutherford, S. R., and Williams, R. H., 1989. Amplitude-versus-offset variations in gas sands: Geophysics, v. 54, p. 680-688.
- Sandoval-Cambranis, M. J., 1969, Interpretación sedimentaria del Oligoceno Inferior en la Cuenca de Burgos, *in* Seminario sobre Exploración Petrolera, Mesa Redonda No.1, Problemas de Exploración de la Cuenca de Burgos: Instituto Mexicano del Petróleo, p. 68-70.
- Sheriff, R. E., 1985, Aspects of seismic resolution, in Berg, O. R., and Woolverton, D. G., eds., Seismic Stratigraphy II: An Integrated Approach, AAPG Memoir 39, p. 1-10.
- Sonneland, L., and Barkved, O., 1990, Use of seismic attributes in reservoir characterization, in Buller, A. T., Berg, E., Hjelmeland, O., Kleppe, J., Torsaeter, O., and Aasen, J. O., (eds.), Proceedings of the North Sea oil and gas reservoirs conference, p. 125-128.
- Straccia, J. R., 1981, Stratigraphy and structure of the Rosita gas fields, Duval County, Texas: Gulf Coast Association of Geological Societies Transactions, v. 31, p. 191-200.
- Sutter, J. R., and Berryhill, H. L., 1985, Late Quaternary shelf-margin deltas, northwest Gulf of Mexico: American Association of Petroleum Geologists Bulletin, v. 69, p. 77-91.
- Tatham, R. H., and Stoffa, P. L., 1976, Vp/Vs-- a potential hydrocarbon indicator: Geophysics, v. 41, p. 837-849.

- Torres-Verdín, C., et al., 1999. Trace-based and geostatistical inversion of 3D seismic data for thin-sand delineation: An application in San Jorge Basin, Argentina: *The Leading Edge*, V. 18, No. 9, p. 1070-1077.
- Whitbread, T., Nicholson, T., and Owens, B., 2001, Structural evolution of a detached delta system--the Vicksburg of South Texas: *The Leading Edge*, October, p. 1106-1117.
- Winker, C. D., 1982, Cenozoic shelf margins, Northwestern Gulf of Mexico: *Gulf Coast Association of Geological Societies Transactions*, v. 22, p. 427-448.
- Winker, C. D., and Edwards, M. B., 1983, Unstable progradational clastic shelf margins: *Society of Economic Paleontologists and Mineralogists Special Publication No. 33*, p. 139-157.
- Yzaguirre, L. A., 1969, Geología regional de la Cuenca de Burgos, *in* Seminario sobre Exploración Petrolera, Mesa Redonda No. 1, Problemas de Exploración de la Cuenca de Burgos: Instituto Mexicano del Petróleo, p. 22.

Vita

Jorge Barrios Rivera was born in Tampico, Tamps., México, the fifth child of Felipa Rivera Maury and Eleuterio Barrios Del Angel. He has eight brothers and sisters. He attended and graduated from Instituto Tecnológico de Cd. Madero in 1983 with a B.S. in Geophysics. The same year, he worked for Compañía Mexicana de Exploraciones, S.A., in a 2D seismic party. In 1984, he was employed by Petróleos Mexicanos (PEMEX). After working for four years in gravimetric, magnetotelluric, and seismic parties in domestic assignments in the states of Veracruz, Guerrero, and Oaxaca, in 1988 he entered the graduate school at the Universidad Nacional Autónoma de México, where he graduated with an M.S. in Hydrocarbon Exploration. For eight years he worked in prospect evaluation in Macuspana and Comalcalco Basins as well as in the Chiapas Fold Belt of Southern México. He entered in 1998 to graduate school at The University of Texas at Austin to pursue a Ph.D. in Geological Sciences.

He married Norma Edith Rojas in 1991. He is the father of two children Jocelyn Edith and Jorge Luis.

Permanent address: Manuel Antonio Romero # 44
Colonia Pensiones, C.P. 86170
Villahermosa, Tab., Mexico
Email: jorge.barrios@lycos.com
jbarriosr@pep.pemex.com

This dissertation was typed by the author.